Travail de fin d'études et stage[BR]- Travail de Fin d'Etudes : Turbulent heat transfer analysis of supercritical carbon dioxide close to the pseudo-critical point in microchannels under non-uniform heat flux boundary conditions[BR]- Stage d'insertion professionnelle

Auteur : Schyns, Bertrand
Promoteur(s) : Lemort, Vincent
Faculté : Faculté des Sciences appliquées
Diplôme : Master en ingénieur civil électromécanicien, à finalité spécialisée en énergétique
Année académique : 2019-2020
URI/URL : http://hdl.handle.net/2268.2/10386

University of Liege
Faculty of Applied Sciences
Aerospace and Mechanical Engineering Department
Thermodynamics Laboratory

Turbulent heat transfer analysis of supercritical carbon dioxide close to the pseudo-critical point in microchannels under non-uniform heat flux boundary conditions

Schyns Bertrand

Academic year: 2019-2020

Master's Thesis Submitted in Partial Fulfillment of the
Requirement for the Master Degree of
Electro-Mechanical Engineering

President of the jury: Dewallef P.

Composition of the jury:
Lemort V., University of Liege (Main Adviser)
Fronk B., Oregon State University
Ngendakumana P., University of Liege
Dumont O., University of Liege

Turbulent heat transfer analysis of supercritical carbon dioxide close to the pseudo-critical point in microchannels under non-uniform heat flux boundary conditions

by Schyns Bertrand
Main Adviser: Lemort V.

Master's Thesis submitted on the 21th of August 2020 to the Faculty of Applied Sciences of the University of Liège in partial fulfilment of the requirements for the degree of Electro-mechanical Engineering

With the increasing heat flux produced by more and more compact electronics device, new technologies are studied to replace more conventional air cooling systems. Due to the good thermal properties of the carbon dioxide around its pseudo-critical point, its safety and its low cost, microchannel based heat exchanger using supercritical carbon dioxide might be a suitable alternative to reduce the power used at the pump and manage the high heat load of the new electronic devices.

This work investigates the performance of a microchannel based heat exchanger using supercritical carbon dioxide close to its pseudo-critical point as its working fluid and subject to a non-uniform heat flux boundary condition. To achieve this particular boundary condition, the heat exchanger is heated up by Joule effect through its bottom Inconel plate. The other sides of the exchanger, being made of Torlon plastic, insure a thermal insulation on three of the four sides of the channels. Two different aspects are studied. On the one hand, the turbulent heat transfer is analysed experimentally. At first in steady-state conditions, the impact of different parameters (inlet temperature, heat flux and mass flux) over the heat transfer is analysed. Then the response of the system to transient heat flux and mass flux is also experimentally tested. On the other hand, a modeling work is investigated in parallel. A model is develop at first for the steady-state heat exchange and the experimental results are used to validate the model predictions. Finally, a transient model is then developed to predict the transient heat exchange with a varying heat flux and mass flux.

First of all, experimental data were recorded with only one varying parameter (the other being as constant as possible) to determine the impact of the different parameters without the interaction of the others. In addition to the traditional heat transfer coefficient and temperature measures the results include the analysis of the buoyancy and the acceleration effect with the help of different developed criteria. It was rapidly shown that the acceleration effect was negligible in all experimental conditions used throughout this work. On the contrary buoyancy effect is present in most tests due to the high density gradient across the boundary layer. Overall, the results showed a negative effect over the heat transfer caused by a higher heat flux with a lower heat transfer coefficient, higher temperatures and higher buoyancy effects. On the opposite, the mass flux was shown to improve the results with much higher heat transfer coefficients, lower temperatures and lower buoyancy effects. The inlet temperature showed to be the parameter with the smallest impact over the performances. The general transient response of the system was shown to be fast with the possible apparition of some local effects during a heat flux variation. However the lack a data points makes it impossible to confirm those without further testing.

Finally, a heat exchanger model is developed using the electrical analogy for both the steady-state and transient conditions. The results are in good agreement with the experimental work as more than 87% of the experimental tests are predicted with a mean absolute percentage error lower than 20%. The model predictions show a possible increase of the average heat transfer coefficient over the channel up to 15% with an optimized inlet temperature (considering that the pseudo-critical point is always reached in the exchanger). The mass flux is shown to have the highest impact over the heat transfer, a 0% increase of the mass flux leads to a 100% increase in the heat transfer coefficient and a quadratic decrease of the buoyancy effect. The model also shows number as high as $6000 \text{W/m}^2\text{K}$ over the whole channel in a realistic simulation of electronics cooling with a relatively low mass flux. Moreover, the transient model showed a really fast response of the system to both a varying heat flux and a varying mass flux.

In conclusion, the microchannel based heat exchanger using supercritical carbon dioxide shows promising results but needs some further research notably in the transient part.

Acknowledgements

Contents

List of Figures

List of Tables

Nomenclature

Acronyms

GWP Global Warming Potential

$MAPE$ Mean absolute percentage error

TDP Thermal design power

Symbols

β	Volumetric coefficient of expansion	[1/K]
$\dot{m}$	Mass flow	[kg/s]
ϵ	Turbulent dissipation rate	[m^2/^{3}]
μ	Dynamic viscosity	[Pa.s]
ν	Kinematic viscosity	[m^2/s]
ρ	Density	[kg/m^3]
ρ_e	Electrical resistivity	[Ohm.m]
σ	Turbulent Prandtl number	[-]
a	Acceleration	[m/s^2]
A_{cb}	Acceleration parameter	[-]
Bo	Buoyancy parameter	[-]
C	Heat capacity rate	[W/K]
c_p	Specific heat capacity	[J/(kg.K)]
D	Diameter	[m]
dx	Width of a finite element	[m]
dy	Length of a finite element	[m]
F_{VP1}	Non-uniformity function from [9]	[-]
G	Mass flux	[kg/m^{2}s]
g	Acceleration due to gravity	[m/s^2]
G_k	Turbulence generation term	
Gr	Grashof number	[-]
h	Heat transfer coefficient	[W/(m^2.K)]

h	Specific enthalpy	[J/kg]
I	Current	[Amp]
J	Current density	[Amp/m^2]
k	Thermal conductivity	[W/(m.K)]
K_v	Acceleration parameter	[-]
m	Mass	[kg]
Nu	Nusselt number	[-]
P	Pressure	[Pa]
Per	Perimeter	[m]
Pr	Prandtl number	[-]
q''	Heat flux	[W/m^2]
q_{gen}	Heat generated	[W]
R_a	Surface roughness	[m]
Re	Reynolds number	[-]
T	Temperature	[°C]
Th	Thickness	[m]
U	Velocity component along the x axis	[m/s]
V	Velocity component along the y axis	[m/s]
v	Specific volume	[m^3/kg]
W	Width	[m]

Subscripts

ϵ	parameter related ti turbulent dissipation rate
abs	Absolute
acc	Acceleration
b	Bulk
ch	Channel
$conv$	Convection
$corr$	Correlation
e	Electric
$elem$	Element
exp	Experimental
$film$	Film temperature
$fric$	Friction
h	Hydraulic

in	Inlet
int	Internal
PC	Pseudo-critical point
R	Reduced
rel	Relative
se	Side edge
sw	Side wall
t	Turbulent value
th	Threshold
w	Wall
k	Parameter related to turbulent kinetic energy

Chapter 1

Introduction

With the first computer ever created and the ascension of the electronics in our society, some technologies were developed to remove the heat produced. A good example to look at is the heat management of the data centers where different methods are used [10]. With the ever increasing compactness of electronics device, the heat flux to dissipate is growing leading to some challenges. Indeed, processors are more and more powerful while being smaller. According to Intel's data [11], the target power level to dissipate known as the thermal design power (TDP) can go up to 40-50 kW/m^2 for the current most powerful processors. In addition to this high heat flux, the electronics device are limited to low temperature (around 100°C) to avoid degradation.

With all those limitations, some current methods used could be unable to sustain the heat management in the future. Indeed, the use of air as primary fluid could become impossible due to the low heat capacity and the generally bad heat transfer properties. With that in mind several studies looked at the use of phase-change cooling. However with the need of low temperature, the only usable fluids are refrigerants with generally high GWP (Global Warming Potential). Another problem encountered with phase changing fluids is the apparition of instabilities and hot spots where potential bubbles would appear [12]. For that reason, the use of supercritical carbon dioxide as the working fluid was studied [13; 14].

The supercritical fluids are characterized by good heat transfer properties in the vicinity of the pseudo-critical point. Those properties come with a decrease in the fluid density but the clear distinction between the two phases no longer appears. This greatly reduces the instabilities present with fluids in their phase change.

The choice of the CO_2 comes from its critical point at only 31°C. This means that the pumping requirement will be low as long as the weather is not too hot. With its availability and its low price, CO_2 is a cheap and efficient while having a GWP of only 1, being non toxic and nonflammable. Compared to water, CO_2 presents the advantage to have better heat transfer properties close to its pseudo-critical point and to be non corrosive leading to lower maintenance cost. It also presents the advantage to be an electrical insulator, a leak on the electrical device would not cause a short circuit. The main problem of the supercritical carbon dioxide is the high pressure (over 7.3MPa) that creates a lot of constraints in the design of the heat exchanger and even microchannels heat exchanger needs to have some thick wall, increasing the thermal resistance in conduction.

In the last decades a lot of research was conducted in order to develop semi-empirical criteria to predict the effect of both buoyancy and acceleration over the heat transfer [2; 15]. However those research were conducted on macro-scale circular heat exchangers with an uniform heat flux. It is unsure if those predictions can be used in the case of a microchannels with a non uniform heat flux. This geometry with such boundary condition can be found in the case of solar receiver [16] or in this case the management of high heat flux in electronics [13]. This design using the microchannels has the advantage to present a high heat transfer coefficient due to the small hydraulic diameter. Moreover, the geometry allows a small quantity of fluid to cool down a large area. This responds to the need of electronics with high efficiency and compactness.

This study aims to understand the effects of those phenomena over the turbulent heat transfer with those boundary condition. Finally the goal is to see if such a design could be used in the case of the electronics cooling and its transient response to different perturbations.

1.1 State of the art of steady-state heat exchange associated with CO2 supercritical flow

In this section, the current knowledge of the steady-state heat exchange using supercritical carbon dioxide as exposed in the literature is presented.

1.1.1 Interest of supercritical fluids

Before looking at any technologies or research it is important to understand why a supercritical fluid is attractive in heat exchange and how the different properties of the fluid evolves around the pseudo-critical point.

The critical point for a pure substance is defined by the disappearance of the clear distinction between the liquid and gaseous phase. More specifically, it is the point where both the first and second partial derivatives of pressure with regards to the specific volume are equals to zero (Eq. 1.1 and 1.2).

$$\left(\frac{\partial P}{\partial v}\right)_T = 0 \tag{1.1}$$

$$\left(\frac{\partial^2 P}{\partial v^2}\right)_T = 0 \tag{1.2}$$

The supercritical region is bounded by pressure and temperature exceeding those of the critical point. Looking at Fig. 1.1, this boundary is at a temperature of 30.98°C and a pressure of 7.377MPa for the carbon dioxide. In that region, the isothermal lines do not cross the saturation curve. As the clear distinction between phases vanishes, the state can only be characterized as "liquid-like" or "gaseous-like" depending on the temperature for a given pressure. Indeed, the fluid presents a sharp variation in its thermophysical properties at the pseudo-critical point. The pseudo-critical point temperature is the one presenting the maximum specific heat capacity for a given reduced pressure ($P_R = \frac{P_{abs}}{P_{critical}}$). As can be deduced from Fig. 1.1, the higher the pressure, the higher the pseudo-critical temperature (e.g. T_{PC}=35.2°C for $P_R = 1.1$).
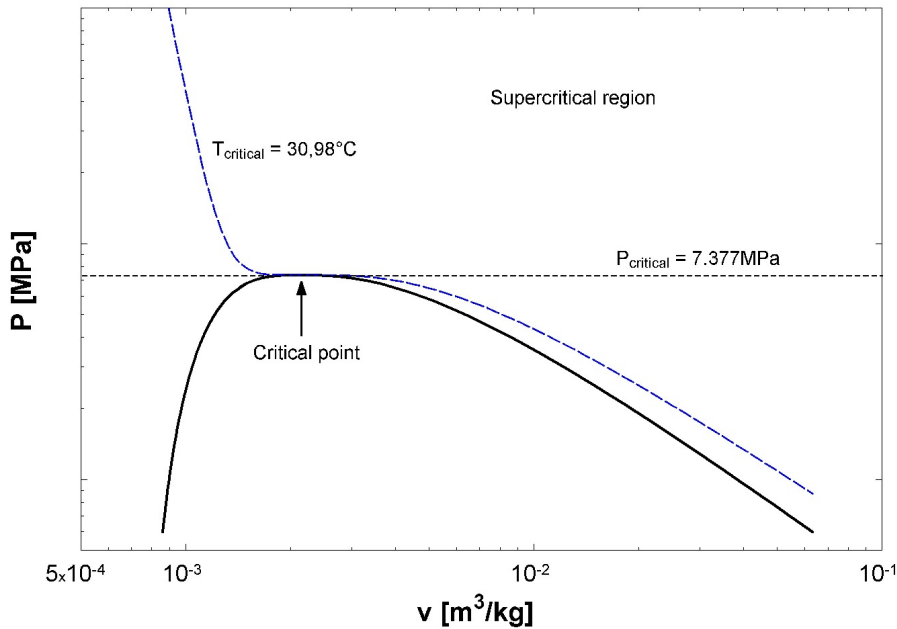
Figure 1.1: P-v diagram for carbon dioxide

An other property of the supercritcal fluids is the reduction of the specific heat capacity peak with an increasing reduced pressure as can be seen in Fig. 1.2a. This is explained by the proximity of the saturation curve and a

higher differentiation between the "liquid-like" and "gaseous-like" state when the pressure is lower. This is further shown in Fig. 1.2b where the partial derivative of the density with regard to the temperature tends more and more to a constant with a higher pressure showing a decreasing distinction between the two phases.

(a) Specific heat capacity

(b) Density

(c) Prandtl
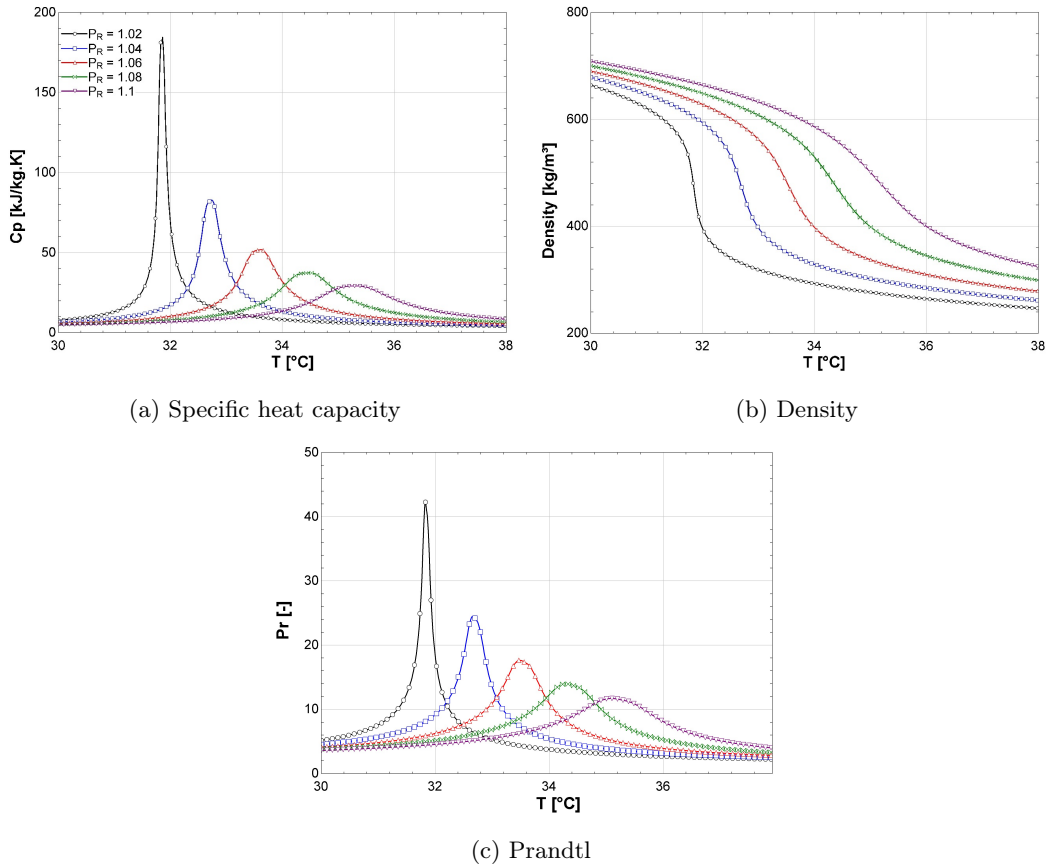
Figure 1.2: Thermophysical properties for the carbon dioxide for different reduced pressures with regard to the reduced temperature

The boundary layer of a fully developed flow can be divided into two layers, the turbulent layer and the diffusion sub-layer which is close to the wall. The thermal resistivity is mostly limited by the diffusion sub-layer where the heat transfer is dominated by conduction. In terms of non-dimensional parameters, the thickness of the sub-layer can be approximated by $\delta \approx Re^{-0.5} Pr^{-0.5}$. The Reynolds number depends on the flow condition, however the Prandtl number depends only of the fluid properties as $Pr = \frac{c_p \mu}{k}$ with μ the dynamic viscosity and k the thermal conductivity. With that, for a given Reynolds number, a higher Prandtl number should result in a smaller diffusion layer thickness thus a smaller resistance in conduction. As shown in Fig. 1.2c, the Prandtl number for the carbon dioxide shows a peak around the pseudo-critical temperature. As it is proportional to the specific heat capacity, the higher the reduced pressure, the lower the peak.

However the Prandtl number is not the only properties taking part in the thermal resistivity. The density gradient (transverse or axial) also plays a major role. Indeed the density gradient will alter the transient transport. In the case of this study with a heated bottom layer, a transverse density gradient will enhance the transient transport with the induced buoyancy. The diffusion layer will thus be smaller and the global resistivity will decrease. The axial density gradient will cause the fluid to accelerate through a favorable pressure gradient. In the case of really high heat flux, this thermally induced acceleration can in the extreme case cause a re-laminarization of the flow and so reduces the thermal transport [9].

1.1.2 Early interest in supercritical heat exchanger

The interest in supercritical fluid started in the 1950s when the United States and the Soviet Union looked for new potential fluids to use in the nuclear power plant and other steam generators [17]. The first studies in

forced convection described the heat transfer close to the pseudo-critical point to occur in the same way as boiling. Some deterioration in the heat transfer leading to peaks in the wall temperature were also observed [18]. Those contradictory reports on the heat transfer close to the pseudo-critical point led to more studies to understand the different occurring phenomena.

The desire at the time was to develop a correlation that could predict the heat exchange in the vicinity of the pseudo-critical point just like the Dittus-Boelter describes the heat transfer in sub-critical single-phase turbulent flow. The general trend in those research is that the maximum heat transfer occurs when the pseudo-critical temperature is reached in the boundary layer ($T_w > T_{PC} > T_b$). One of the first semi empirical prediction concerning the supercritical carbon dioxide was done by Bringer and Smith [19] and later improved by Hsu and Smith [20]. The later version took into account the variation in the density and with that the buoyancy effect in vertical tubes. The new model showed the possibility of a higher velocity in the boundary layer than in the center of the tube. The effect of the buoyancy over the velocity was later verified by experiments [21]. This discovery would lead to further research and will be described into more detail in the following section.

An other research to understand better the physical phenomena present in the boundary condition is a Thesis written by E. Hauptmann [22]. This study used the Schlieren image method which uses the variation in the refractive index of fluids with their density to capture the variation in density over a heated plate. The study looked at different cases to compare the image with the results of the heat transfer coefficient measures.

A part of the study aimed to determine if buoyancy was present in supercritical heat transfer. Fig. 1.3 shows four images of a turbulent boundary layer developing from left to right over a heated plate in different experimental conditions. The speed is fixed for all tests at 1.5ft/s (0.45m/s) with a corresponding Reynolds number of around 10^6 in the test section leading to a fully developed turbulent layer. In those image, the black lower part corresponds to the heated plate, the red/yellow layer is the boundary layer of hot fluid and the green layer at the top is the bulk fluid. Finally, black spots in the boundary layer correspond to high density gradient spots. Those images do not allow some detailed conclusion but rather give a global view of the boundary layer.
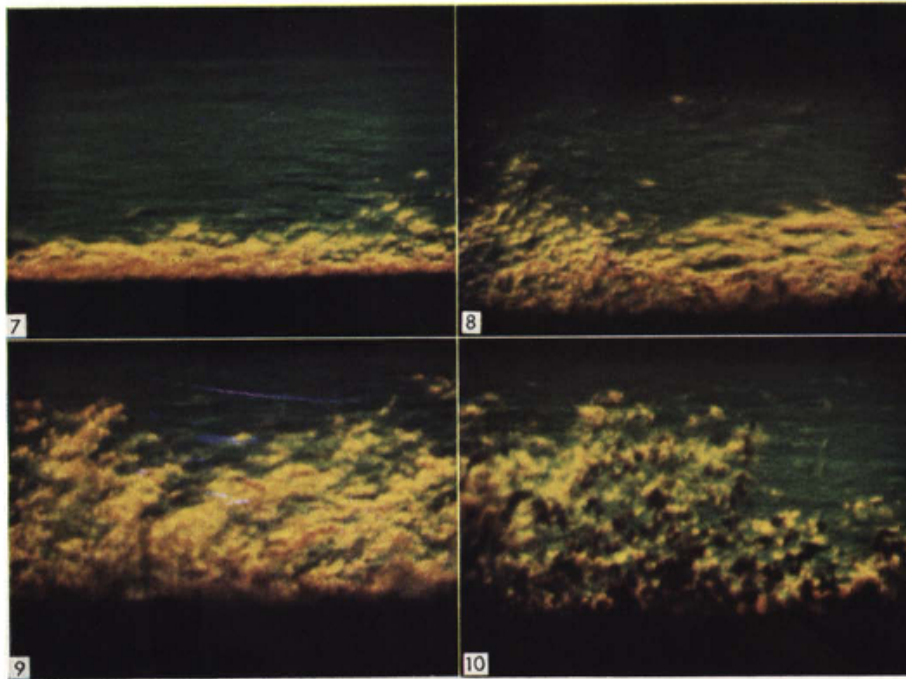
Figure 1.3: Schlieren images from the E. Hauptmann sCO_2 turbulent boundary layer study [1]. Images (7) to (9) are at a supercritical pressure (7.58MPa = 1100Psi) with a corresponding pseudo-critical temperature of 31°C and image (10) is at a sub-critical pressure (7.24MPa = 1050Psi). The bulk fluid temperature is fixed at 23.89°C (75°F) but the temperature difference between the wall and the bulk fluid change: (7) T_w-T_b = 4.94°C (8.9°F), (8) T_w-T_b = 9.88°C (17.8°F), (9) T_w-T_b = 33.66°C (60.6°F) and (10) T_w-T_b = 46.22°C (83.2°F).

The first test in Image (7) corresponds to a supercritical turbulent boundary layer with both the bulk fluid

temperature as well as the wall temperature bellow the pseudo-critical point. The density gradient is relatively small and no secondary motion perpendicular to the flow appears. In Images (8) and (9), the bulk fluid temperature stays at 23.89°C but the wall temperature is increased to the point that it becomes higher than the pseudo-critical temperature. With that, the pseudo-critical point is reached inside of the boundary condition leading to higher density gradient. According to [1], the density ratio between the free-stream and the fluid at the surface of the heated wall is around 2.5 in image (8) and grows to around 4.5 for Image (9) as the temperature difference increases. In both cases, a perpendicular motion appears and the width of the boundary layer increases as well. However in Image (8), besides the presence of some black spots at the wall, the boundary layer stays very much like a normal one-phase turbulent forced flow boundary layer. On the other hand, the higher wall temperature in Image (9) leads to a free convective motion and more black spots are presents.

To prove the presence and the importance of buoyancy, the study compared the results with an inverted orientation test section. The flow would be heated with the upper plate instead of the lower one. Two distinct cases were studied in [22], the first one was with a heat flux of 1.39 W/cm^2 (4400 BTU/hr.ft^2) and the second with 8.39 W/cm^2 (26600 BTU/hr.ft^2). In the first case and for wall temperature bellow the pseudo-critical point, the heat transfer coefficient does not change significantly with the orientation of the heated plate. However with the temperature approaching the pseudo-critical temperature the difference would increase. The maximum heat transfer coefficient reached for the upward-facing plate is 9085.2 W/m^2.K (1600 BTU/hr.ft^2.°F) compared to the 6813.9 W/m^2.K (1200 BTU/hr.ft^2.°F) for the downward-facing plate. This difference increases rapidly once the pseudo-critical temperature is exceeded. In the second case, due to the higher heat flux, the surface temperature is always higher than the pseudo-critical temperature (for the experimental conditions used). The heat transfer coefficient for the downward-facing heated plate is only around half that of the upward-facing plate. Those results prove the presence of buoyancy in supercritical heat transfer.

In order to compare the results, Image (10) shows a sub-critical flow being heated by a hot plate. The boundary layer is clearly impacted by buoyancy with some large vapor cluster breaking into the free stream. This clearly shows that even if buoyancy has an impact in super-critical heat transfer, those large clusters do not appear like in the sub-critical case. This explains the lower instabilities of super-critical fluids compared to phase changing fluids as stated previously in the introduction.

1.1.3   Influence of buoyancy and flow acceleration

Even if the supercritical fluid keeps a continuous evolution in its thermophysical properties, significant variations appear close to the pseudo-critical point. Those variations lead to the buoyancy discussed in the last section. To analyse the phenomenon into more detail, some experiments on vertical tubes were undertaken and are discussed in [2]. The use of vertical tube enables to compare the results between the upward and downward flows. Indeed, if the heat flux is high enough, some buoyancy induced forces will be applied to the flow. In the case of the upward flow, this added force is in the same direction than the flow and it is a buoyancy-aided flow. On the other hand, for a downward flow, the buoyancy force will be opposed to the forced flow and it is called a buoyancy-opposed flow.

An example of the evolution of the wall temperature of a vertical tube is exposed in Fig. 1.4, the downflow case shows a really continuous wall temperature that follows the temperature of the bulk fluid temperature. This results shows a high heat transfer coefficient in the whole tube. On the opposite, the upward flow wall temperature has a huge peak at some point in the tube. After the peak, the temperature decreases quite rapidly at first and then seems to converge towards the wall temperature of the downward flow. The first explanation provided to explain the shape of the temperature curve for the upward flow was to divide the flow in two parts with its own resistance. The first one, close to the wall would degrade with the increasing of the wall temperature well above the pseudo-critical point. This degradation would be then reduced by the bulk fluid temperature increasing towards the pseudo-critical temperature and reducing the resistance between the layer close to the wall and the one in the middle of the tube. However this theory was unable to explain the downward flow curve where the heat transfer coefficient would stay high with no peak in temperature.

An other theory proposed and developed in [2] is the influence of the buoyancy over the shear stress in the flow. In a flow with a uniform density, the shear stress decreases linearly from the edge of the wall to the center of the flow. Due to the heat flux applied, a density gradient will appear and this gradient can be significant around the pseudo-critical point. In Fig. 1.5, the flow is divided in two flow, a low density close to the wall and a high density in the center and the new resulting shear stress is represented with the inertia being neglected. This new
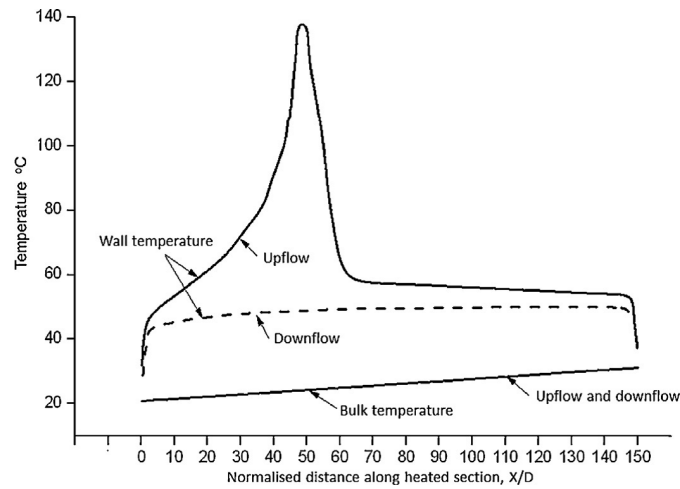
Figure 1.4: Evolution of the wall temperature for supercritical upflow and downflow in a heated vertical 5mm diameter tube from J.D. Jackson study [2].

distribution will create a higher shear stress close to the wall (as in reality it will be null at the wall) but a lower one closer to the middle of the tube as can be seen with boundary thickness of the test **(1)**. In the case of the upward flow, the buoyancy will lead to an increase of this phenomena. At some point, the case of the boundary layer thickness (corresponding to test **(2)**) is reached and the shear stress in the middle of the tube is reduced to zero with the associated reduction in the turbulent diffusivity. The lower diffusivity leads to a temperature peak at some point. After this peak, the shear stress at the end of the boundary layer becomes negative (in test **(3)**). This negative shear stress create instabilities inside the core fluid increasing the heat transfer coefficient and reducing the wall temperature. This new stage can be linked to a transition to a region dominated by free convection due to the huge impact of buoyancy. In the case of a downward flow, the buoyancy increases the shear stress at the end of the boundary layer improving the turbulent diffusivity and the heat transfer coefficient all along the tube keeping the wall temperature aligned with the bulk flow temperature.
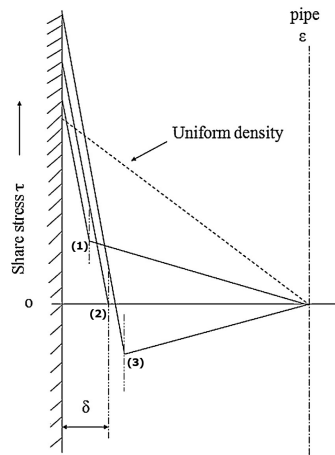
Figure 1.5: Shear stress distribution in a tube for different boundary layer thickness adapted from [2].

In order to find a better way to account for the buoyancy in heat transfer model, the new goal was to find a correlation fitting the experimental results. A new parameter combining the Grashof number, the Reynolds number and the Prandtl number appeared to characterize the phenomenon of buoyancy. In Fig. 1.6, the buoyancy parameter $Bo^\star$ is defined as $Gr_b^\star/(Re_b^m Pr_b^n)$ where $Gr^\star$ is the Grashof number usually defined as $Gr^\star = g\beta q'' D_h^4/k_b\nu_b$. In this graph, the different behavior are explicit. At the start, the buoyancy has a small effect and the Nusselt number is equal for upward and downward flow. Then the upflow starts to see a decrease when the buoyancy starts to impact the shear stress and the turbulent diffusivity. After a huge drop, the Nusselt number will start to increase back up and converge to the value of the downflow which increases at all time. With this new parameter some studies

started to develop new methods to account for the buoyancy in vertical tubes for supercritical heat exchange. A notable model was developed in Manchester by J.D. Jackson. The basic principle is to use an equivalent flow not impacted by the buoyancy with a new velocity higher or lower than the actual one to take its impact into account. The development of this model is described in [15] and [23].
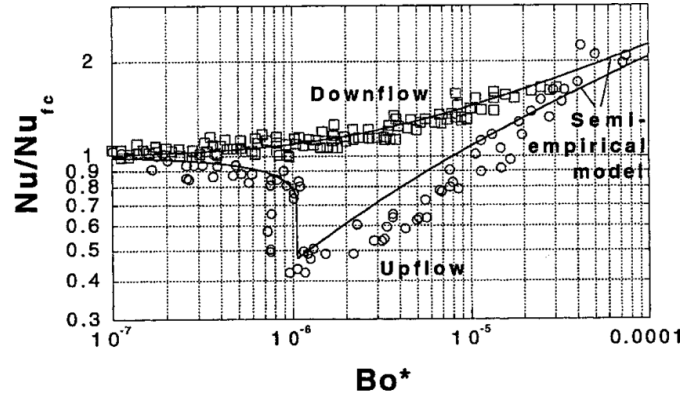
Figure 1.6: Effects of buoyancy on convective heat transfer for fully-developed flow in vertical circular tubes adapted from [3]

The effect of buoyancy being described in detail in vertical tubes, some research tried to compare the effect of the buoyancy in uniformly heated horizontal tubes. A general observation in those studies was the uneven temperature distribution around the tubes when the heat flux was high enough to create some buoyancy effects. This distribution is created by the concentration of low density and low velocity fluid at the top surface. On the other hand, the fluid at the bottom surface is accelerated due to the density gradient. Those two effects increase the turbulence intensity at the bottom while decreasing it at the top leading to the temperature difference. According to [24], the heat transfer coefficient of supercritical water at the bottom are up to 2.5 times larger than at the top surface in one of its experiment. The results also showed that the temperature difference between the two surfaces is maximum when the bulk fluid temperature is close to the pseudo-critical temperature. With the bulk fluid temperature increasing even more, the difference decreases and eventually gets to zero.

The study then looks at the existing correlation to determine the impact of buoyancy using different mass flow rate to have some data for heavily (low mass flow) to lightly (high mass flow) buoyancy influenced flow. Those results showed that the correlation previously presented in the case of vertical tubes did not get good results. Instead a correlation developed by Petukhov and Polyakov was used and verified. This correlation uses a threshold value for the Grashof number Gr_{th} defined in Eq. 1.3, under which the effect of buoyancy are negligible. The standard Grashof number is defined by Eq.1.5 and characterise the magnitude of the buoyancy in the flow.

$$Gr_{th} = 3 \times 10^{-5} Re_b^{2.75} \bar{Pr}^{0.5} [1 + 2.4 Re_b^{-1/8} (\bar{Pr}^{2/3} - 1)] \tag{1.3}$$

$$\bar{Pr} = \frac{h_w - h_b}{T_w - T_b} \frac{\mu_b}{k_b} \tag{1.4}$$

$$Gr_q = \frac{g \bar{\beta} q'' D_h^4}{\nu_b^2 k_b} \tag{1.5}$$

$$\bar{\beta} = \frac{1}{\rho_{film}} \frac{\rho_b - \rho_w}{T_w - T_b} \tag{1.6}$$

In a flow without any buoyancy effect, the ratio between Gr_q and Gr_{th} must be unity. Even in slightly impacted flow, the ratio will be higher than unity and this ratio will grow with the growing effect of buoyancy. According to [24], the experiment with the lowest mass flow rate had a ratio up to 200 where the one with the highest mass flow rate only had a ratio of maximum 5.

An other effect caused by heat flux in the fluid properties is the density gradient along the channel. This gradient caused by the change in temperature creates a positive pressure gradient leading to an acceleration of the bulk fluid as depicted in Fig. 1.7. According to different studies [25; 26; 27], this acceleration decreases the

turbulence intensity level reducing the thermal transport from the boundary layer to the bulk fluid. In extreme case, the boundary layer can reverse to a laminar boundary layer, further reducing the thermal transport.
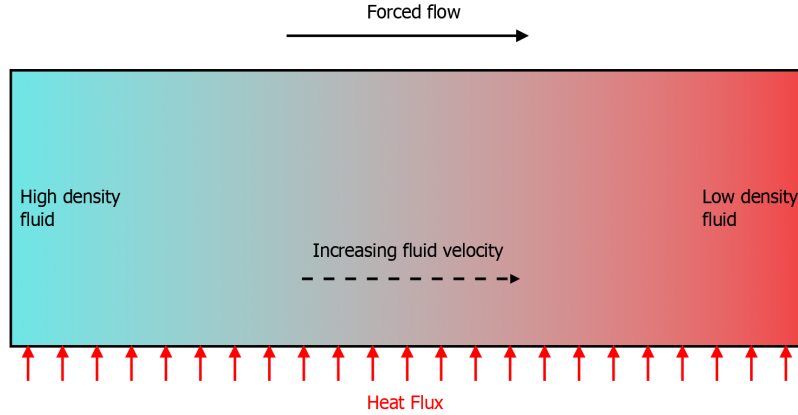
Figure 1.7: Acceleration of the flow caused by the heat flux

In order to take account of that phenomenon in uniformly heated tubes, some semi-empirical models were created by [9] and [3]. This model is developed in details in [9]. The idea is to compare the heat transfer between the normal case and the case where the acceleration is taken into account and is reducing the shear stress. From there correlations relating the friction and the heat transfer are used to find a relation between the shear stress and the heat transfer. Once it is done, a relation between the two Nusselt number can be defined in Eq.1.7. In this equation, Nu_b is the Nusselt number influenced by the acceleration and Nu_{b_0} is the one without its influence. If the acceleration parameter A_{cb} is small enough and that $C_A A_{cb} F_{VP1}$ is smaller than 0.385, the influence of the acceleration over the heat transfer will be less than 2%.

$$\frac{Nu_b}{Nu_{b_0}} = \left[\left| 1 - C_A A_{cb} F_{VP1} \left(\frac{Nu_b}{Nu_{b_0}} \right)^{-1.1} \right| \right] \tag{1.7}$$

$$C_A = 10^4 \tag{1.8}$$

$$A_{cb} = \frac{\beta_b q'' D}{k_b Re_b^{1.625} Pr_b} \tag{1.9}$$

$$F_{VP1} = \left(\frac{\mu_{ave}}{\mu_b} \right) \left(\frac{\rho_{ave}}{\rho_b} \right)^{-0.5} \tag{1.10}$$

This criterion was also adapted to asymmetric heating in horizontal duct by [3] in Eq. 1.11. The criterion says that when $K_v < 9.5 \times 10^{-7}$, the flow stays fully turbulent and the effect of the acceleration can be neglected. Above this threshold, the heat transfer will be affected. Finally, if $K_v > \approx 2 - 3 \times 10^{-6}$, the flow will get back to a laminar boundary layer.

$$K_v = \frac{4(Per_{heated}/Per_h)q^+}{Re_b} \tag{1.11}$$

$$q^+ = \beta q''_w / G c_p \tag{1.12}$$

1.1.4 Asymmetric heat flux boundary condition applied to microchannels

Half a decade of research about the heat transfer with supercritical carbon dioxide saw a lot of different correlations developed in order to account for the different phenomena that can affect the heat transfer. However, most of them were designed on the basis of macro scale heat exchanger and uniformly heated tubes. It is unknown if those correlations can be used in the case of microchannels with a non uniform heat flux. Moreover the literature does not contain any studies for the specific case of a turbulent heat exchange using supercritical carbon dioxide close to its pseudo-critical point happening in a microchannel-based heat exchanger subject to an asymmetric heat

flux boundary conditions. Some experiments were conducted at Oregon State University by Saad A. Jajja [28; 29] in the last couple years to address this problem.

The first one [28] shows that the general trend of the heat transfer coefficient remains the same than in the other cases. The peak is reached when the pseudo-critical temperature is reached in the boundary layer with the bulk fluid temperature as close to that temperature as possible. An increase of the bulk temperature above the pseudo-critical will lead to a decrease in the heat transfer coefficient. The studies also shows that for a constant mass flow rate, increasing the heat flux will lead to a degradation of the heat transfer coefficient. And for a constant heat flux, increasing the mass flow rate will increase the average heat transfer coefficient. According to the Petukhov and Polyakov criterion, the flow was affected by buoyancy but the experimental results are unable to prove it with certainty as the criterion is for uniformly heated tubes. The same applies for the acceleration effects. Looking at correlations for the heat transfer coefficient, it appears that the best correlation for any case away from the pseudo-critical point is the Dittus and Boelter correlation for constant properties single phase, turbulent flow. However, in the vicinity of the pseudo-critical point the correlation over estimate the heat transfer coefficient. Around the pseudo-critical point, more complex correlations taking into account the sharp property variation in that vicinity give better results but the precision stays low as they are made for uniformly heated tubes.

Later Jajja et al. [29] looks into more detail at the effects of the buoyancy and the acceleration in microchannels by comparing the results for mass flow rates and heat fluxes while applying it from the top or the bottom. It also compares two aspect ratio for rectangular channels and a micro-pin based geometry. With the aspect ratio of one and the experimental conditions used, the orientation of the heat flux had little effect on the heat transfer coefficient even if the Petukhov and Polyakov criterion indicated the clear presence of buoyancy. This might be due to the overestimation of the Grashof number due to the non uniform heating in this case. However, this results do not mean that no buoyancy appears at the local scale but rather that its effect on thermal transport is negligible. Concerning the acceleration, the study shows a greater effect of the acceleration over the low aspect ratio channels. Finally, the micro-pin based geometry gives the best results in term of heat transfer coefficient for a given heat flux and mass flow rate. However, this comes at the cost of a higher pressure drop which is in line with the results of constant property, one phase, turbulent flow.

Some limitations in those studies are the lack of means to determine local results as well as the diffusion of the heat flux in the whole test section leading to around 10-15% of the heat flux being applied from the top. In this work, the new experimental set up here aims to address those problems to continue the research about microchannel heat exchanger with non uniform heat flux using supercritical carbon dioxide. This study also aims to look at the transient response of this setup as the literature is incomplete in that regard too. Therefore the current state of the art of transient heat exchange with supercritical carbon dioxide is done in the following section.

1.2   State of the art of transient heat transfer associated with CO2 supercritical flow

In real applications, as well as in the nature itself, thermal systems more commonly encounter transient regimes than permanent ones. Nevertheless, most of the studies look at steady-state case of convection. This is mostly due to the complexity of the representation of the time-dependant heat exchange compared to the permanent regime.

For supercritical fluids, the literature contains only a handful of papers that looks at time-dependant heat exchange. A part of those papers are mostly looking at pressure transient systems. The main interest comes from the development of new technologies for nuclear reactor such as the Supercritical Water Cooled Reactor (SCWR) to improve the efficiency of power plants. However, before implementing a new technology with nuclear fission as heat source, some studies are needed to assess the security of the technology. One of the main point being pointed out at is the response of the system in a pressure transient state at start-up, shut down but also accidental condition that could cause temporary boiling and lead to some surface temperature increases in the core ([30], [31], [32]). An other interest of the depressurization is the case of a pressure drop through an expansion valve. This interest comes from the application of geothermal energy [33]. However even if the application of the electronics device cooling can potentially be submitted to a pressure drop in the case of a leak or a malfunction of the pressure control system, this study is mainly focusing on transient heat flux or mass flux. Indeed the test bench is not equipped to perform pressure transient tests.

Due to the limited number of existing experimental study in the literature and the complexity to model the transient forced convection with supercritcal [34], most models developed use the knowledge of the steady-state heat transfer. With the low number of studies present in the literature, it is difficult to have a really good idea of the response of the microchannel-based heat exchanger used in this study. Indeed, even the vertical circular tube case is not well known with the supercritical carbon dioxide. Apart from the interest in high temperature in the nuclear [35] or other heat to power conversion system [36], most study looking at a transient heat flux are centered on the response of supercritcal methane [37] or aviation kerosene [38] for regenerative cooling in aerospace propulsion or energy production systems. Those studies reports some small instabilities happening at the start of a transient heat flux but those instabilities stabilize rapidly. Those instabilities and other were linked to the same phenomena than in steady-state namely the buoyancy and the acceleration. The same parameters are also used to determine their impact in [38]. However, it is unclear if the same reaction will be observed in the case of the asymmetric heating applied to supercritical carbon dioxide in a horizontal microchannel heat exchanger.

An other domain that saw some studies is the cooling of superconducting magnet using cryogenic helium [39], however the transient part in cryogenic case is happening of some micro seconds which as little in common with the application studied here.

1.2.1 Modelling of transient convection

Even if the transient response of supercritical system is not well known in the literature, it is interesting to look at the methods used in some papers to model it. But before looking at the modelling of supercritical fluid to some transient heat exchange a small look at the modelling of transient convection using conventional fluid is done. As study was realized by Padet [4] to describe the results observed and to present an approach using the differential form of the equations of conservation (mass, momentum and energy) described as follows:

$$\frac{\partial U}{\partial x} + \frac{\partial V}{\partial y} = 0 \tag{1.13}$$

$$U\frac{\partial U}{\partial x} + V\frac{\partial V}{\partial y} = -\frac{1}{\rho}\frac{dp}{dx} + \nu\frac{\partial^2 U}{\partial y^2} \tag{1.14}$$

$$\frac{\partial T}{\partial t} + U\frac{\partial T}{\partial x} + V\frac{\partial T}{\partial y} = a\frac{\partial^2 T}{\partial y^2} \tag{1.15}$$

Those equation are then completed with the boundary conditions and the initial conditions. Those equations can then be adapted to different systems.

In order to validate the model, the study compares it to some steady-state experiments. Indeed, the steady-state heat exchange is well known compared to the transient heat transfer and the steady-state points are just representing asymptotic solutions of the unsteady problem. This is proved in Fig 1.8 with a step decrease of the plate temperature in Fig. 1.8a and a step increase in Fig. 1.8b. The graphs are plotted using dimensionless temperature $T*$. The parameter R_t is simply equal to the ratio of the plate temperature at the start and at the end. Those figures clearly show that the evolution is indeed asymptotically between the two steady-state point.

The study also shows that the response to an increase in heat flux is slower than a change in the plate temperature. Finally, the effect of the Prandtl number over the transient response is also studied. The results showed that the higher the Prandtl number, the longer the transient response. Applied to the case of supercritical carbon dioxide, the response of the system could be relatively slow as the Prandtl number is at its peak around the pseudo-critical point.

Concerning the modelling of transient supercritical heat transfer, two different approaches were observed in the papers treating the varying heat flux. The first one, described in [36], is a 1D CFD representation of the heat flux using the standard k-ϵ turbulent model described in Eq. 1.16 and 1.17 alongside the laws of conservation. In this paper, the 1D approach is validated in comparison to the 3D CFD approach with a difference of less than 2%. The limitation of the 1D model resides in the inability to represent complex phenomena such as the entry effect. However this comes with the advantage of a much lower computational time.

$$\frac{\partial(\rho k)}{\partial t} + \nabla.(\rho\vec{U}k) = \nabla.\left[\left(\mu + \frac{\mu_t}{\sigma_k}\right)\nabla k\right] - \rho\epsilon + G_k \tag{1.16}$$

(a) Negative step change in the plate temperature

(b) Positive step change in the plate temperature
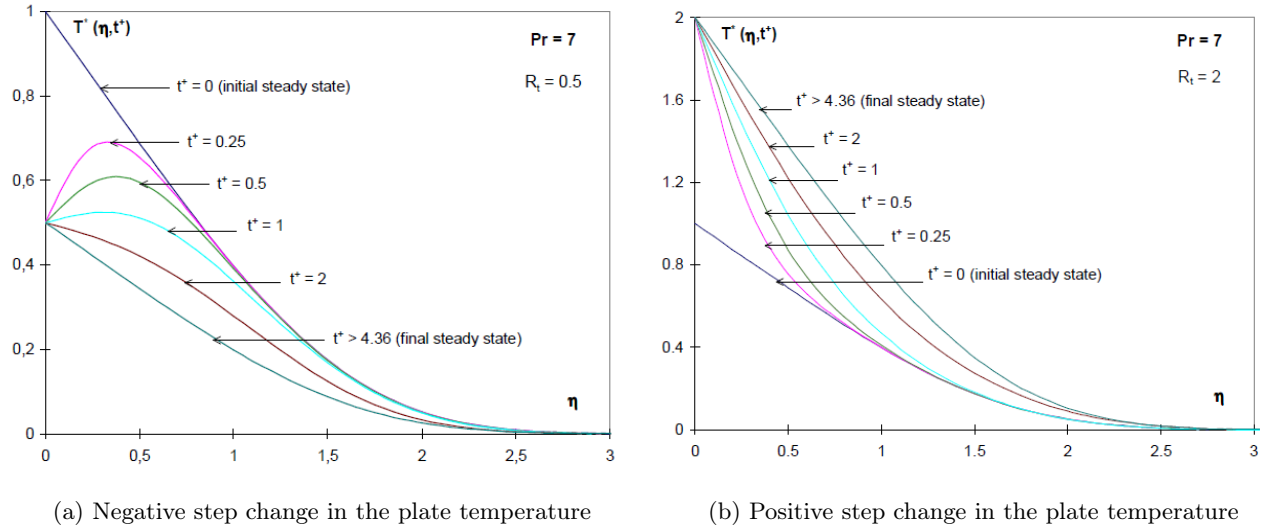
Figure 1.8: Transient temperature profile [4]

$$\frac{\partial(\rho\epsilon)}{\partial t} + \nabla.(\rho\vec{U}\epsilon) = \nabla.\left[\left(\mu + \frac{\mu_t}{\sigma_\epsilon}\right)\nabla\epsilon\right] - C_1\frac{\epsilon}{k}G_k - C_2\rho\frac{\epsilon^2}{k} \tag{1.17}$$

The second approach, described in [35], is a simplified method first developed by Sharifi et al. [40] using energy balance equations. Those equations use the heat capacity rate for the fluid defined as: $C = \dot{m}c_p$ to determine the evolution of the fluid temperature in time. This can be also applied with the solids by changing the mass flow rate by the mass of the finite element of the solid. In the case of the study, the system represented is a counter-flow heat exchanger and the energy balance equations for the fluid on both side and the plate are respectively:

$$\rho_{hot}c_{p,hot}\frac{\partial T_{hot}}{\partial t} + \rho_{hot}c_{p,hot}U_{hot} = -\frac{T_{hot} - T_{plate}}{R_{conv,hot}} \tag{1.18}$$

$$\rho_{cold}c_{p,cold}\frac{\partial T_{cold}}{\partial t} + \rho_{cold}c_{p,cold}U_{cold} = \frac{T_{plate} - T_{cold}}{R_{conv,cold}} \tag{1.19}$$

$$\rho_{plate}c_{p,plate}\frac{\partial T_{plate}}{\partial t} = \frac{T_{hot} - T_{plate}}{R_{conv,hot}} - \frac{T_{plate} - T_{cold}}{R_{conv,cold}} \tag{1.20}$$

In this work, the second method will be adapted with a 1D representation known to be good (with its limitation) thanks to the study of Marchionni [36]. This method fits well with the heat exchanger with an asymmetric heat flux boundary condition. Indeed, the representation of the energy balance of the counter-flow heat exchanger representation assumes a single dimension heat exchange between the two fluid leading to an asymmetric heat flux.

1.3 Objective

This work aims to analyse the heat exchange in a horizontal microchannel heat exchanger using supercritical carbon dioxide (s-CO$_2$) as working fluid. This heat exchanger is heated only by its bottom layer, the other sides being insulated. This is therefore a turbulent heat transfer with an asymmetric heat flux boundary condition. This geometry with the asymmetric boundary condition is tested for the first time. The different tests are performed in the Thermal Energy Systems and Transport (TEST) Laboratory at Oregon State University. The main interest of this particular research is to manage high heat flux [28],[13] such as the cooling of electronics that need a thermal management for high heat flux at relatively low temperatures.

The test section is part of a loop enabling the control of the different parameters (temperature, pressure and mass flux) at the inlet of the heat exchanger to ensure the presence of the pseudo-critical point inside the test

section. In order to have data all along the channel, an infrared camera is used. It enables a local study of the temperature and with some post processing the heat transfer coefficient as well. The steady state experimental part aims to determine the influence of the different parameters over the heat transfer. After the steady state experimental part, the heat exchanger is tested in transient conditions to look at the response of the system to different perturbations. In addition to the experimental part, this work aim to develop a predictive model of the test section first in steady state and then in transient regime using the electrical circuit analogy. In short, the different objectives can be summarized as follows:

1. Testing the heat exchanger with the carbon dioxide close to the pseudo-critical point in a steady-state heat exchange and compare the results to the literature.

2. Testing some transient heat exchange with the carbon dioxide close to the pseudo-critical point.

3. Developing a predictive model for the heat exchanger in steady-state condition and compare the prediction to the experimental results.

4. Developing a predictive model for the heat exchanger in transient condition and compare the prediction to the experimental results.

1.4 Overview

An overview of the present work can be described as follows:

- Chapter 2: the experimental setup, used to perform steady-state convection, with the different components of the loop and the measurements devices are first described. Then, the experimental results are analysed.

- Chapter 3: the experimental setup modifications for the transient experiments are explained with the new data acquisition procedure. Some transient tests are then performed and analysed

- Chapter 4: a predictive model of the heat exchanger in steady-state regime using an electrical representation is described. The different correlations possible to determine the heat transfer coefficient in convection are then compared to the experimental data. Finally, the results of the model are exposed and analysed.

- Chapter 5: a predictive model of the heat exchanger in transient regime is described. Using the same correlation to compute the heat transfer coefficient than in chapter 4, the results of the model are directly exposed and analysed.

- Chapter 6: the different results presented in this work are summarised and a conclusion is drawn. Some suggestions for future works are also presented.

Chapter 2

Experimental testing of heat transfer in steady state

2.1 Experimental setup

The experimental part was conducted in the Thermal Energy Systems and Transport (TEST) Laboratory at Oregon State University. The test setup was designed to analyse the heat transfer inside the test section. The rest of the loop is only used to control the different parameters (mass flux, inlet temperature, absolute pressure) at the inlet of the test section.

2.1.1 Test stand

The test stand can be seen in Fig. 2.1 with a scheme in Fig. 2.1a and the actual picture in Fig. 2.1b. The test stand is composed of four main components, the gear pump, the pre-heater, the test section and a tube-in-tube cooler.

(a) Schematic   (b) Picture
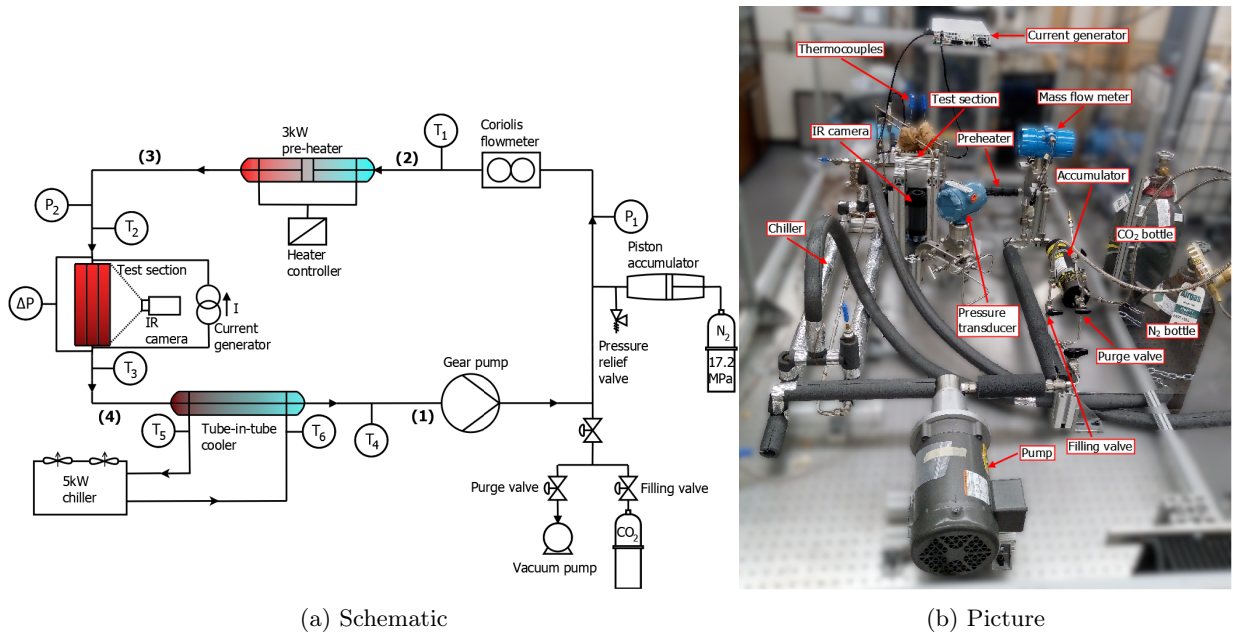
Figure 2.1: Test stand

The loop can be described by the four different states of the fluid. At the exit of the cooler and before the pump, the fluid is in a "liquid-like" state as its temperature is lower than the pseudo-critical temperature. The fluid

then goes through a gear pump that acts here as a simple circulator as the whole loop is at a single supercritical pressure set by a 0.95 L piston driven accumulator linked to a 17.2 MPa (2500 Psi) nitrogen tank equipped with a high-pressure regulator. The accumulator is further equipped with a pressure relief valve to reduce the pressure in the nitrogen part and with that reduce the pressure in the whole loop. After the pump, the fluid goes through a Coriolis flowmeter before entering a 3kW pre-heater used to have the carbon dioxide at the desired temperature before the test section. The test section itself is connected to a current generator to control the heat flux applied on the bottom plate of the heat exchanger. The carbon dioxide gets out at the highest temperature in the loop generally in a "vapor-like" state. Finally, the carbon dioxide is cooled down in a tube-in-tube cooler linked to a 5kW chiller to return to a "liquid-like" state. The evolution of the carbon dioxide in the loop can also be seen in the P-h diagram in Fig. 2.2. In order to have a better vision of the evolution, the pressure drop in the different components was exaggerated. In reality, the pressure increase between the state (**1**) and (**2**) is smaller as the pump act as a circulator.
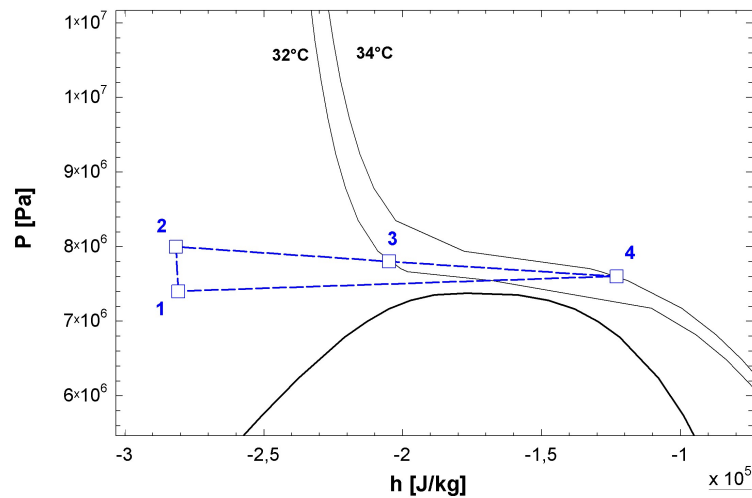
Figure 2.2: Electrical resistivity of different materials

The different measurement devices and their position are also represented in the figure. A notable measurement device is the infrared camera used to measure the wall temperature of the test section. This method was chosen in order to be able to develop a predictive model which required the knowledge of local heat transfer coefficient along the channel. All components are depicted in Fig. 2.1b and will be described in more detail in the following sections.

2.1.1.1 Test section

The test section is a heat exchanger composed of three microchannels and Joule heated by a metallic sheet used as bottom layer of the heat exchanger. The metallic sheet was connected to a current generator by two copper electrodes. In order to be as close as possible of the ideal case desired with the fluid heated only on the bottom wall, the channels are machined in Torlon plastic. Below the Inconel sheet, a layer of Torlon is also used in order to have insulating materials on every side of the heat-exchanger. This plastic was used due to its thermal and electrical insulating properties. Moreover, contrary to other plastic, the Torlon can be used at high temperature as its glass transition temperature is around 270°C. The test section is then completed with a gasket to prevent any leakage and finally two stainless steel plate held in place with 24 screws to sustain the high pressure. In order to use the infrared camera, a view port in the bottom layers was added and the metallic sheet was painted in black. All the different part of the test section can be seen in Fig. 2.3a with the specifications of the geometry in Tab. 2.1. Its place in the loop with the inlet/outlet ports and the connections to the current generator can be seen in Fig. 2.3b.

In order to perform the different testing with the best precision, it is necessary to have a low variation in the electrical resistivity of the metallic layer at the bottom. Indeed, the Joule heating being proportional to the resistivity, a constant heating flux along the channel can only be reached with an adequate material. With that in mind, the Inconel 718 was chosen. As can be seen in Fig. 2.4, its electrical resistivity only increase by 4.8%

(a) Dismantled test section   (b) Mounted test section
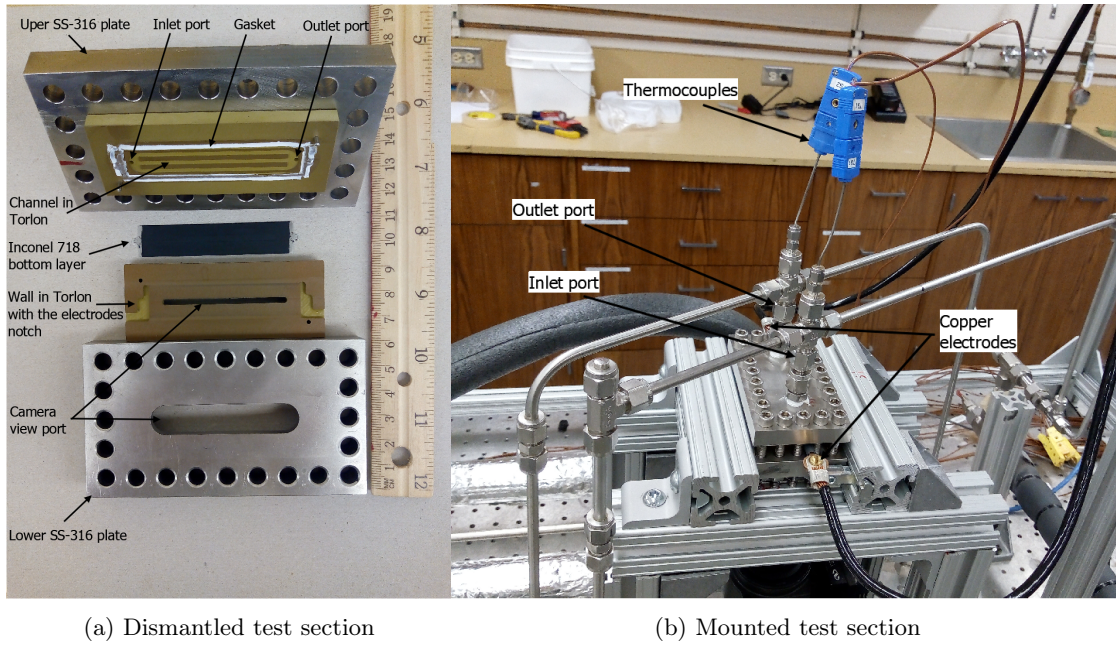
Figure 2.3: Test section used for the different experiences

Thickness of the Inconel sheet	254 µm
Length of the channel	50 mm
Length of the header (inlet/outlet)	7 mm
Height of the channel	600 µm
Width of the channel	1.92 mm
Aspect ratio of the channel	3.2
Number of channel	3
Thickness of the channel side wall	1.5 mm
Thickness of the outer edge	1.5 mm

Table 2.1: Geometrical specification of the channels and the Inconel sheet

between 20°C and 250°C compared to the stainless steel that see a 20.4% increase or the aluminum with its near 100% increase. The expected temperature of the Inconel being between that range, as higher temperature would compromise the use of Torlon, the constant heat flux along the channel is approached with a decent accuracy.

2.1.1.2 Current generator

The current generator is used to apply the desired heat flux to the test section by Joule effect is a GENESYS model GENH 6-100. Its specifications are given in Tab. 2.2. As the power induced inside the test section is computed only with the current and the electrical resistivity of the Inconel sheet, the error on the voltage output does not need to be considered. This method also reduces the error as the copper wire is also responsible for a part of the voltage.

Rated output voltage	6V
Rated output current	100Amp
Rated output power	600W
Output current error	±1% of reading

Table 2.2: Current generator specifications [8]
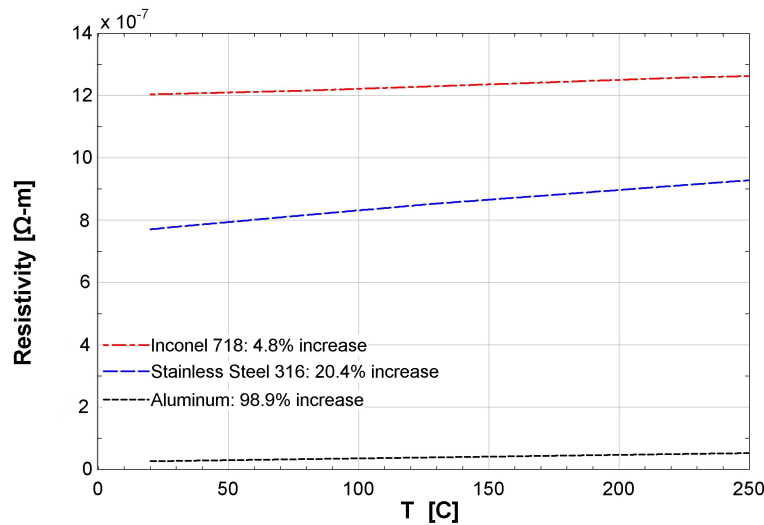
Figure 2.4: Electrical resistivity of different materials

2.1.1.3 Pre-heater

The pre-heater, used to adjust the temperature at the inlet of the test section, is composed of a couple SCR (PAYNE Engineering) controlled 1.5 kW cartridge heater elements. Those elements are isolated from the sCO_2. A high temperature silicon foam is used to isolate the pre-heater assembly.

2.1.1.4 Cooling system

The cooling system used to compensate the heat flux in the pre-heater and in the test section is a tube-in-tube counter-flow heat-exchanger. The heat exchanger consists of a couple of tubes put in series as shown in Fig. 2.5a. The hot carbon dioxide coming from the test section enters the center of the tube while the chilled 50-50% glycol-water flows in the annulus. That mixture is then cooled down in a Neslab Merlin recirculating chiller (Model M150) used for low temperature cooling. This model is a 5kW chiller with a temperature range of 5-35°C, it can be observed in Fig. 2.5b.
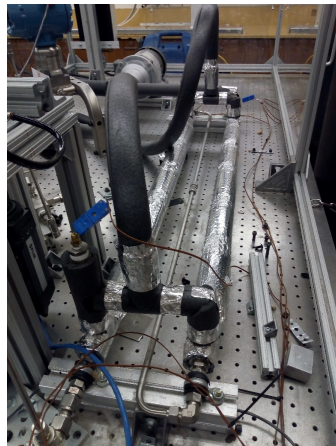
(a) Cooler in the test loop   (b) Air chiller

Figure 2.5: Cooling system

2.1.1.5 Pump

The pump used in the loop is a magnetically driven gear pumps (Model GC-M23) [41] shown in Fig. 2.6. The magnetic drive allows for a pulseless flow. It is only used as a circulator as no turbine or other expansion devices

are present in the loop.
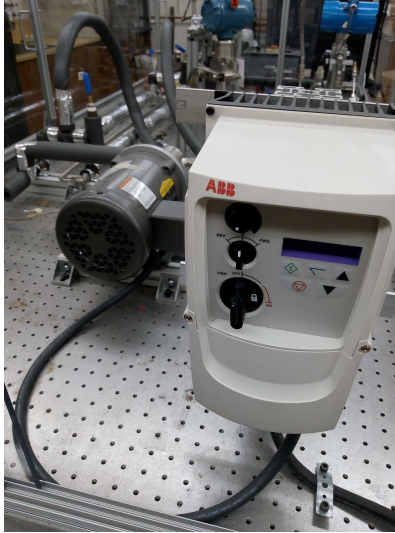
Figure 2.6: Pump

2.1.2 Measurement devices

2.1.2.1 Thermocouples

In order to measure the different temperatures, T-type thermocouples (Copper/Constantan) with a nominal uncertainty of $\pm$ 0.5°C or 0.4% are used. The thermocouples are widely used because of their cost-effectiveness and the wide temperature range that they cover. The working principle is based on the Seebeck effect. This phenomenon explains the generation of an electromotive force if two different metals are joined together at two junctions that are at different temperatures. Both the temperature difference between the junctions and the combination of materials will affect the electromotive force [42]. Every combination is characterized by a range of temperatures and a tolerance which define the differences between the types of thermocouples. The electromotive force induced in a thermocouple is given by:

$$\Delta E = \int_{T_1}^{T_2} S_a - S_b \ dT \tag{2.1}$$

S_a and S_b are the Seebeck coefficients characterizing both metals used. As the thermocouple is only measuring the difference of temperature, it is necessary to know the reference temperature T_1 in order to determine the desired temperature T_2. This is done thanks to a built-in cold junction inside of the Data Acquisition DAQ NI-9214 that enables the creation of the reference temperature needed by the thermocouples. More information about the Data Acquisition are presented in section 2.1.2.5.

2.1.2.2 Pressure transducers

The pressure is measured at two places in the loop. After the pump, the gauge pressure is measured using an OMEGA current output transducer (Model PX-309-3KGI) depicted in Fig. 2.7 with a nominal uncertainty of 0:25% FS and range of 0–20.7 MPa (=0-3000Psi) [43]. This sensor works using the semiconductor strain gages that make use of the piezoresistive effect of the silicon in a Wheatstone bridge as shown in Fig. 2.8. With the deformation of the silicon membrane, the resistance of the fourth branch will change creating a imbalance in the bridge and creating a potential difference between the point B and D. Generally used with metal film, the use of semiconductor enables a higher sensitivity in the bridge.

The second pressure transducer present in the loop, a Rosemount (Model 3051 SMV) with a range of 0–24.8MPa (3600psi), measures the absolute sCO_2 pressure at the inlet of the test section. It also measures the pressure drop inside the test section for a range of 0 to 62.2 kPa.

Figure 2.7: OMEGA pressure transducer
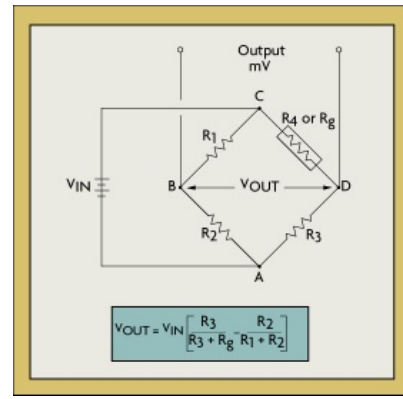
Figure 2.8: Wheatstone bridge

Figure 2.9: Rosemount pressure transducer

2.1.2.3 Supercritical fluid mass flow meter

The mass flow rate of supercritical fluid is measured using a Coriolis flow meter immediately after the pump with a current output, nominal uncertainty of 0.1% of reading, and range of 0–325 kg/h. A representation of the mass flow meter can be seen in Fig. 2.10 with the different elements present inside the device.

The working principle is simple, the two tubes are oscillating and are in phase as long as there is no flow. When the fluid goes through the tubes, the tubes twist due to the Coriolis effect. This deformation will create a phase shift between the two vibration as depicted in Fig. 2.11. This phase shift is directly proportional to the mass flow rate and this time difference is converted into a mass flow rate.

2.1.2.4 IR camera

As the primary goal of this study is to look at the heat transfer coefficient inside the test section, the knowledge of local temperature was needed. For that reason, an IR camera was installed bellow the test section that was designed with a view port as previously shown in Fig. 2.3a. The camera used is a FLIR model A325sc. Its resolution is 320 by 240 pixels and the accuracy is $\pm$ 2°C or $\pm$ 2% of reading.

In order to have the results with an IR camera, some principles must be followed. As the camera receives and analyses the radiations emitted, any cavity must be avoided and the lens must be orthogonal to the studied plate to increase the point of view between the surface and the lens. The distance between the lens and the surface must be known in order to set the focal distance. Concerning of radiation, the emissivity of the studied surface must be as high as possible and must be known, in this case the Inconel sheet was painted in black to have an emissivity of
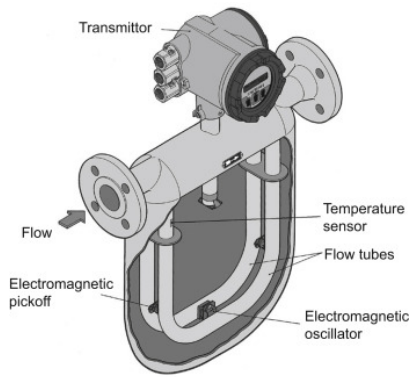
Figure 2.10: Mass flow meter [5]   Figure 2.11: Measurement using the Coriolis effect
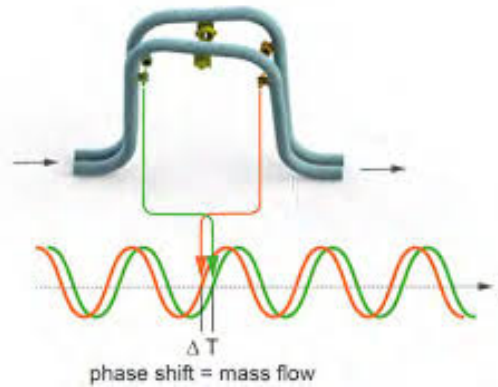
0.95. Any metallic pieces must be avoided close to the surface to reduce the reflection that could alter the results of the analysis. Finally, in order to have a good contrast between the channel and the surrounding, the view port was surrounded by a sandblasted aluminum sheet to have a low emissivity material around the studied plate.

Finally, in order to have good results, the IR camera must be calibrated using a black body. This procedure will be described in more detail in section 2.2.2.

2.1.2.5 Data acquisition

The measurement devices producing analog signal output (under the form of voltage or current), a Data Acquisition (DAQ) system is needed to convert those signals to digital signal (analog-to-digital converter) that the computer can analyse in a LabView model.

The data from the transducers are acquired using a National Instruments compact data acquisition chassis (Model NI-cDAQ-9174). To complement that chassis, some National Instruments (Model NI-9205, NI-9211 and NI-9203) are used to acquire either a current analog input (NI-9203) and change it into a voltage output with a resistance or a voltage input (NI-9205, NI-9211). In this case, the mass flow meter sends a current output and the pressure transducers and thermocouples use voltage output. Finally a 16-channel thermocouple input module (Model NI-9214) is used to produce the reference temperature with a build-in cold junction needed by the thermocouples. All the signals are then sent to the computer by an USB cable and are treated inside of a LabView model. The goal of the LabView model is to convert back the digital signals into physical value thanks to thermodynamical and mathematical relationships using different correlations that are calibrated with the different measuring devices.

2.2 Experimental results

2.2.1 Procedures

In order to perform the different experiments in the best conditions, it is necessary to follow some basic procedures. Indeed with the high pressure, it is important to keep the test stand safe and avoid endangering people.

2.2.1.1 Static pressure test

The first test to carry out is the static pressure test on the test section itself. Once all screws and bolts are tightened, the test section is put under high pressure using the high pressure regulator of the nitrogen bottle. The test section is put under a pressure of up to 9 MPa to make sure the gasket is well in place and the bolts are tightened enough. In order to see if a leak is present, the test section under pressure is simply immersed in water to see if bubbles are created. As the experiments will always stay bellow that pressure, this test shows that the test section itself is not responsible for potential leakage once it is mounted on the test stand.

2.2.1.2   Charging the system with CO2

Once the test section is tested and mounted on the test stand, the loop can be filled with carbon dioxide. In order to do that some steps need to be followed:

1. Use a vacuum pump to remove the air from the system

2. Close the valves of the pressure sensor to avoid any damage with the rapid pressure change when the saturated CO_2 is added

3. Charge the system with saturated CO_2 (around 6.4 MPa at 25°C)

4. Reopen the valves at the pressure sensor to check if it is indeed liquid

The first step serves a two-fold goal. The first is to detect if a leak is present in the loop. If one is present, a refrigerant is injected in the loop and a gas sensor is used to detect the leak and fix it. The second goal of the vacuum pump is lowered the pressure enough to avoid the dilution of the carbon dioxide with air during the filling. If too much air is present, it will be impossible to increase the pressure later as the CO_2 will be in a gaseous state instead of a liquid one.

Once the loop is filled, the filling valve is closed and the pressure in the loop can be increased with the piston driven accumulator and the high pressure regulator linked to the nitrogen bottle to reach a supercritical pressure.

2.2.1.3   Pressure drop test

Once the loop is at a supercritical pressure, it is possible to start the different devices of the loop. For obvious reasons the pump and the cooling system must be activated before the pre-heater or any heating up of the test section. The mass flow rate must stay high enough at any time to avoid an overheating in the test section and the melting of the Torlon.

The last thing to do before starting any heating is to make a pressure drop test in the test section. This test is necessary to verify that the gasket inside the test section did not enter the channels. This would reduce the space where the fluid can go through, increasing the pressure drop and more importantly change the flow distribution between the three channels. This would create errors in the data analysis as only the center channel has its local temperature measured with the IR camera.

As the pressure drop is not measured directly in the test section, the total pressure drop is equal to the sum of pressure loss inside the channel with the different minor losses present at the inlet and outlet. The total pressure drop is described by Eq. 2.2.

$$\Delta_{P,measured} = \Delta_{P,fric} + \Delta_{P,acc} + \Delta_{P,minor} \tag{2.2}$$

The different minor losses taken into account the tubing between the sensor and the test section, the different bending in the tube, sudden expansion or contraction,... The position of those different losses is represented in Fig. 2.12. The pressure drop due to the acceleration of the fluid ($\Delta_{P,acc}$) is not taken into consideration in the case of the pressure drop test as the test is adiabatic. In addition to neglecting the pressure drop due to acceleration, doing an adiabatic test removes the problems of the fluid properties taken at the film temperature or the bulk fluid temperature as those temperatures are equals. Once all the losses have been computed, the minor losses are deducted from the measured losses to only look at the friction losses inside the channels. The description of the pressure drop model can be found in details in Appendix B.

The pressure drop test is performed with different mass fluxes to evaluate the losses at different Reynolds numbers and the results are shown in Fig. 2.13. The pressure losses measured are represented with their respective uncertainty errors (uncertainty of the pressure transducer but also the uncertainty on the minor losses) and as can be seen, the theoretical line is within the range of the uncertainty. As the pressure drop is valid, the tests with a heat flux can be performed.
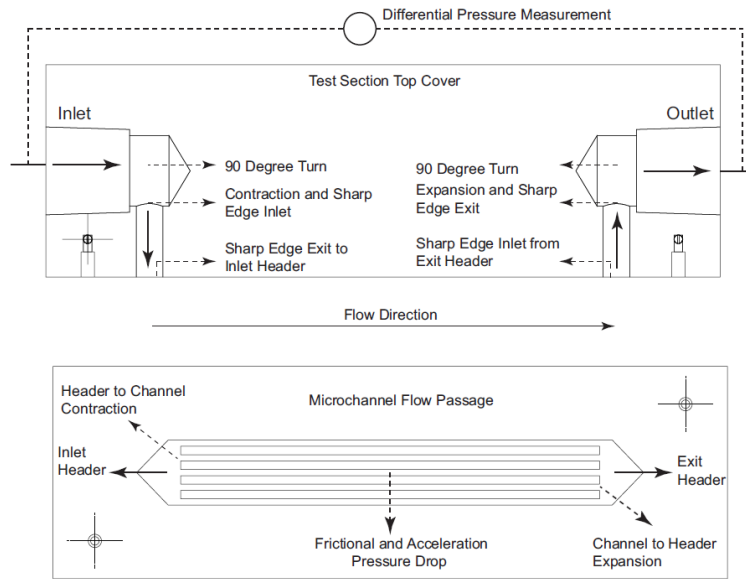
Figure 2.12: Flow path of the carbon dioxide for the pressure drop analysis

2.2.2 Calibration of the camera

Just like different measurement devices, the IR camera needs to be calibrated in condition as close to the actual testing as possible:

- Use of a black body as reference.

- Put the camera at the same distance than for the actual test section (+- 15cm).

- Select the emissivity of the body (for the black body 0.999 was used), for the paint the best way is to have data from the producer of the paint (0.95 in this case).

- Impose a reflected temperature (set at the room temperature: 20°C).

- Select the good configuration of the lens in place on the camera (here 18mm).

- Select the good range temperature that will present during the testing. A too wide range will lead to less precise results but a temperature higher than the maximum temperature range will lead to an overflow and a wrong measured temperature.

Once those parameters are fixed, the black body can be used to verify the good calibration of the camera. In order to do that, the black body is set to given temperatures and the results given by the camera is compared to this temperature. As shown in Fig. 2.14, the camera sees the black body as a circle and the temperature of the zone is not perfectly even. To compensate that, the temperature taken into account for the calibration is a mean temperature of an area of interest. This area of interest of the black body is defined by the zone where the standard deviation is equal to 1%. In other words, the results of Eq. 2.3 must be equal to 1% of the mean temperature. In this equation are present: N the number of points in the area, x_i the temperature of the local point and μ the mean temperature.

$$\sigma = \sqrt{\frac{1}{N} \sum_{i-1}^{N} (x_i - \mu)^2} \tag{2.3}$$
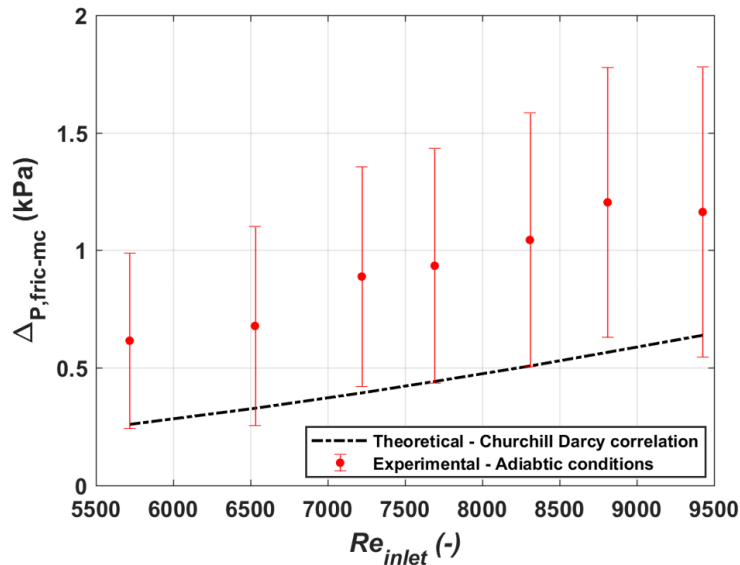
Figure 2.13: Pressure drop validation

2.2.3 Analysis of the IR camera image

The primary goal of the study being the determination of the local convective heat transfer coefficient along the channel, the local temperatures given by the camera are the primary measures. In order to go from an image like Fig. 2.15 with local temperatures to heat transfer coefficient, an analysis is needed. During the steady state analysis, those local temperature are taken as the mean temperature of 5 IR images to improve the repeatably of the different tests.

The first step before any analysis is to determine the pixels that constitute the channel. A first raw selection can be seen in the white box in Fig. 2.15. A more detailed view of that zone of interest can be seen in Fig. 2.16. From that zone of interest, the inlet (X=291) and outlet (X=39) are easily determined thanks to the temperature gradients between the Inconel foil and the Torlon around it. The problem was to determine the pixels across the channel as the channel is not perfectly straight. To be as precise as possible, the assumption of symmetry across the channel was made. The extreme points are the ones with the closest temperature while being separated by 12 pixels (number determined with the geometry and the size of the pixel in that axis). After it was done all along the channel, the selection was finally refined by removing 5 columns (along the axis) and 2 rows at each side as the view port was longer and wider than the channel and shows a part of the headers and a part of the Inconel below the side walls.

The area of the channel being now selected, the next step was to set the boundary conditions on the sides of the channel as well as the inlet and outlet. Those conditions were:

- Constant heat flux on the side with half of the heat produced between two channels (or all the heat produced between the channel and the edge of the heat exchanger) applied to the side of the channel. It means that for an indicated heat flux of 5 W/cm^2, the effective heat flux will be higher as the heat produced in the side walls and edges goes to the carbon dioxide through the bottom as well thanks to the perfect insulation. Looking at the geometry, the heat flux can be considered to be doubled.

- The carbon dioxide temperature at the start of the channel is determined by an energy balance over the header region.

- The carbon dioxide temperature at the outlet of the test section is determined by an energy balance over the header region.

With the boundary conditions set, the balance of the elements can be described and a representation of the situation is shown in Fig. 2.17. The axes are oriented with the y-axis along the channel, the x-axis across it and the z-axis perpendicular to the plane of the Inconel sheet. As the sheet is really thin (254μm), the possibility to
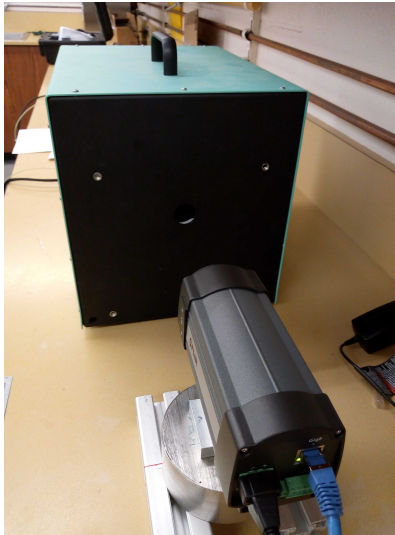
Figure 2.14: Calibration of the camera with a black body
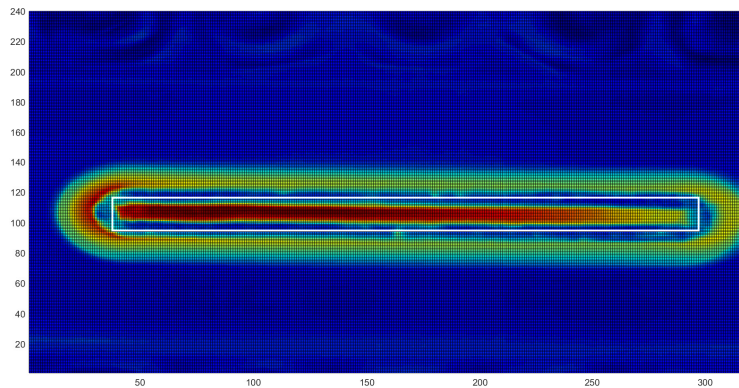
Figure 2.15: Global view of an IR image

neglect the conduction along the z-axis was studied with the use of the Biot number. This dimensionless parameter, described in Eq. 2.4, shows the importance of the conduction inside the solid compared to the forced convection between the fluid and the surface. In other words, for a low Biot number the temperature in the middle of the solid can be assumed equal to the surface temperature. The threshold value for this assumption is $Bi < 0.1$ [44]. After some testing with different currents (=different heat flows) applied, the value of the Biot number never goes above 0.05 which is well bellow the threshold and neglecting the conduction along the z-axis is therefore a valid assumption.

$$Bi = \frac{h_{conv}Th_f/2}{k} \tag{2.4}$$

With the conduction being neglected and looking at Fig 2.17, the energy balance in the steady state case can be described by Equation 2.5

$$q_{cd,x} + q_{cd,y} + \dot{E}_{gen} - q_{cd,x+dx} - q_{cd,y+dy} - q_{fc} - q_{rad} = 0 \tag{2.5}$$

In this equation, the two first terms respectively represent the heat coming into the element through conduction perpendicular to the surface in the x and y directions. They can be described using Fourier's law [44]:
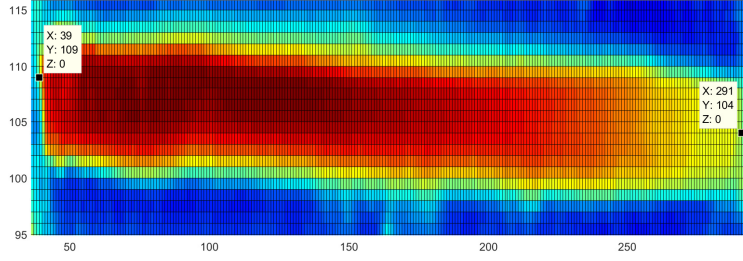
Figure 2.16: Zone of interest in the IR image

$$q_{cd,x} = -k \ Th_f.dy \frac{\partial T_m}{\partial x} \tag{2.6}$$

$$q_{cd,y} = -k \ Th_f.dx \frac{\partial T_m}{\partial y} \tag{2.7}$$

The different terms present here are obviously the conductivity of the material k, the measured temperature of the Inconel T_m and the geometrical dimensions. Two other conduction terms are found in Equation 2.5 and represent the heat leaving the element. Those two terms can be seen as the conduction at rate that comes in x or y directions with the additional term of its change over the distances dx or dy:

$$q_{cd,x+dx} = q_{cd,x} + \frac{\partial q_{cd,x}}{\partial x} dx \tag{2.8}$$

$$q_{cd,y+dy} = q_{cd,y} + \frac{\partial q_{cd,y}}{\partial y} dy \tag{2.9}$$

Substituting the different terms from Equations 2.6 to 2.9 into Equation 2.5 gives:

$$k \ Th_f \left(\frac{\partial^2 T_m}{\partial x^2} + \frac{\partial^2 T_m}{\partial y^2} \right) dx.dy + E_{gen} - q_{fc} - q_{rad} = 0 \tag{2.10}$$

Outside of the conduction, the element is subject to three other terms. The first one, E_{gen}, is the heat generated inside the Inconel by the current flowing through it. The current flow along the x axis can simply be described by the Joule heating equation where γ represents the electrical resistivity:

$$E_{gen} = I^2 \frac{dy \ \gamma}{dx \ Th_f} \tag{2.11}$$

The second term, q_{fc} represents the heat leaving the element through forced convection by the supercritical carbon dioxide inside the channel. As the goal is to determine the convective heat transfer coefficient h, the convective heat transfer is at first expressed using the Newton's law of cooling [44]:

$$q_{fc} = h \ dx.dy(T_m - \bar{T}_{sCO_2}) \tag{2.12}$$

$\bar{T}_{sCO_2}$ represent the mean bulk temperature of the fluid inside the channel. Then, using the energy balance of the element, it is expressed with regards to the other exchanges in Equation 2.13:

$$h = \frac{q_{cd} + E_{gen} - q_{rad}}{dx.dy(T_m - \bar{T}_{sCO_2})} \tag{2.13}$$
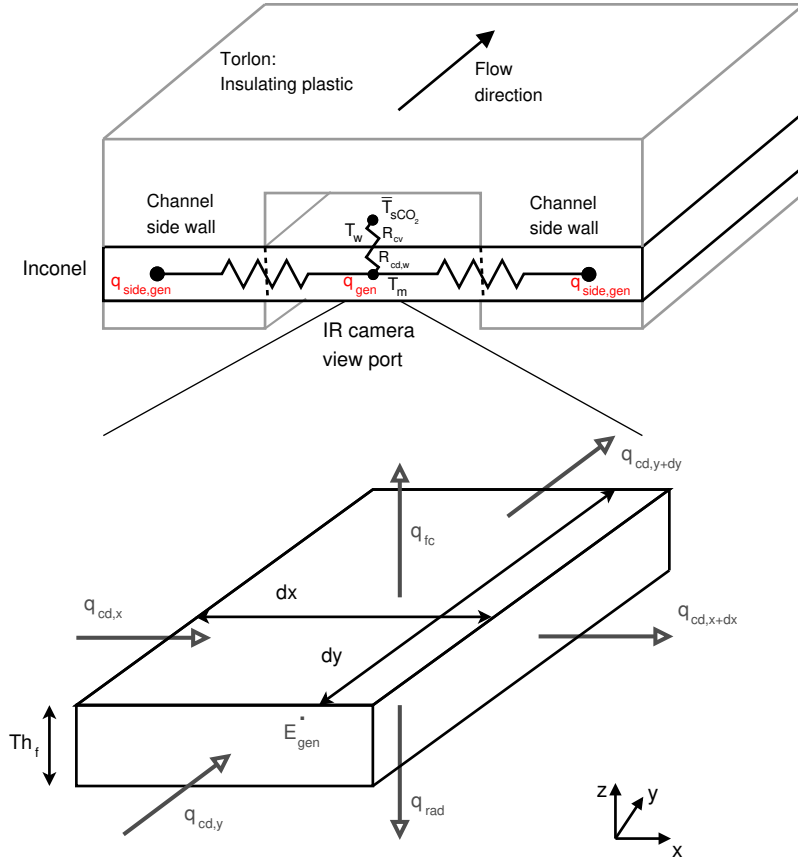
Figure 2.17: Energy balance in an element [6; 7]

Finally, the last term q_{rad} is the radiation emitted by the bottom face of the Inconel to the ambiance and that was painted in black in order to know the emissivity ϵ ($\approx 95\%$) of the surface for the IR camera measurements. The heat exchange is expressed as a single exchange with the ambiance described by its temperature T_∞. The other terms are the Stefan–Boltzmann constant σ and the wall temperature T_m.

$$q_{rad} = \epsilon \sigma dx.dy(T_m^4 - T_\infty^4) \tag{2.14}$$

Using Equations 2.10, 2.11 and 2.14 in Equation 2.13, the new expression to calculate the convective heat transfer coefficient becomes:

$$h = \frac{k\ Th_f \left(\frac{\partial^2 T_m}{\partial x^2} + \frac{\partial^2 T_m}{\partial y^2} \right) - \epsilon \sigma (T_m^4 - T_\infty^4)}{(T_m - \bar{T}_{sCO_2})} + \frac{I^2 \gamma}{dx^2\ Th_f\ (T_m - \bar{T}_{sCO_2})} \tag{2.15}$$

With this expression, the value of the convective heat transfer coefficient can be computed everywhere once the boundary conditions are set. Indeed the different terms are either known through measurements or computed in the model. The last needed equation is the one to approach the second derivative of the temperature in space. In order to be as precise as possible, a fourth order central differentiation approximation of that second derivative is used [45]:

$$\left(\frac{\partial^2 T}{\partial x^2} \right)_i = \frac{-T_{i-2} + 16T_{i+1} - 30T_i + 16T_{i+1} - T_{i+2}}{12(\Delta x)^2} + \mathcal{O}(\Delta x)^4 \tag{2.16}$$

This detailed description of the energy balance was theoretically the best one to get good results. However, due to the low number of points along the channel and even lower number across it, the temperature gradient between

some pixels was huge leading to spikes in the heat transferred by conduction. Those peaks were even enhanced by the selection of the point due to the oblique orientation of the channel compared to the image. Indeed, the temperature gradient was even greater at the different points where the selection jumped from one line of pixels to the other. Taking that into consideration but also the small impact that the conduction should have with the thickness of the plate, the conductions in both x and y directions were neglected. The data validation will show in further sections that the results are better with the conduction neglected and all the oscillations that it produces. Finally, with the conduction out of the equation, the analysis becomes easier with no approximation needed:

$$h = \frac{E_{gen} - q_{rad}}{dx.dy(T_m - \bar{T}_{sCO2})} = \frac{I^2\gamma}{dx^2 \, Th_f \, (T_m - \bar{T}_{sCO_2})} - \frac{\epsilon\sigma(T_m^4 - T_\infty^4)}{(T_m - \bar{T}_{sCO_2})} \tag{2.17}$$

However, as the conduction is removed, the heat generated below the side walls and the edges ($E_{gen,sw}$) needs to be accounted for differently. This energy is computed using Eq. 2.11 but with the corresponding geometrical values. In order to keep it simple, the heat was added equally all across the channel. In reality, more heat will go to the fluid close to the walls but as the local heat transfer coefficient is not looked at across the channel, this assumption does not change the results. Finally, as the heat exchanger presents 2 edges and 2 side walls for 3 channels, it is assumed that all the heat produced under the edges and the side walls is equally divided between the there channels, resulting in a 4/3 factor in front of $E_{gen,sw}$. Therefore the final equation becomes as follows and the code can be found in Appendix A:

$$h = \frac{E_{gen} - q_{rad}}{dx.dy(T_m - \bar{T}_{sCO2})} = \frac{I^2\gamma}{dx^2 \, Th_f \, (T_m - \bar{T}_{sCO_2})} + \frac{4}{3}E_{gen,sw} - \frac{\epsilon\sigma(T_m^4 - T_\infty^4)}{(T_m - \bar{T}_{sCO_2})} \tag{2.18}$$

2.2.4 Uncertainty analysis

Using the different information in the data sheets of all the devices including the Data Acquisition, it is possible to determine the uncertainty on the different measures. From those uncertainties, the sequential perturbation method is used to determine their influence on the different variables. This method assumes that the different measured variables are uncorrelated, meaning that their influence is taken separately with a finite approximation error (u_i). The variable is therefore sequentially perturbed by the uncertainty of all measures (x_i) influencing that variable. Its global perturbation (u_R) is the root mean square value of the different perturbation error (D_i) as described in Eq.2.19. This method is applied to the different variables in different MATLAB functions. The uncertainties of the different measurement devices are summed up in Tab. 2.3.

$$u_R = (D_1^2 + D_2^2 + D_3^2 + ... + D_n^2)^{0.5} \tag{2.19}$$

$$
\begin{aligned}
D_1 &= f(x_1 + u_1, x_2, x_3, ..., x_n) - f(x_1, x_2, x_3, ..., x_n) \\
D_2 &= f(x_1, x_2 + u_2, x_3, ..., x_n) - f(x_1, x_2, x_3, ..., x_n) \\
D_3 &= f(x_1, x_2, x_3 + u_3, ..., x_n) - f(x_1, x_2, x_3, ..., x_n) \\
&\vdots \\
D_n &= f(x_1, x_2, x_3, ..., x_n + u_n) - f(x_1, x_2, x_3, ..., x_n)
\end{aligned}
$$

Sensors	Uncertainties	Total uncertainty
Thermocouples	Special uncertainty	±0.5K
Gauge pressure sensor	Sensor accuracy: 0.25% FS Conversion error: 1% reading	0.25% FS + 1% reading
Absolute pressure sensor (Pin)	Absolute uncertainty	±20 kPa
Pressure difference	Absolute uncertainty	±0.12 kPa
Mass flow rate	Sensor accuracy: 0.1% reading DAQ accuracy 0.06%FS	0.06%FS + 0.1% reading (=0.054g/s + 0.1% reading)
IR camera	Sensor accuracy: +-2K or 2% reading	2K or 2% reading
Current	Accuracy: 1% reading	±1% reading

Table 2.3: Uncertainties of measurements

2.2.5 Test matrix

The test matrix was created in order to look at the main parameters that could influence the heat transfer coefficient in a real application such as the cooling of electronics. The main parameters are varied while keeping the rest as constant as possible to have the best comparison possible. The parameters studied and their variations are:

- The effect of the heat flux (5.69 W/cm^2 -> 17.13 W/cm^2)

- The effect of the inlet temperature (changing the pseudo-critical point location inside the channel)

- The effect of the mass flux (444.3 kg/m^{2}s -> 823.6 kg/m^{2}s)

It was decided to keep a constant pressure at all time as a change in the pressure will affect the pseudo-critical point and the evolution of the different parameters such as the density of the fluid or the Prandtl with regard to the temperature with a large effect on the heat transfer as explained in section 1.1.1.

2.2.6 Data validation

Before analysing any data, a data validation is necessary. First of all, as stated in the description of the data analysis, it is possible to show that neglecting the conduction improves the results. According to [46], an asymmetric heating of a plate has its heat transfer coefficient best approached by the Dittus-Boelter correlation with a correction factor between 0.89 and 0.93 depending on the aspect ratio of the channel (5 and 2 respectively). Having an aspect ratio of 3.2 in this case, a middle value of 0.91 is used as expressed in Eq. 2.20 and 2.21 where the Reynolds number and the thermal conductivity are computed using the bulk fluid temperature but the Prandtl number is computed using the average temperature of the wall and the bulk fluid. Moreover an earlier study on supercritical carbon dioxide showed that Dittus-Boelter gives good results away from the critical point [28].

$$Nu = 0.023Re_b^{0.8}Pr_{av}^{0.4} \times 0.91 \tag{2.20}$$

$$h_{conv} = \frac{Nuk_{bulk}}{D_h} \tag{2.21}$$

With those two information a first test is analysed away from the critical point with the following parameters: $T_{inlet} = 40.1°C$, $P_R = 1.04$, $T_{PC} = 33°C$, $G = 567$ kg/m^{2}s, $q'' = 5.69$ W/cm^2. It is important to remember that the heat flux indicated is the heat produced per square centimeter, however due to the perfect insulation assumption, all the heat produced below the side walls and edges also goes to the fluid through the bottom layer. Therefore, in reality the carbon dioxide sees here as heat flux q'' closer to 11 W/cm^2. The results for the heat transfer coefficient are represented in Fig. 2.18. Due to the huge oscillation with the conduction (see large fluctuations on the curve "data analysis with conduction" in Fig. 2.18), the uncertainties were not represented. Moreover, the uncertainties are not needed to show that the data analysis is better without the conduction. The results present few oscillation and are way closer to the value given by the Dittus-Boelter correlation. For those reasons, the conduction inside the Inconel sheet will simply be neglected for the rest of the data analysis.

The next step was to compare the data analysis to the Dittus-Boelter correlation and the comparison is illustrated in Fig. 2.19a. As can be seen, the heat transfer coefficient is well predicted after the 10 first millimeters of the channel. These results clearly show that the data analysed are well predicted by the correlation as expected with the literature. The only location where this is not verified is the inlet of the channel. This is explained by different phenomena, even though it was impossible to quantify their individual effect. The first phenomenon is the development of the flow after it enters the header and goes into the channels. The second one is the imperfection of the insulation provided by the Torlon leading to some heat leakage through the Torlon resulting in a lower surface temperature and higher heat transfer coefficient. Finally, in the header region, no side walls are present and a part of the heat produced below the side walls at the start of the channels can be absorbed by the fluid in the header. The heat is therefore split further reducing the surface temperature. The effects can also be seen at the end of the channel where the plate temperature decreases as depicted in Fig. 2.19b. In the middle of the channel, the temperature of the plate follows a nearly linear increase as could be expected with the low variation of the heat transfer coefficient.

An other hypothesis that was previously made is the constant heat flux along the channel due to the low
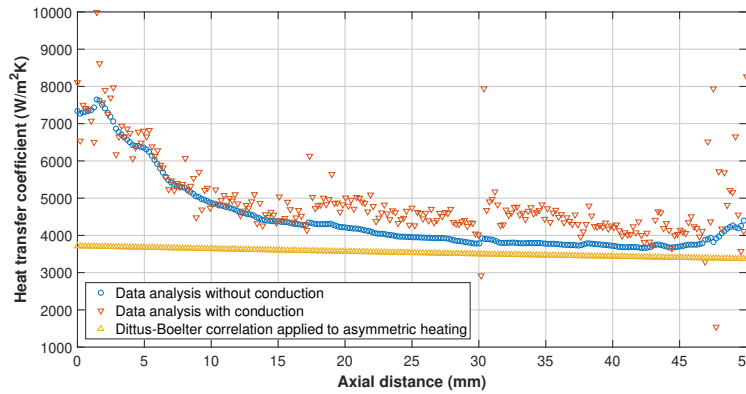
Figure 2.18: Data analysis comparison with or without the conduction

electrical conductivity variation of the Inconel with temperature. Fig. 2.19c clearly shows that the assumption is valid as the highest variation in this case is only 0.3% which is well under the uncertainty.

With the different assumptions verified and the data analysis showing results in line with the literature, it is possible to perform the other tests to see the effect of different factors such as the heat flux, the inlet temperature and the mass flow rate as explained in the test matrix.
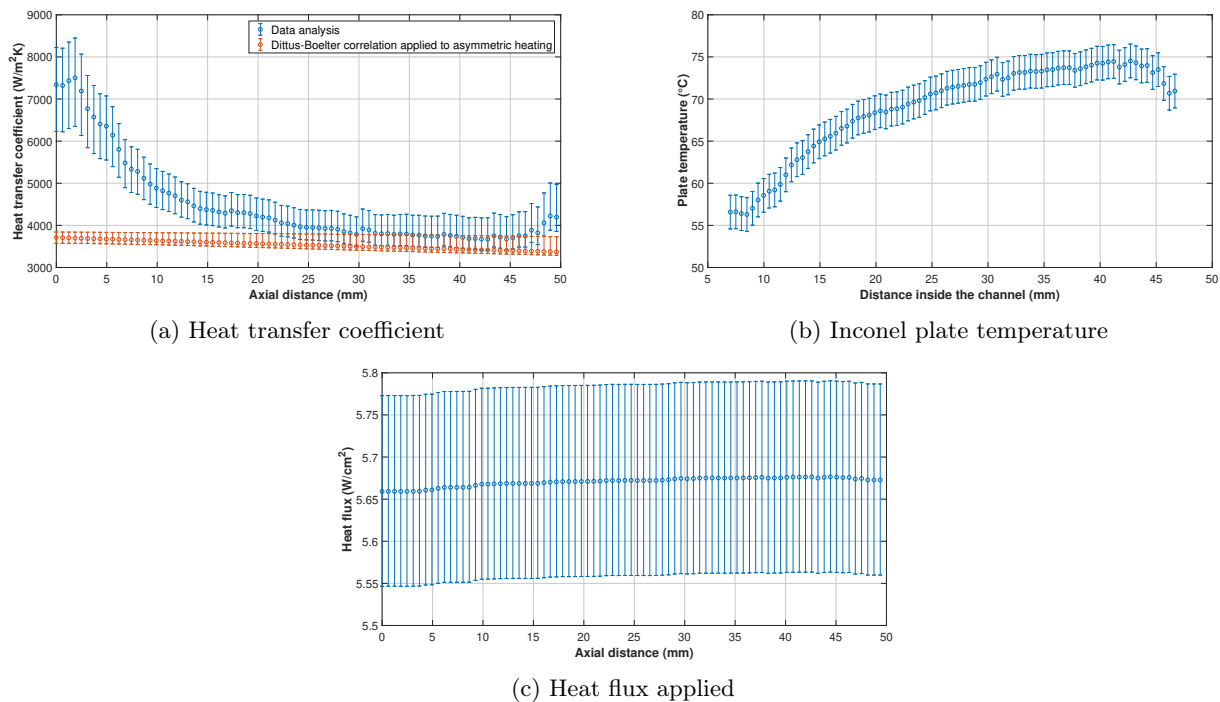
(a) Heat transfer coefficient

(b) Inconel plate temperature

(c) Heat flux applied

Figure 2.19: Data validation away from the critical point ($T_{inlet} = 40.1$°C, $P_R = 1.04$, $G = 567$ kg/m^{2}s, $q'' = 5.69$ W/cm^2)

2.2.7 Response close to the pseudo-critical point

The first step to analyse the heat transfer in the test section was to perform a first test close to the pseudo-critical point to be able to compare the response to the one away from the critical point presented in the previous section. The test is performed with the lowest mass flux used throughout the study (444.3 kg/m^{2}s) and with a relatively high heat flux of 10.55 W/cm^2. The Reynolds number at the inlet is above 11000 meaning that the flow is fully turbulent and this will also be the case for the other tests as the Reynolds will increase with the mass flux

increasing. The Reynolds will even increase along the channel as the density will decrease, which will results in an increasing velocity. This test was chosen in order to see the impact of the buoyancy and the acceleration as their influence is maximum with low mass flux and high heat flux. The different results are presented in Fig. 2.20.

The first result displayed in Fig. 2.20a is the evolution of the heat transfer coefficient along the channel. The coefficient is decreasing from the start of the channel and indicates the presence of the peak in the header region where the pseudo-critical temperature is reached within the turbulent boundary layer. Indeed, it is important to note that due to the homogeneous temperature at the inlet of the test section, the point where the pseudo-critical temperature is reached within the boundary layer is ensured to occur inside the test section, either in the header region or in the channels. The only way to reach it outside of it would be if the inlet temperature was above the pseudo-critical temperature. However, it is important to consider the shape of the curve of the heat transfer coefficient away from the critical point in Fig. 2.19a. There is no doubt that the peak in heat transfer coefficient happens inside the test section but the value of the peak might be lower if the peak was not happening so close to the start of the channel where the heat transfer coefficient is already enhanced by the different reasons presented in the previous section. Apart from the peak, some other points are worth noting. The decrease after the peak is due to the boundary layer turning more and more into a fully 'vapor-like' boundary layer but a small 'rebound' appears after 5mm in the channel. This rebound might be due to the bulk fluid temperature being closer and closer to the pseudo-critical temperature as can be seen in Fig. 2.20b. With that, the resistance between the boundary and the bulk flow decreases and the global heat transfer coefficient increases. After that rebound, the coefficient decreases for the rest of the channel and would decrease more and more until it reaches its stable value when the whole flow is in a 'vapor-like' state and the heat exchange can be described as a single phase turbulent heat exchange as demonstrated in the previous section.

The second figure, Fig. 2.20b shows the evolution of the bulk fluid temperature inside the channel (in blue) with some references such as the inlet and outlet temperatures of the test section measured with thermocouples but also the pseudo-critical temperature computed using the following equation where the pressure is expressed in bar:

$$T_{PC} = -122.6 + 6.124 * P_{sCO2,bar} - 0.1657 * P_{sCO2,bar}^2 + 0.01773 * P_{sCO2,bar}^{2.5} - 0.0005608 * P_{sCO2,bar}^3 \qquad (2.22)$$

Finally, the last element is the outlet temperature computed with the energy balance all along the channel. This point is further along the x-axis than the end of the channel as the header region is 7mm long. As can be seen, the value computed and the value measured by the thermocouple are within uncertainty range further validating the model of analysis. The huge difference in uncertainty between the upper limit and lower limit for the temperature is caused by the properties around the pseudo-critical point. Indeed, the energy balance in the model is using the enthalpy for which the uncertainty is the same for the upper and lower limit. However due to the huge specific heat capacity at the pseudo-critical point, the lower limit going towards the pseudo-critical temperature, sees a much lower uncertainty. On the other end, the upper uncertainty goes away the pseudo-critical point where the specific heat capacity is much lower, a same error in enthalpy therefore leads to a much higher uncertainty error in temperature.

The evolution of the plate temperature is represented in Fig. 2.20c, compared to Fig. 2.19b, the highest temperature reached is around 20°C higher. However, this temperature difference is reached while using a lower mass flux (27.7%) and a much higher heat flux (85%) showing the capability of the carbon dioxide around its pseudo-critical point to cool down high heat flux.

The final results displayed in Fig. 2.20d are the Pethukov and Polyakov's buoyancy criterion and the Jackson's acceleration criterion described in section 1.1.3. First looking at the acceleration with the red curve, it is clear that the value observed are well below the threshold and the acceleration will have a negligible effect in these experiments. As this test used the lowest mass flux used in the study with a relatively high heat flux, it is clear that the threshold will not be reached. This is due to the asymmetric heating as well as the high aspect ratio of the channels (3.2) that reduce the effect of the acceleration [29]. On the other side, according to Petukhov and Polyakov criterion and the research done by [24] on horizontal tube, the heat transfer is here influenced at all time by the buoyancy as the threshold limit is 1. However this effect is relatively low as the maximum value is only 21 compared to the 200 observed in the horizontal tube with supercritcal water. Moreover, a recent study about the impact of the buoyancy in microchannels [29] shows that buoyancy influence is quite low in microchannels. However, the influence of the different parameters will still be studied over the buoyancy influence.

(a) Heat transfer coefficient

(b) Inconel plate temperature

(c) Inconel plate temperature

(d) Buoyancy parameter
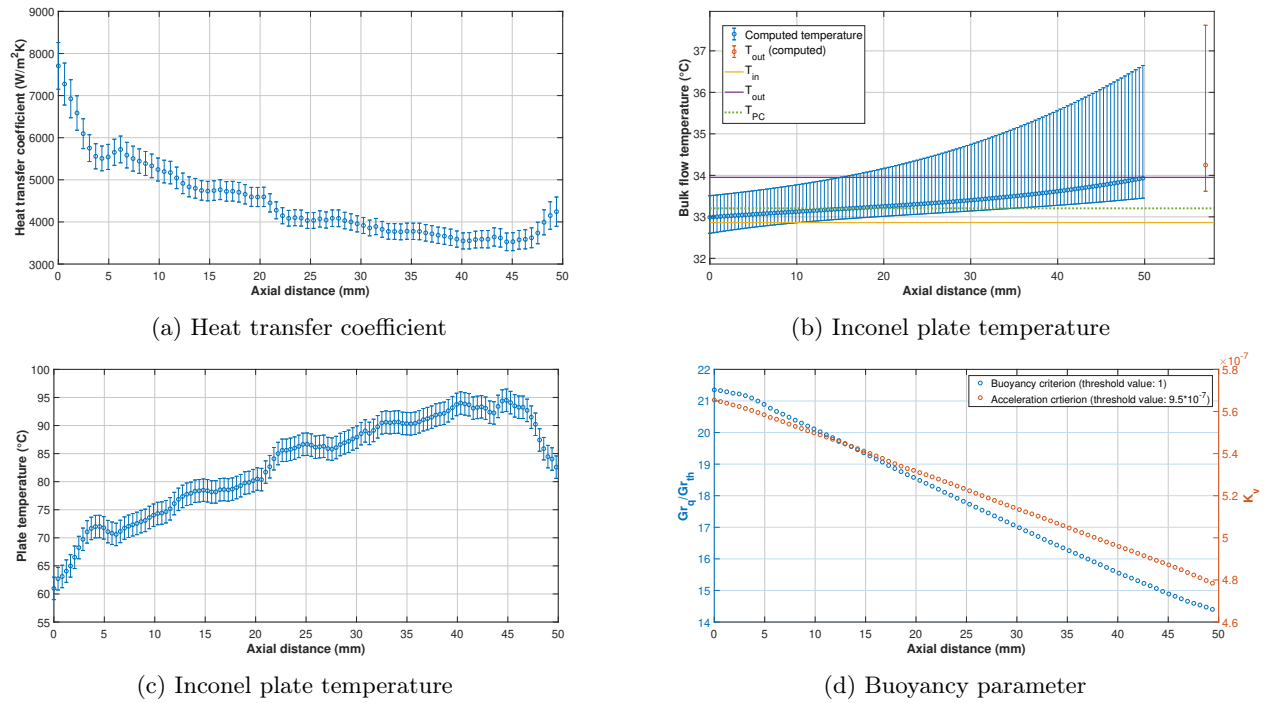
Figure 2.20: First test close to the pseudo-critical point: $T_{inlet} = 32.86°C$, $T_{outlet} = 33.95°C$, $P_R = 1.05$, $T_{PC} = 33.1°C$, $G = 444.83$ kg/m²s, $q'' = 10.55$ W/cm²

2.2.8   Effect of heat flux

The first parameter to be studied is the variation of the heat flux with the mass flux constant at around 480 kg/m²s (+-16 kg/m²s) and the reduced pressure is fixed at $P_R = 1.05$ leading to a critical temperature of 33°C. The exact value of the different parameters for each tests are given in detail in Tab. 2.4.

	T_{inlet} (°C)	T_{outlet} (°C)	G (kg/m²s)	ΔP (kPa)	q'' (W/cm²)
Blue line	31,06	32,62	485,99	3.97	6,88
Red line	31,20	32,79	479,73	4.01	8,74
Yellow line	31,67	32,98	482,07	4.43	10.55
Purple line	31,72	33,12	488,65	4.72	12.80

Table 2.4: Parameters specification for the impact of the heat flux with the pseudo-critical point outside or at the very end of the channel ($P_R = 1.05$, $T_{PC} = 33°C$)

Before looking at the effect of an increased heat flux in Fig. 2.21, it is important to note that only the test with the highest heat flux has a bulk flow temperature above the pseudo-critical temperature at the outlet of the test section. This means that none of the bulk flow will be in a vapor-like condition inside the test section and the pressure drop stays relatively low. Higher pressure drop will occur with a higher inlet temperature leading to a vapor-like bulk fluid inside of the channel.

From the first look at Fig. 2.21a, it is clear that a lower heat flux leads to higher heat transfer coefficient which is in line with the literature. All tests also show the same general shape for the evolution of the heat transfer coefficient with an increase at the start of the channel followed by a decrease to a more or less stable value for most of the remainder of the channel. This shows that the peak of the heat transfer coefficient appears always before the bulk fluid temperature reaches the pseudo-critical point. Looking at the Inconel plate temperature in Fig.2.21b, the temperature is always well above the pseudo-critical point. It explains the shape of the curve with the peak at the start when the pseudo-critical point is reached inside of the boundary layer. Looking at the highest heat flux on the figure, the heat transfer coefficient only decreases from the start. Considering the plate temperature of 70°C at the inlet of the channel, it is safe to assume that the peak occurs in the header region and once in the channels, the boundary layer must be nearly totally in the 'vapor-like' state decreasing the heat transfer coefficient. For

lower heat flux, the temperature gradient between the plate and the fluid is lower at all time leading to better heat transfer coefficient with the highest peak happening with the lowest heat flux with values as high as 10680 W/m²K. Moreover, with the lower heat fluxes, the heat transfer coefficient is still increasing at the start before decreasing to its stable value for the rest of the channel. Over the whole channel, the results show an average decrease of the heat transfer coefficient around 30% when the heat flux is doubled (between the blue and purple line) while the plate temperature is nearly doubled.

(a) Heat transfer coefficient

(b) Inconel plate temperature

(c) Buoyancy parameter
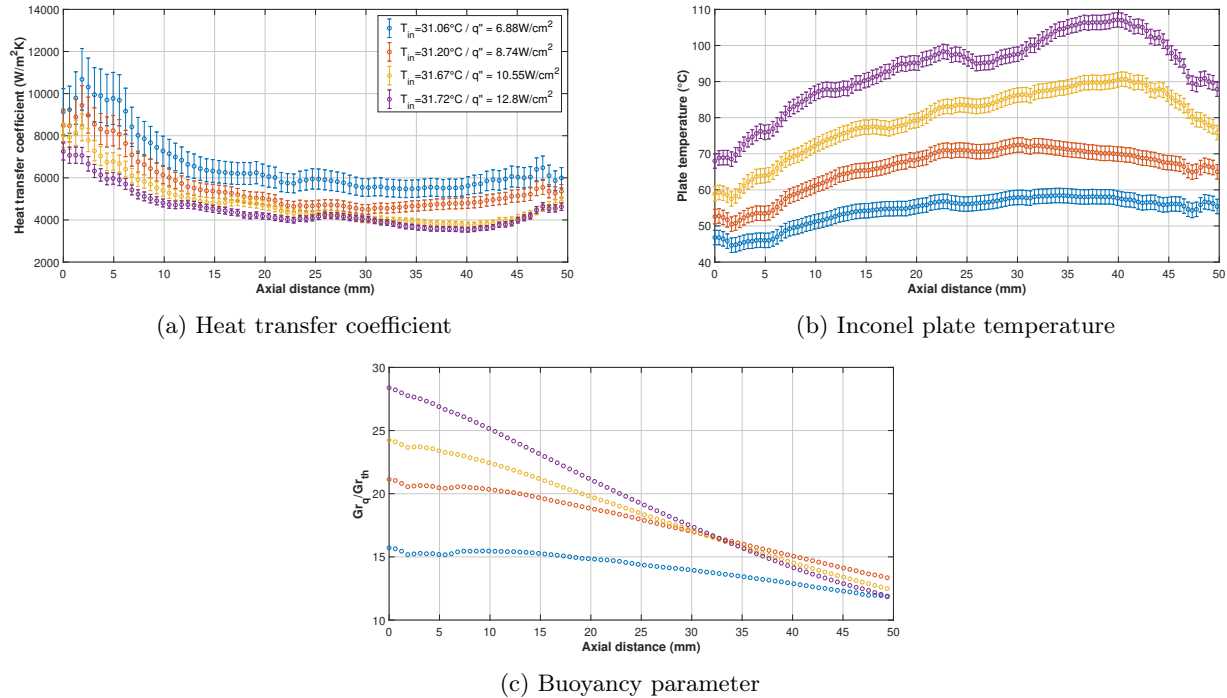
Figure 2.21: Effect of heat flux over the results observed with the pseudo-critical point outside or at the very end of the channel

An other parameter that is interesting to look at is the buoyancy criterion in Fig. 2.21c. As could be expected, the higher the heat flux, the higher the buoyancy parameter as the buoyancy is created by the density gradient through the boundary layer. This also explains why the test with the highest heat flux ends up with the lowest value. Indeed, the bulk fluid temperature reaches the pseudo-critical temperature at the end of the channel and approaches a 'vapor-like' state leading to the decrease of the density gradient and so the effect of the buoyancy.

In conclusion, a lower heat flux will always lead to better performances in the heat transfer with a higher heat transfer coefficient at all time. Moreover, a higher heat flux increases the pressure drop even if this increase is not huge as the pressure drop only increased by around 20% when the heat flux increased by nearly 90% (between the two extreme tests). It means that overall the pressure drop is not proportional to the heat flux. Moreover, this set of tests shows that the peak in heat transfer coefficient appears before the pseudo-critical temperature is reached in the bulk fluid temperature. It appears when the pseudo-critical temperature is reached within the boundary layer which is in line with research done on macro-scale heat exchanger using supercritical carbon dioxide. The effect of buoyancy will be further discussed in the following sections.

2.2.9 Effect of a different inlet temperature

In order to improve the analysis of the effect of the heat flux, a second set of tests was performed using higher inlet temperature (around 1.5°C higher) while keeping the same mass flux, the same pressure (meaning the same pseudo-critical temperature) and the same heat fluxes (see Tab. 2.5. In this case, each test has its bulk flow temperature leaving the channels above the pseudo-critical temperature. A first observation is the increased pressure drop compared to the first set. For the same heat flux, the pressure drop increases by 30 to 40% when the inlet temperature increases. This is explained by the higher pressure drop when the flow is in a 'vapor-like' state while keeping the same mass flux.

	T_{inlet} (°C)	T_{outlet} (°C)	G (kg/m^{2}s)	ΔP (kPa)	q'' (W/cm^2)
Blue line	32,78	33,17 30	493,25	5,50	6,90
Red line	32,80	33,46 17	483,67	5,69	8,74
Yellow line	32,80	33,78 15	480,51	5,73	10.55
Purple line	32,94	34,52 11	494,81	6,36	12.80

Table 2.5: Parameters specification for the impact of the heat flux with the pseudo-critical point reached inside the channel ($P_R = 1.05$, $T_{PC} = 33$°C)

First of all, it is easy to see that an increased heat flux has the same impact in Fig. 2.22 than in the previous section. A higher heat flux means a higher pressure drop and a lower heat transfer coefficient all along the channel. The evolution of the buoyancy parameter displayed in Fig. 2.22c is also the same as in Fig. 2.21c even if the buoyancy impact is smaller in this case. This is due to the bulk fluid temperature being at a higher temperature and therefore having a lower density. However, on the contrary to what could be expected, except for the pressure drop, the evolution of the heat transfer coefficient and the plate temperature in Fig. 2.22 are really close to the ones in Fig. 2.21. Indeed, for a same heat flux, the values at any points are nearly identical. These results can be confusing at first, however, with some further analysis, it is possible to explain them.

The first thing to note is that for the cases of $q'' = 8.74$ W/cm^2 (the red line) and $q'' = 10.55$ W/cm^2, the heat transfer coefficient does not see any increase in the second set and just stays constant for the first couple millimeters before decreasing. In the first set the coefficient increases by around 500 W/m^{2}K and then starts to decrease. This behavior with a constant heat transfer coefficient at the start is the same observed for the highest heat flux in the first set. With the higher inlet temperature and the heat flux of 12.8 W/cm^2, the heat transfer coefficient does not even stay constant at the start and decreases straight away. For the lowest heat flux, the heat transfer coefficient increases in both cases but the increase is larger for the lower inlet temperature. This observation shows that except for the blue curve in Fig. 2.22a, all the higher heat fluxes reached their highest heat transfer coefficient in the header region. The value at the start is as high as for lower inlet temperature as in theory the peak is higher when the heat flux is lower (as demonstrated in the previous section) but also when the bulk fluid temperature is closer to the pseudo-critical temperature as it reduces the resistance between the turbulent boundary layer and the bulk flow. Moreover, the buoyancy parameter is lower with the higher inlet temperature as can be seen in Fig. 2.22c compared to Fig. 2.21c. This is once more explained by the lower density gradient through the boundary layer as the bulk flow is at a higher temperature all along the channel where the plate temperature is mostly equal. However, it is hard to quantify the impact of the buoyancy in this case. The same study should be performed with the upper plate heated instead of the lower one in order to compare the results and see if the buoyancy is just a local effect or if it also affects the global performance of the heat transfer.

The second thing to note is the decrease of the heat transfer coefficient for the blue curve around the 35th mm of the channel in Fig. 2.22a. This decrease occurs slightly after the bulk fluid temperature gets above the pseudo-critical point. The other curves also seem to decrease along the channel with the bulk fluid temperature increasing more and more above the pseudo-critical temperature leading to a decrease of the Prandtl number and the specific heat capacity. This reduction in the heat transfer coefficient is also in line with what was observed in different earlier studies. Thanks to the data validation previously made, it is possible to say that the heat transfer coefficient would continue to degrade until it reaches the value predicted by the Dittus-Boelter correlation for asymmetric heating once the whole flow is in a 'vapor-like' state. In the case of a longer test section, it is expected to have a sharp decrease in the heat transfer coefficient with the bulk flow turning more and more into a fully 'vapor-like' state.

The second set of test to look at the influence of the inlet temperature was performed using a constant heat flux of 12.8 W/cm^2 and mass flux nearly constant, the difference being within the range of the uncertainty. The detailed parameters of the different tests are presented in Tab. 2.6. As the pseudo-critical temperature is 33°C, all tests have their outlet temperature above it but the first one is just reaching it at the very end. This is reflected in the pressure drop which is around 30% lower for the first test compared to the others.

Instead of displaying the results with the axial distance as the abscissa, the set is using the ratio between the bulk fluid temperature and the pseudo-critical temperature in Fig. 2.23. With this new axis, the points are not evenly distributed along the graph anymore. The higher specific heat capacity around the pseudo-critical point means that the closer the pseudo-critical point is, the closer the points are from one another.

(a) Heat transfer coefficient

(b) Inconel plate temperature

(c) Buoyancy parameter
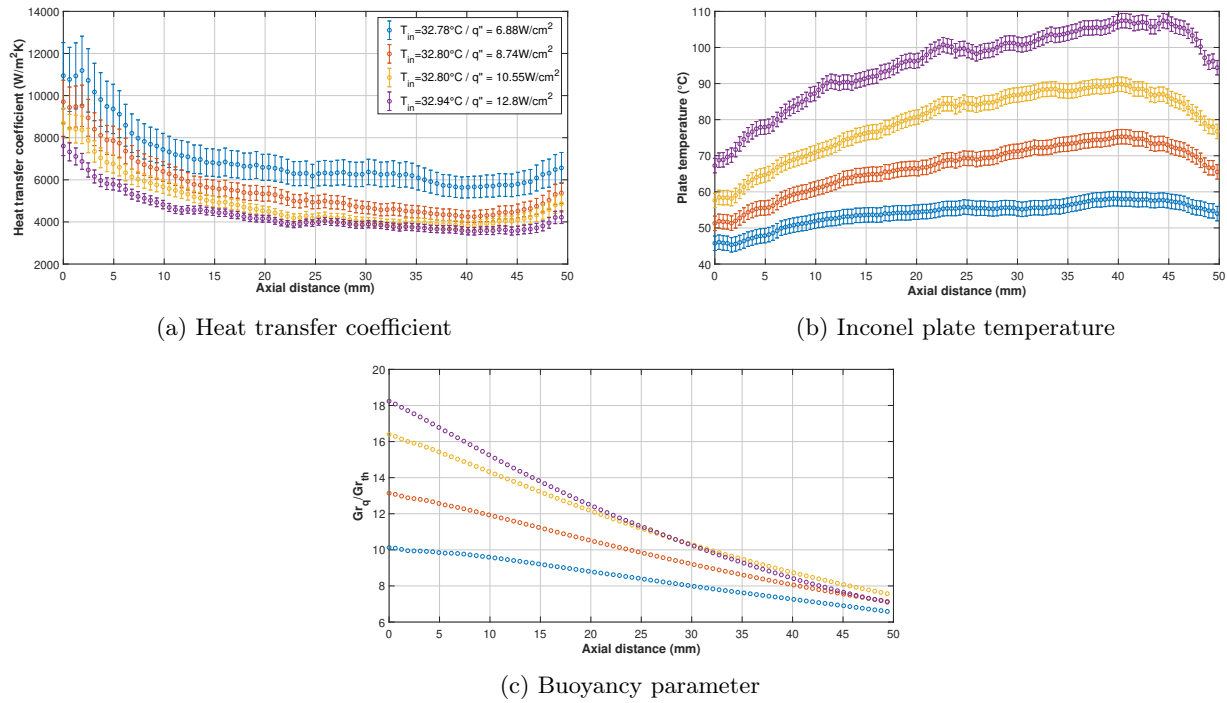
Figure 2.22: Effect of heat flux over the results observed with the pseudo-critical point reached inside the channel

	T_{inlet} (°C)	T_{outlet} (°C)	G (kg/m^{2}s)	ΔP (kPa)	q'' (W/cm^2)
Blue line	31,73	33,12	488,65	4,72	12.80
Red line	32,94	34,52	494,81	6,36	12.80
Yellow line	32,59	33,56	507.15	5,97	12.80

Table 2.6: Parameters specification for the impact of the inlet temperature with a constant heat flux and mass fluxes within uncertainty error ($P_R = 1.05$, $T_{PC} = 33$°C)

Looking at the evolution of the heat transfer coefficient in Fig. 2.23a, it is clear that a higher inlet temperature leads to a higher heat transfer coefficient peak as both the red and yellow curve shows no sign of reaching their maximum compare to the blue curves that is stable at the start. This could however be due only to the inlet impact over the results. Around the pseudo-critical point, a transition seems to occur for the blue and yellow curves as a sudden increase in heat transfer coefficient appears. This might be due to the bulk flow presenting its minimum resistance but this increase is soon followed by a new decrease. In the case of the yellow curve, this increase leads the curve to be really close to the red one until the effects of the outlet appear. Concerning a convergence between the three curves, it is assumed that it would happen in a longer heat exchanger and as stated before, it would ultimately converge to the results given by the Dittus-Boelter correlation once the bulk fluid temperature is away from the pseudo-critical point. An other proof of the convergence is the evolution of the buoyancy in Fig. 2.23c. The three curves nearly overlap around the pseudo-critical temperature and have the same shape. The difference between the three might even come from the small difference in their mass flux. Indeed a higher mass flux leads to a lower buoyancy effect and the blue curve is the one with the lowest mass flux (and so the higher buoyancy effect). The effect of the mass flux over the buoyancy will be further developed in the following section.

Looking at the evolution of the plate temperature in Fig. 2.23b, it is possible to see that for every inlet temperature, the peak in heat transfer coefficient will happen for a different combination of bulk fluid temperature and plate temperature. The higher the inlet temperature, the higher the bulk fluid temperature but the lower the plate temperature. This lower temperature difference between the two is the main factor explaining the higher peak in heat transfer coefficient for higher inlet temperature.

From the different tests performed, it is possible to say that an inlet temperature closer to the pseudo-critical temperature (but always below it) gives a higher peak in heat transfer coefficient. However this higher peak comes

(a) Heat transfer coefficient

(b) Inconel plate temperature

(c) Buoyancy parameter
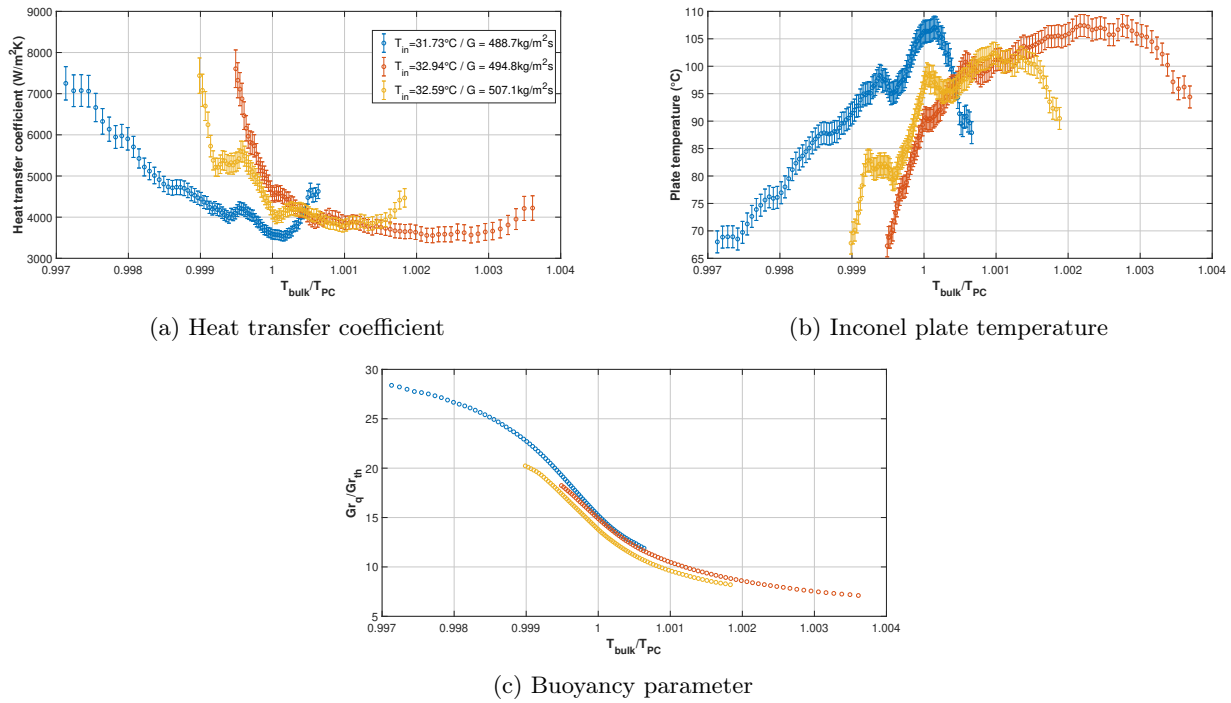
Figure 2.23: Effect of inlet temperature with a fixed heat flux ($q'' = 12.8$ W/cm^2) and pressure ($P_R = 1.05$)

at the cost of a higher pressure drop. Moreover, comparing the plate temperatures between Fig. 2.21b and Fig. 2.22b, for a given heat flux, the inlet temperature has only a small impact. In conclusion, the inlet temperature could be very important in the case of very small surface with really high heat flux where the heat transfer could really be optimized with an inlet temperature really close to the pseudo-critical temperature. This would ensure a lower plate temperature. However, in larger heat exchanger, the pressure drop could difference could be significant and a lower inlet temperature could be preferred.

2.2.10 Effect of mass flux

The next parameter to be studied is the variation of mass flux. In the first set of tests, a more or less constant mass flux was used while increasing the heat flux like in Fig. 2.21 and 2.22. In order to compare the response to one of those two, the color of the different tests remained the same as before. The difference being that the lowest heat flux studied earlier is not tested in this set. It was also possible to study higher heat fluxes without having risks of degrading the Torlon plastic as for a given heat flux, the wall temperature is lower with a higher mass flux. The highest heat flux in this case is thus 17.13 W/cm^2. The different parameters of the tests are presented in Tab. 2.7. As can be seen, the inlet temperature is close to the tests performed in Fig. 2.22 and a comparison between the two will be used to show the effect of a higher mass flux.

	T_{inlet} (°C)	T_{outlet} (°C)	G (kg/m^{2}s)	ΔP (kPa)	q'' (W/cm^2)
Red line	32,77	33,03	740,68	12,05	8,74
Yellow line	32,89	33,29	726,858	12,39	10.55
Purple line	32,85	33,53	733,76	13,13	12.80
Green line	32,89	33,72	744,08	13,92	13.41
Cyan line	32,82	33,67	823,55	16,09	17.13

Table 2.7: Parameters specification for the impact of the heat flux with a higher mass flux ($P_R = 1.05$, $T_{PC} = 33$°C)

Just like in the case of a higher inlet temperature, it is no surprise to see the pressure drop increase with the mass flux. Indeed, the pressure drop in duct is proportional to the square of the mass flux. In this case, the increase is not exactly quadratic as the temperature is also playing a part in the pressure loss as explained in section 2.2.9. However, this increase also comes with a large increase in heat transfer coefficient as shown in Fig. 2.24a. The

peak is much higher and the more or less stable value in the remainder of the channel is also much higher than with lower mass flux. Looking at the plate temperature in Fig. 2.24b, the temperature is much lower leading to smaller temperature gradients inside the boundary layer and improving the heat transfer coefficient. Moreover, those smaller gradients lead to a lower effect of the buoyancy. Looking in Fig. 2.24c, the impact of the buoyancy is nearly negligible in all cases. All those different results are in line with the results observed in macro-scale heat exchangers.

In the case of a real application such as the cooling of electronics, it is fairly obvious that the mass flux will be a really important parameter in order to avoid any overheating of the different devices. It is indeed the easiest way to reduce the plate temperature if the power happens to increase. Compared to the purple curve in Fig. 2.22b, the temperature reached by the cyan curve in Fig. 2.24b is pretty similar with a maximum temperature between 100 and 110°C. Going from one curve to the other represents an increase of 34% in heat flux (from 12.8 to 17.13 W/cm^2) and an increase of 66% in mass flux (from 494.81 to 823.55 kg/m^{2}s). This shows that at high heat flux, the mass flux must increase more than proportionally to the heat flux to keep the same plate temperature.

(a) Heat transfer coefficient

(b) Inconel plate temperature

(c) Buoyancy parameter
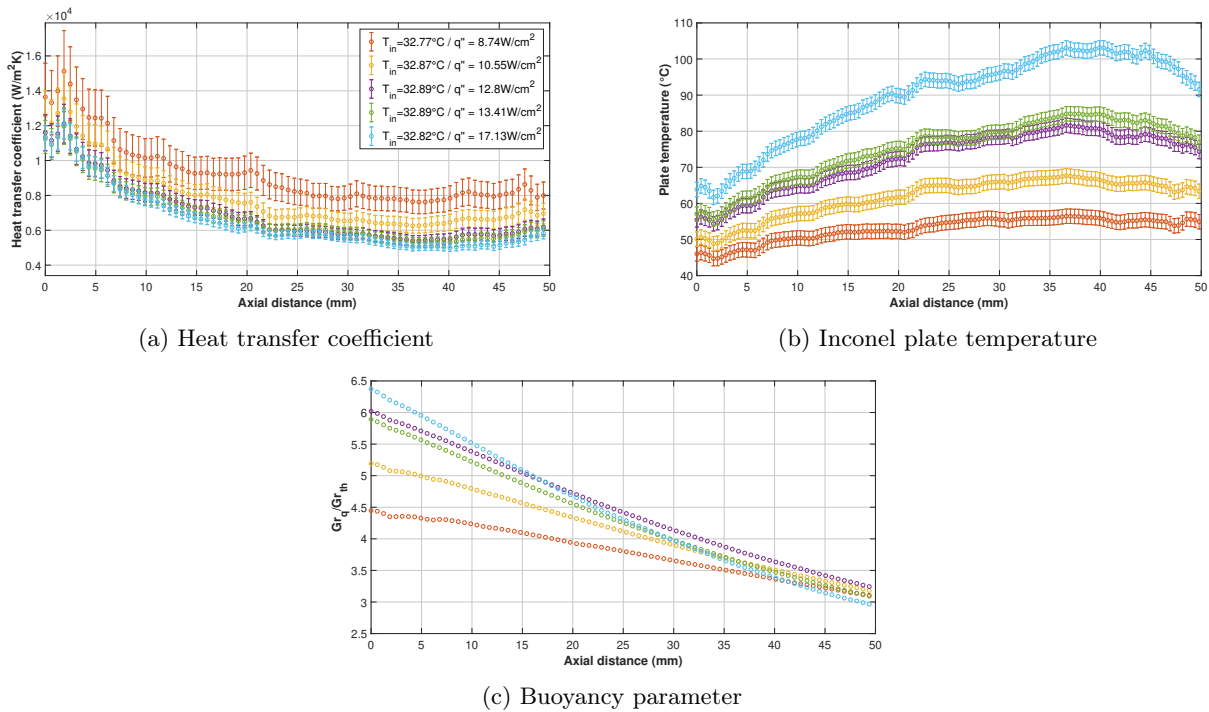
Figure 2.24: Effect of heat flux over the results observed with a higher mass flux

The second set of tests presented are tests using the same heat flux, around the same inlet temperature but with different mass flux to assess the response of the system when the mass flux is increased or decreased at constant heat flux. The different parameters of the tests are exposed in Tab. 2.8.

	T_{inlet} (°C)	T_{outlet} (°C)	G (kg/m^{2}s)	ΔP (kPa)	q'' (W/cm^2)
Blue line	32,94	34,52	494,81	6,36	12.80
Red line	32.85	33.53	733.76	13.13	12.80
Yellow line	32,77	34.15	463.48	5.41	12.80

Table 2.8: Parameters specification for the impact of the mass flux with a constant heat flux and inlet temperature within uncertainty error ($P_R = 1.05$, $T_{PC} = 33$°C)

As just explained, this is no surprise to see the highest pressure drop and the lowest outlet temperature with the highest mass flux. But in order to better understand the other effects of the mass flux, the different results were displayed in Fig. 2.25 using the ratio between the bulk fluid temperature and the pseudo-critical temperature (as it was done with the tests at various inlet temperature).

The first thing to note in Fig. 2.25a is that the red line with the highest mass flux sees a peak where the two

other lines decrease from the start with their peak happening in the header region. It shows that thanks to a lower plate temperature (as can be seen in Fig. 2.25b), the point where the pseudo-critical temperature is reached inside the boundary layer happens later in the channel with a higher bulk fluid temperature. This lower temperature gradient increases the heat transfer coefficient (around 50% higher all along the channel with a 40-50% increase of the mass flux) but also decreases the effect of buoyancy as the density gradient between the fluid at the wall and the bulk flow is much lower than with a lower mass flux.

When comparing with the effect of the inlet temperature, it is possible to note that the evolution of the heat transfer coefficient between the different mass fluxes is more similar than it was with the different inlet temperatures in Fig. 2.23b. Indeed, if the blue curve was translated upward and a little bit to the right, it would fit decently the red curve. The slope of the higher mass flux is just slightly steeper as there is nearly no influence of the buoyancy. However, in this case, there is no similarity in the evolution of the buoyancy effect in Fig. 2.25c. The slope is really different between the three cases because the mass flux influences a lot the buoyancy. Indeed, between the blue and yellow curve, the mass flux decrease by less than 10% and the difference in Fig. 2.25c is already significant for the value of the criterion.

(a) Heat transfer coefficient

(b) Inconel plate temperature

(c) Buoyancy parameter
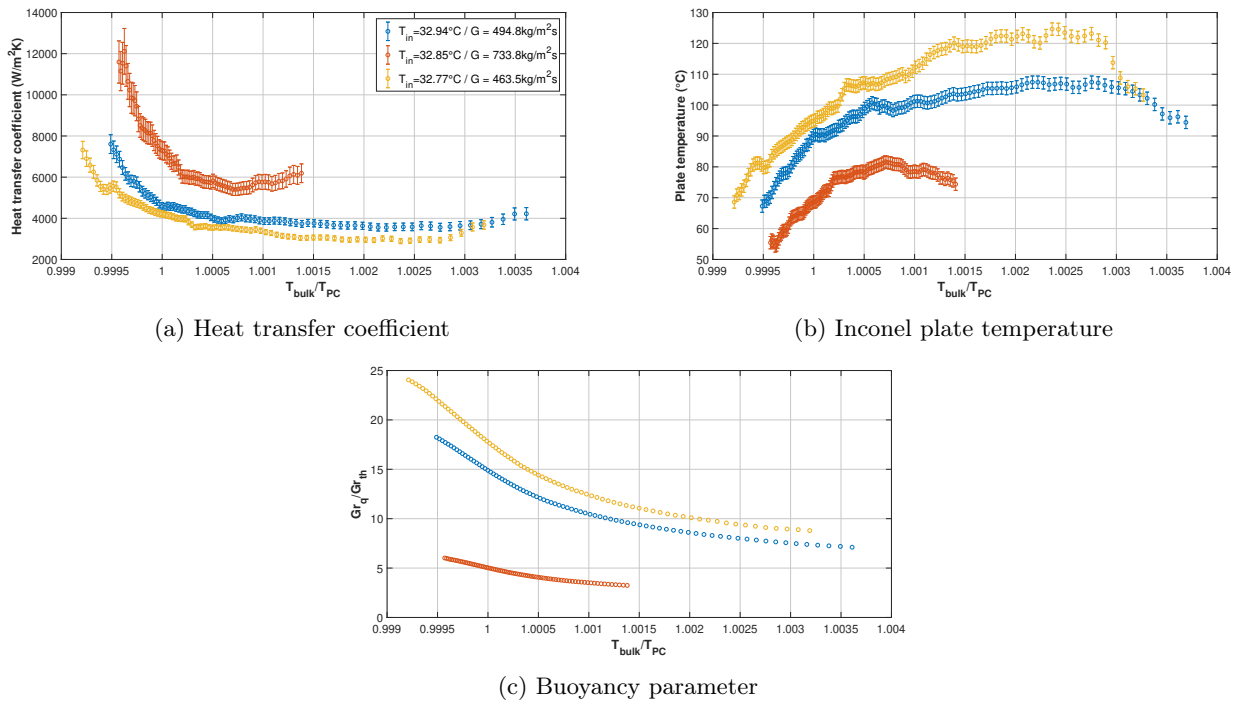
Figure 2.25: Effect mass flux with a fixed heat flux ($q'' = 12.8$ W/cm^2) and pressure ($P_R = 1.05$)

In conclusion, the mass flux increases the heat transfer coefficient and decreases quite significantly the plate temperatures but it comes at the cost of higher pressure drops. With really high heat flux, an increase in mass flux can also significantly reduce the effect of buoyancy but also of the acceleration and avoid a 'laminarization' in an extreme case with higher heat fluxes than what was tested in this study.

2.2.11   Extreme cases

The last set of tests to be exposed is a couple of experiments with the highest heat flux used throughout this study. This heat flux is 17.13 W/cm^2 corresponding to a current of 70Amp. Two different mass fluxes were used in order to compare the results. Those results are displayed in Fig. 2.26 with the red line corresponding to the higher mass flux of 823.6 kg/m^{2}s with an inlet temperature of 32.82°C and the blue line has a mass flux of 630.4 kg/m^{2}s and an inlet temperature of 32.48°C. Once more, the pressure is the same for both tests ($P_R = 1.05$) in order to have the same pseudo-critical temperature of 33°C.

Looking at the different results in Fig. 2.26, the difference between the two curves is exactly the same as what is expected with a mass flux increase. The higher mass flux presents a higher heat flux, with its peak happening

later in the channel, a lower plate temperature and a lower effect of buoyancy and acceleration all along the channel. Concerning the influence of the acceleration, it is proven once more that its influence is negligible for the different tests performed in this study as the maximum value in Fig. 2.26c is well under the threshold value of 9.5×10^{-7}. For the buoyancy, the results show that even with a high heat flux, the buoyancy effect can be significantly reduced to the point of nearly disappearing with a high enough mass flux as displayed by the red curve.

Looking at the plate temperature in Fig. 2.26b, the temperature reaches higher temperature than on previous tests with 130°C reached for the test with the lower mass flux. This is due to the low heat transfer coefficient in the channel caused by a too high temperature gradient through the boundary layer. However it is also important to remember than the heat produced bellow the side walls and edges goes through the bottom layer as the Torlon is an insulator. Therefore the effective heat flux seen by the carbon dioxide in the channel is close to 35 W/cm^2 which is a substantial heat flux.

(a) Heat transfer coefficient

(b) Inconel plate temperature

(c) Buoyancy parameter
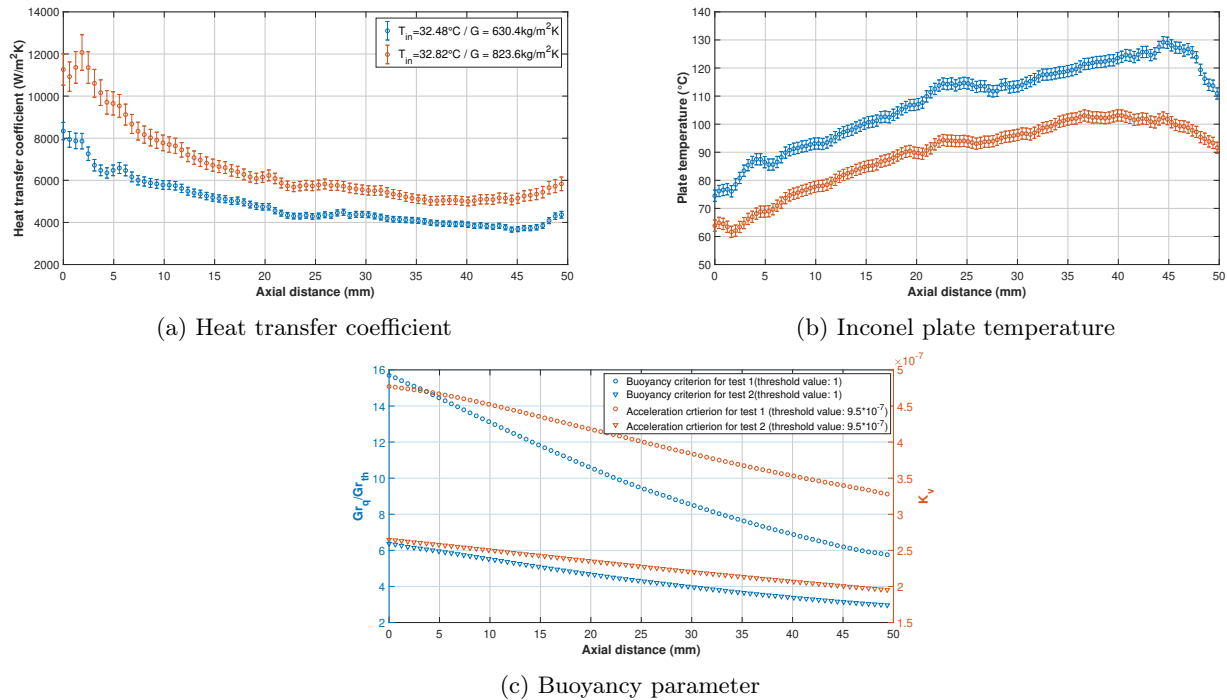
Figure 2.26: Highest heat flux ($q'' = 17.13$ W/cm^2) applied to two different mass fluxes and inlet temperatures ($P_R = 1.05$, $T_{PC} = 33$°C)

In conclusion of this Chapter, the experimental results show that the two parameters having the biggest impact over the heat transfer are the heat flux and the mass flux. An increased heat flux leads to a degradation of the heat transfer coefficient (around 30% when the heat flux is doubled) but also an increase in the plate temperature and the buoyancy parameter. The mass flux has the inverse effect of the heat flux. An increased mass flux leads to better heat transfer coefficients (around 50% better for a 40% increase in mass flux) and lower plate temperature. It also reduce the effects of the buoyancy and the acceleration. Of the three main parameter, the inlet temperature shows the lowest impact over the heat transfer even though the results indicate a possible optimization to reduce the plate temperature. Finally, a test performed at very high heat flux and relatively low mass flux indicates that the acceleration should not affect the heat transfer in normal conditions of electronics cooling. Indeed, the threshold of the acceleration is far from reached with this 'extreme' test. With the effects of the parameters analysed in steady-state condition, it is possible to do some experiments in a transient regime.

Chapter 3

Experimental testing of transient heat transfer

In the case of real life application, the different systems are rarely in steady-state regime. In the case of electronics device, the heat produce will fluctuate in time and the other parameters (mass flux and inlet temperature) will fluctuate as well as part of the control of the cooling system. Therefore, it is important to analyse the response of the system in different transient regimes.

3.1 Change in the setup

Due to the Covid-19 crisis, the actual transformations of the test bench to improve the data acquisition of the transient tests were impossible to carry out so the experimental tests were performed using the same setup as for the steady-state part. This means that the accuracy of the results can be lower and the uncertainty error of the current is increased to account for that (as it is the most impacted as explained just below).

In order to have the best results in a transient regime, it is ideal to collect as much data points as possible during the transient part to capture accurately local effects that can happen due to the transition. Some instabilities could even occur in some cases when the heat flux is rapidly increased due to some local density gradients. Moreover, a larger number of data point in Labview enables to take the mean value to reduce the error due to the oscillation of the acquisition. With that in mind, the goal was to change the acquisition from 2 data points per second to 30 or 60 data points per second (as 60 frames is the maximum possible with the IR camera).

Moreover, in the steady-state case, the current applied to the test section was directly read on the current generator. Indeed, being stable during a whole test and knowing the error on the reading, this method was more than adequate. However, for some tests where the current is to be varied to have a transient heat flux applied to the test section, this method is unreliable as during a transition nothing proves that the current increase is linear between the start and the end of the transition. For that reason, the current generator needs to be linked to the data acquisition using an Ethernet cable in order to know the current at the same time as the rest of the data.

Besides those two modifications, the different components are the same for the transient experiments as in the steady-state experiments. Therefore, the different procedures described in section 2.2.1 such as the pressure drop tests (static and dynamic), the filling of the loop with carbon dioxide and the pressurization to reach the supercritical state and the calibration of the camera do not change from the steady-state tests.

3.2 Experimental results

3.2.1 Procedure

As previously explained, the different procedures such as the pressure tests (static and dynamic) and the filling of the system with carbon dioxide remain the same as for steady-state experiments. The calibration of the camera

stays the same as well. Indeed, the camera was calibrated regarding the focal distance between the lens and the surface to analyse and the temperature range that is observed and neither change from a steady-state test to a transient one. However, a couple of procedures change for the transient part. An example is the analysis of the IR camera images but also the procedure to acquire data.

3.2.1.1 Analysis of the IR camera image

Concerning the analysis of the camera image, a few adaptations had to be made. In order to keep the experiments safe, the currents used throughout the transient experiments is smaller than in the steady-state tests. Indeed, in the steady-state case, it is easy to increase slowly the current and to check all the measures from the different sensors in real time and to adjust the mass flux or the heat flux if the temperature in the test section started to increase too much. In a transient regime where the current is increased by 10 Amp (eg. from 55 to 65 Amp), the temperature could potentially increase rapidly and the Torlon could potentially melt resulting in the degradation of the test section. Therefore, the current was limited to a maximum value of 35 Amp during the different transient tests. A lower heat flux leads to lower surface temperatures and smaller temperature gradients with the rest of the IR image as depicted in Fig. 3.1. This is even more true for the lowest current used (25Amp) and close to the inlet.
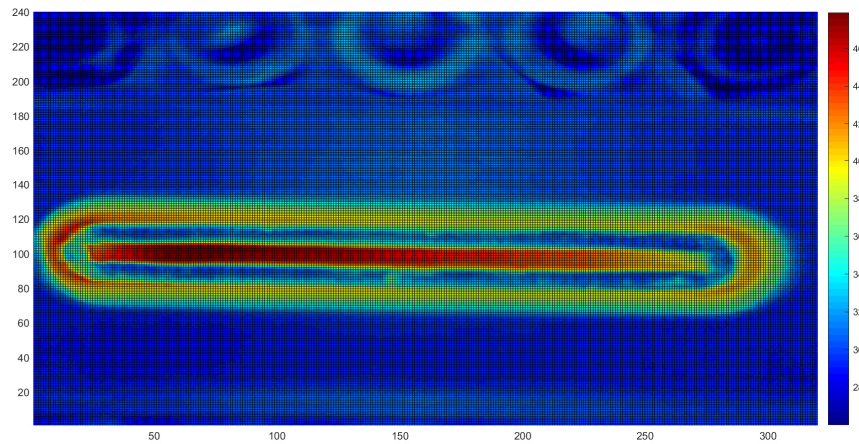
Figure 3.1: Global view of an IR image of the transient analysis

This lower temperature gradient results in some problems for the determination of the limits of the channel close to the inlet. Therefore, the limits are set manually by looking directly on the image to be as precise as possible as depicted in Fig. 3.2. This procedure was done twice to be as precise as possible as the different transient tests were done at two different times and the camera had been moved slightly in the meantime.

Apart from the choice of the pixels delimiting the channel, the equations used to compute the heat transfer coefficient at each frame stay the same. Indeed, with the inlet temperature, the surface temperatures and the current (ie. the heat flux) always known, no differential equations are needed. The same assumptions are also made: the surface temperature measured by the camera is assumed to be the same as at the bottom of the channel and the conduction inside the Inconel is neglected. Therefore all the equations described in section 2.2.3 remain the same and the general equation used to determine the heat transfer coefficient is as follows:

$$h = \frac{E_{gen} - q_{rad}}{dx.dy(T_m - \bar{T}_{sCO2})} = \frac{I^2\gamma}{dx^2 \, Th_f \, (T_m - \bar{T}_{sCO2})} + \frac{4}{3}E_{gen,sw} - \frac{\epsilon\sigma(T_m^4 - T_\infty^4)}{(T_m - \bar{T}_{sCO2})} \qquad (3.1)$$

3.2.1.2 Data acquisition

In an ideal case, the data acquisition for transient experiments is made similarly to steady state. If the objective is to have a data point every second, the data acquisition is set to have more points such as one point every 0.1 second. The mean value of the ten point is then used for the actual data point to reduce the oscillation. In order to avoid the flattening of the peaks, the mean value can be taken over less points in the critical regions.
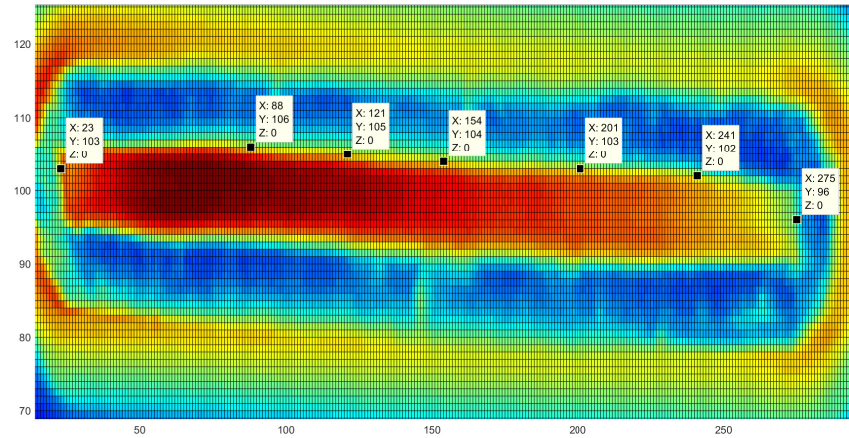
Figure 3.2: Selection of the boundary of the channel in the IR image of the transient analysis

However, in this case, as explained in section 3.1, this was impossible to achieve due to the limitation of time with the Covid-19. The fact that the current generator is not linked to the data acquisition is a problem. Therefore a procedure to keep the experimental results as good as possible is followed:

1. The starting point of the transient test is recorded with 5 IR images and 10 minutes of data to have the starting reference

2. The data acquisition in LabView is activated with a frequency of 2 Hz.

3. The IR camera (set to 2 frames per second as the data acquisition) is activated

4. After a few second the transient part is launched (heat flux increased/decreased, mass flux increased) in a few second (between 3 and 5s)

5. After 10-15s of recording (20-30IR images), the camera is stopped

6. The data acquisition with LabView is stopped after around minute to see if the steady-state is reached or not (with inlet/outlet temperature, pressure drop,...)

7. The new steady-state point is recorded

This method, even if not perfect, enables to have the starting point and the point of convergence and to see the speed of convergence of the system.

3.2.2 Uncertainty analysis

As the test setup does not change, the uncertainty analysis stays the same and the different values are in Tab. 3.1. The only difference is the increase of the error on the current. As the current is not acquired directly in LabView in real time but read on the current generator (as the modifications of the setup were not carried out), the error is assumed 2 times bigger than before. This factor is taken arbitrarily as it is impossible to determine the exact error made over the assumption of the linear variation of the current in time between the value at the start and at the end.

3.2.3 Test matrix

Due to the limitation of time to do the experiments, only a handful of transient tests were conducted. The choice was therefore made to look at three different situations and to compare the results. These situations are:

- The heat flux is doubled from 2.19 W/cm^2 (25.2Amp) to 4.37 W/cm^2 (35.6Amp) in 5s with a constant mass flux of 411.61 kg/m^{2}s

Sensors	Uncertainties	Total uncertainty
Thermocouples	Special uncertainty	±0.5K
Gauge pressure sensor	Sensor accuracy: 0.25% FS Conversion error: 1% reading	0.25% FS + 1% reading
Absolute pressure sensor (Pin)	Absolute uncertainty	±20 kPa
Pressure difference	Absolute uncertainty	±0.12 kPa
Mass flow rate	Sensor accuracy: 0.1% reading DAQ accuracy 0.06%FS	0.06%FS + 0.1% reading (=0.054g/s + 0.1% reading)
IR camera	Sensor accuracy: +-2K or 2% reading	2K or 2% reading
Current	Accuracy: 1% reading Transient error: error x2	±1% reading ±3% reading

Table 3.1: Uncertainties of measurements

- The heat flux id divided by two from 4.3 6W/cm^2 (35.6Amp) to 2.18 W/cm^2 (25.2Amp) in 5s with a constant mass flux of 414.13 kg/m^{2}s

- The mass flux is increased from 490.29 kg/m^{2}s to 578.7 kg/m^{2}s in 5s with a fixed heat flux of 4.36 W/cm^2

Those tests enable the comparison between an increase and a decrease in heat flux. The system could indeed be more reactive in one way due to some local effects. Then the variation of the mass flux is used to see the reactivity of the system to get the temperature of the surface down. Indeed in a real application such as the cooling of electronics, the control of the mass flux will be one of the main parameters and knowing how fast the system can respond is really important.

3.2.4 Transient heat flux

In this section, the response of the system to a change of the heat flux is studied. However, before looking a transient test, a small analysis of the two steady-state points is made. The first one is the steady state with the lower heat flux that will be the starting point for the increase and the point of convergence for the decrease in heat flow. The different parameters of the steady-state are detailed in Tab. 3.2.

T_{inlet} (°C)	T_{outlet} (°C)	G (kg/m^{2}s)	ΔP (kPa)	q'' (W/cm^2)
32.6	32,68	416.46	3.89	2.19

Table 3.2: Parameters specification for the start of the transient test with the increase in heat flux ($P_R = 1.046$, $T_{PC} = 32.9$°C)

As expected with such a small heat flux and the bulk fluid close to the pseudo-critical point, the outlet temperature is really close to the inlet temperature. The pressure drop is also small as the mass flux is not high and the heat flux is not sufficient to increase it significantly. The results of the analysis are shown in Fig. 3.3. Looking at the heat transfer coefficient in Fig. 3.3a, the effect of the inlet of the channels is once more noticeable but apart from that the value stays more or less constant along the channel with a value around 11 kW/m^{2}K. This result comes from the nearly constant fluid temperature along the channel relatively close to the pseudo-critical temperature to assure good thermal properties. Moreover the plate temperature, represented in Fig. 3.3b, is low (once more due to the low heat flux) leading to a small temperature gradient across the boundary layer. Therefore the density gradient is small as well and the buoyancy is not important. This is further shown in Fig. 3.3c where the value of the buoyancy parameter is only around 4. The acceleration parameter is far from the threshold and does not affect the heat exchange. With all that combined, and the fact that the pseudo-critical temperature is reached within the boundary layer, the heat exchanger is in an ideal state to have this really high heat transfer coefficient of 11 kW/m^{2}K.

An other thing to notice is the high uncertainty on the heat transfer coefficient. This is partly due to the higher uncertainty on the current but the main part of the uncertainty comes from the IR camera. Indeed, with its uncertainty of 2°C, the error becomes more significant with a low plate temperature. Indeed an error of 2°C for a temperature of 36°C represents an error of more than 5% where the same error for a temperature of 100°C is only a 2% error. The low temperature is also the cause of the quite large variation of the heat transfer coefficient along

the channel. Indeed, due to the form of the equation used to compute the heat transfer coefficient (in Eq. 3.1) and with the low values all along the channel, a small variation (eg. 0.5°C) in the surface temperature T_w results in a large difference for the heat transfer coefficient.

(a) Heat transfer coefficient

(b) Inconel plate temperature

(c) Buoyancy and acceleration parameters
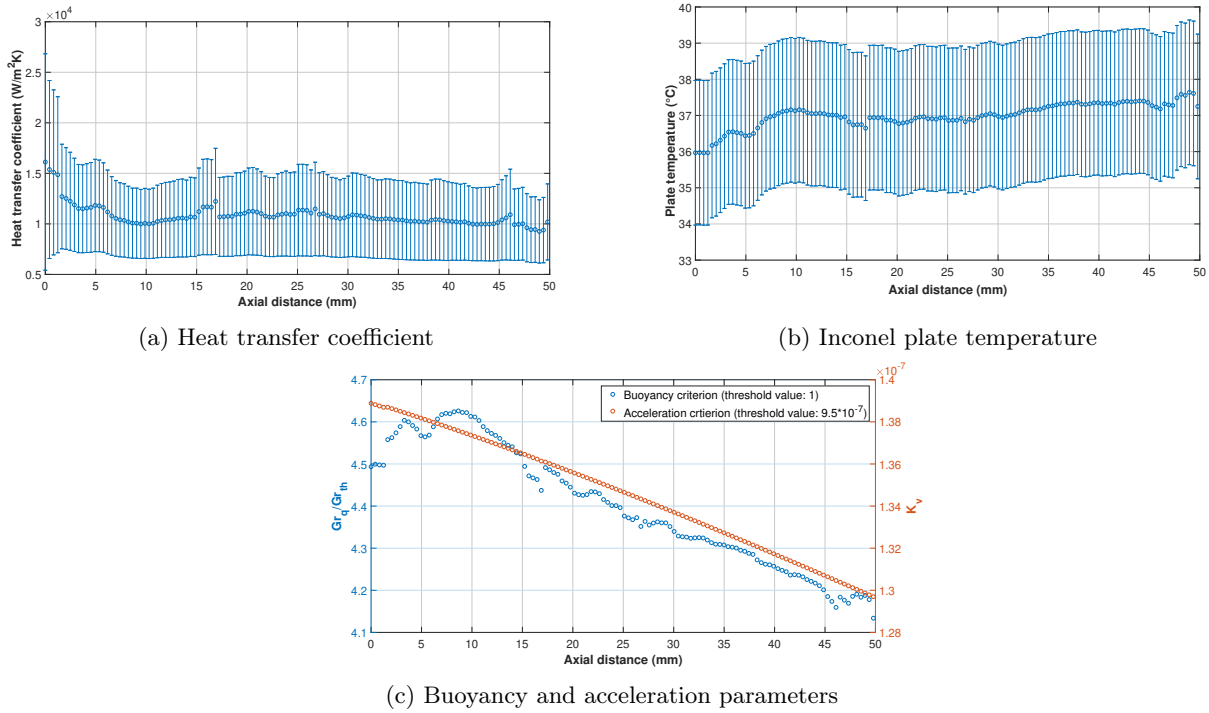
Figure 3.3: Steady state with an heat flux $q'' = 2.19$ W/cm^2 and a mass flux $G = 416.46$ kg/m^{2}s

The second steady state point is the steady state point at the highest heat flux. This point is the point of convergence for the increase in heat flux and the starting point for the decrease in heat flux. The different parameters of the test are presented in Tab. 3.3.

T_{inlet} (°C)	T_{outlet} (°C)	G (kg/m^{2}s)	ΔP (kPa)	q'' (W/cm^2)
33	33.3	408.52	4.02	4.37

Table 3.3: Parameters specification for the convergence point of the transient test with the increase in heat flux ($P_R = 1.051$, $T_{PC} = 33.26$°C)

Obviously, the mass flux is the same as for the test with the lower heat flux. The inlet temperature is sightly higher due to the increased heat flux inside the test section while the heat flux in the pre-heater is kept constant. Therefore, with an increase in the total heat produced, the temperature inside the loop is slightly higher. This also explains the change in pressure (and therefore the pseudo-critical temperature) that increases with the temperature in the loop. An other effect that was expected is the bigger temperature gradient between the inlet and outlet. This leads to a small increase in the pressure drop.

The results for this test are presented in Fig. 3.4. All the results are in line with what could be expected from the analysis of the effect of the heat flux in section 2.2.8. The heat transfer coefficient is lower in Fig. 3.4a than in Fig. 3.3a as it decreases when the heat flux increases. The plate temperature (displayed in Fig. 3.4b) is higher all along the channel and the temperature is also evolving along the channel unlike the temperature in Fig. 3.3b. Finally, the buoyancy is more present in this case as depicted in Fig. 3.4c. The acceleration parameter is also higher but it remains well under the threshold.

Apart from these results, it is also possible to notice that the uncertainty is already much smaller in this case than with the lower heat flux. The temperature of the plate being higher, a small variation in its value has a lesser impact on the heat transfer coefficient as the temperature gradient with the fluid is larger.

(a) Heat transfer coefficient

(b) Inconel plate temperature

(c) Buoyancy and acceleration parameters
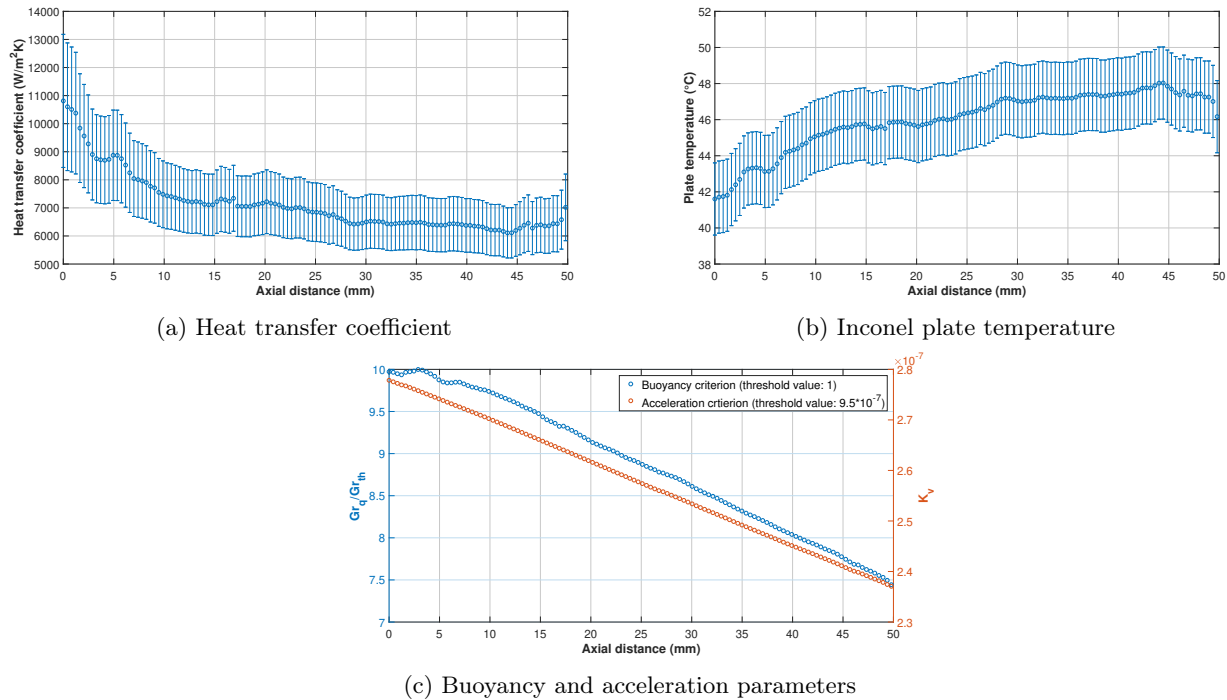
Figure 3.4: Steady state with an heat flux $q'' = 4.37$ W/cm^2 and a mass flux $G = 408.52$ kg/m^{2}s

3.2.4.1 Increase in the heat flux

With the two 'extreme' points for the transient heat flux tests described, it is possible to look at the parameters of the first test in Tab. 3.4. This test looks at the response of the system being subject to a heat flux increase from 2.19 to 4.37 W/cm^2 over a period of 5s. The transient part starts after 3.5s. Before that time the system is still at the steady-state described in Fig. 3.3. The mass flux is assumed constant and the mean value over the transient part is used, the same is done with the pressure which explains the small difference with the starting steady-state point.

$T_{inlet,start}$ (°C)	$T_{outlet,start}$ (°C)	G (kg/m^{2}s)	q''_{start} (W/cm^2)	q''_{end} (W/cm^2)	t_{start} (s)
32.6	32,68	411.61	2.19	4.37	3.5

Table 3.4: Parameters specification for the start of the transient test with the increase in heat flux ($P_R = 1.047$, $T_{PC} = 33$°C)

The results are represented in Fig. 3.5 under the form of the evolution in time of the mean value of the different parameters along the channel. The heat flux is transient after 3.5s and during 5s and is then let constant to see if a stabilisation occurs. This is easy to notice the start and finish of the transient heat flux in Fig. 3.5c representing the evolution of the buoyancy parameter. The evolution seems to be linear during the increase of the heat flux because the current was assumed to increase linearly (as it is not acquired directly with the data acquisition). Therefore in reality, the evolution might not be in such a straight line but the evolution of the buoyancy parameter follows the evolution of the heat flux.

Fig. 3.5a represents the mean value of the heat transfer coefficient along the channel as a function of time. As it is the mean value over the whole channel, those numbers are higher than what they would be if the inlet was not enhancing the heat transfer and therefore increasing the heat transfer coefficient. At the start of the increase in heat flux, the heat transfer coefficient sees a sudden increase and it stabilises for a couple of seconds before decreasing. This increase at the start is due to the thermal inertia of the system. Indeed, the Inconel plate temperature increase sees a small delay compared to the heat flux. Therefore, with the heat flux increasing and the wall remaining at the same temperature (or increasing less than accordingly), the heat transfer coefficient increases. After the first few seconds, the wall temperature increases and the heat transfer coefficient starts to decrease and to converge to its new steady-state point. The decrease is even faster following the end of the increase of the heat flux. It finally starts

to stabilise slowly towards the end. However, looking at the end of the curve and the results for the steady-state point for $q'' = 4.37$, it is clear that the convergence is not yet reached.

The fact that the convergence is not yet reached is also shown in the evolution of the mean temperature of the Inconel plate in Fig. 3.5b. Indeed the temperature is still rising at the end. In this figure, it is also possible to confirm the explanation of the increase of the heat transfer coefficient. Between second 3.5 and 5, the temperature is increasing slowly but increases faster and faster with time. Once the heat flux is at its maximum (at 8s), the temperature increase starts to slow down.
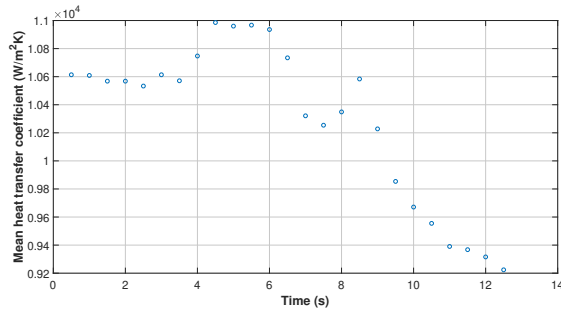
(a) Mean heat transfer coefficient along the channel
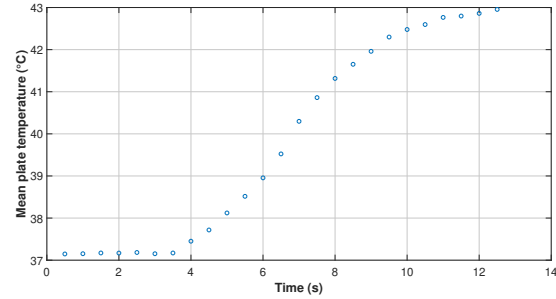
(b) Mean Inconel plate temperature
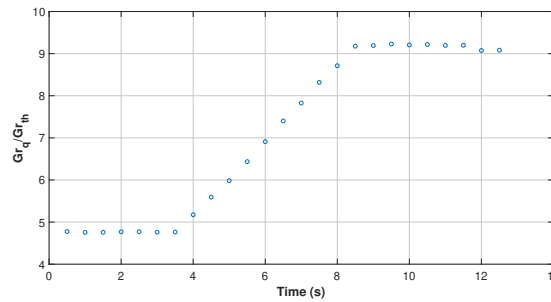
(c) Mean of the buoyancy parameter

Figure 3.5: Evolution in time of the mean value of different results along the channel during an increase of the heat flux from 2.19 to 4.37 W/cm^2 with a mass flux of 411.61 kg/m^{2}s

An other way to see if the convergence is close or not is to look at the heat transfer coefficient along the channel or at the surface temperature at different times. Fig. 3.6 shows results at five different times, the first one is the starting point at the steady state with the heat flux of 2.19 W/cm^2. Then three transient times are displayed, the results after 5s (during the heat flux increase) when the heat transfer coefficient is at its peak, after 10s and after 12.5s as it is the last IR image. Finally, the last line correspond to the new steady-state point with the heat flux of 4.37 W/cm^2.

The heat transfer coefficients, displayed in Fig. 3.6a, show a similar shape for the different time with a small increase at $t = 5s$ and then a decrease toward the new steady-state point. As can be seen, the system is far from convergence after 12.5s. Moreover, the results seem to show some local phenomena as the heat transfer coefficient shows some peak all along the channel that correspond to some colder spot on the Inconel plate as shown in Fig. 3.6b. Those colder spots seem to stay as time passes and even amplify with larger drop in temperature at some places. The fact that those points remain in time is a good indication that some local phenomena are happening and that it is not due to some uncertainty error.

Concerning the evolution of the plate temperature, it is also possible to see here a slow increase at the start which explains the increase in heat transfer coefficient. After 10s, the increase slows down as well with the heat flux being constant and it starts to converge to the new stable point.

Following the analysis of Fig. 3.6 showing that the convergence is not reached, the data from Labview over a longer period of time is looked at. Fig. 3.7 displays the evolution of the inlet and outlet temperature of the carbon dioxide measured by the two thermocouples during the transient test. Due to the procedure followed, the LabView data acquisition starts a couple second before the acquisition of images by the IR camera. This explains

(a) Heat transfer coefficient

(b) Inconel plate temperature

Figure 3.6: Evolution in time of different results along the channel during an increase of the heat flux from 2.19 to 4.37 W/cm^2 with a mass flux of 411.61 kg/m^2s

why the the outlet temperature starts increasing after 5-6s instead of 3.5s as in the IR images analysis. This is obviously taken into consideration in the analysis. After a steep increase of the outlet temperature during around 5s when the heat flux is increased, the outlet temperature continues to rise and sees no real sign of convergence even after a minute. The inlet temperature is also rising as soon as the heat flux increases but slower than the outlet temperature at first as the temperature gradient along the channel increases with the heat flux increasing. But after the initial steep increase of the outlet temperature, the temperature difference between the two stays constant for the rest of the data points. Both temperatures increase as the whole loop tends to its new steady-state point. From the study of the new steady-state point in Fig. 3.4, it is known that the inlet temperature is converging to 33°C and the outlet to 33.3°C. If the evolution was to keep the same slope, the convergence would take at least one additional minute, but the slope is more than probably decreasing as the temperatures draw closer to their stable values and the convergence is most certainly longer than two minutes in total. This is due to all the parameters such as pressure, mass flux, temperatures,... varying with the heat flux and converging to the new stable point for the whole loop.

Figure 3.7: Evolution of the measured inlet and outlet temperatures of the carbon dioxide during an increase in heat flux

3.2.4.2 Decrease in the heat flux

After testing an increase of heat flux, the opposite case is tested. The starting parameters of the test are presented in Tab. 3.5. This test looks at the response of the system being subject to a decrease of heat flux from 4.37 to 2.19 W/cm^2 over a period of 5s. The transient part starts after 2s. Before that time the system is still at the steady-state described in Fig. 3.4. The mass flux is assumed constant and the mean value over the transient part is used, the same is done with the pressure which explains the small difference with the starting steady-state point.

The results are shown in Fig. 3.8. Fig. 3.8c, representing the evolution of the buoyancy parameter, clearly shows the time where the heat flux is evolving, between 2 and 6.5s, and decreases linearly with the heat flux. After that time, the parameter remains nearly constant.

| $T_{inlet,start}$ (°C)	$T_{outlet,start}$ (°C)	G (kg/m^{2}s)	q''_{start} (W/cm^2)	q''_{end} (W/cm^2)	t_{start} (s)
33	33.3	414.13	4.37	2.18	2

Table 3.5: Parameters specification for the start of the transient test with the decrease in heat flux ($P_R = 1.051$, $T_{PC} = 33.26$°C)

Looking at the evolution of the heat transfer coefficient in Fig. 3.8a, the inertia of the systems appears once more. However the magnitude of the decrease is leading to the questioning of the validity of this data point. Indeed the heat transfer coefficient only starts to increase once the heat flux has stabilised and before that decrease by nearly 20%. Moreover, this drop could not be explained by the plate temperature exposed in Fig. 3.8b as it decreases fairly rapidly when the heat flux goes down. Therefore the results shown in this graph should not be taken as the full reality. Due to the adaptation of the data acquisition made to get transient data over the steady-state loop, an error can appear at too much different steps. More testing would be needed to determine if this trend repeats itself or if it just a result of an error during the data acquisition.
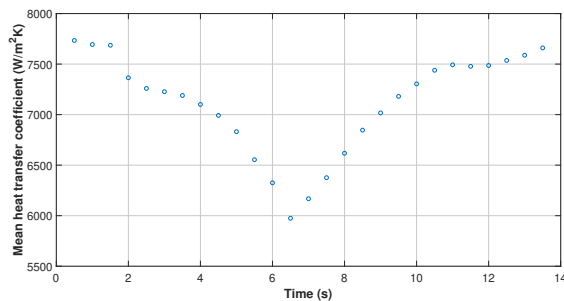
(a) Mean heat transfer coefficient along the channel
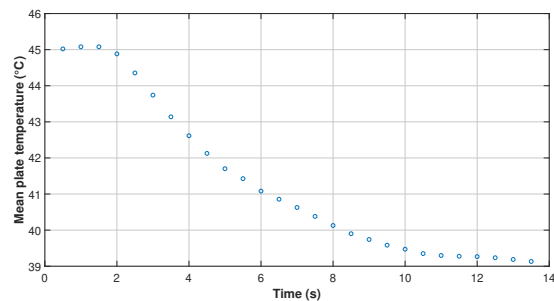
(b) Mean Inconel plate temperature
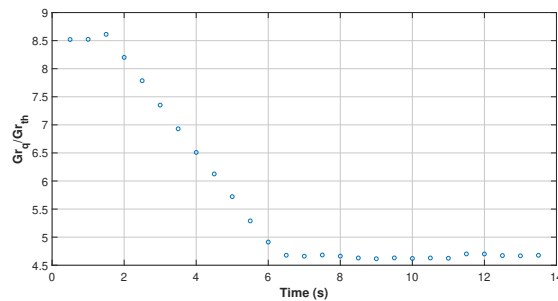
(c) Mean of the buoyancy parameter

Figure 3.8: Evolution in time of the mean value of different results along the channel during a decrease of the heat flux from 4.37 to 2.19 W/cm^2 with a mass flux of 414.13 kg/m^{2}s

In order to look differently at the results, the results of the heat transfer coefficient and the plate temperature along the channel are represented for five different times in Fig. 3.9. The times used are the same except for the fourth one at 13.5s instead of 12.5s as two additional IR images were recorded for this tests.

Looking at the heat transfer coefficient in Fig 3.9a, the evolution is very slow with a convergence to the new steady-state point very far off. However, it seems to increase towards the end of the data recording showing at last an expected result of a possible convergence. Moreover, just like during the increase, some local effects appear with some big variation along the channel. Once more, those variation are corresponding to some hotter spots. And those points are staying hotter during the following seconds. A longer analysis would be needed in order to see how long the local phenomena are present. Moreover, additional testing should be performed to see if those effects are repetitive and analyse their amplitude for different set of heat fluxes.

Fig. 3.9b shows the evolution of the plate temperature, and the results are really similar to those of the increase in heat flux in Fig. 3.6b. The plate temperature decreases rapidly with the presence of some hotter spots and then the decrease slows down until it reaches eventually the new steady-state point.

(a) Heat transfer coefficient
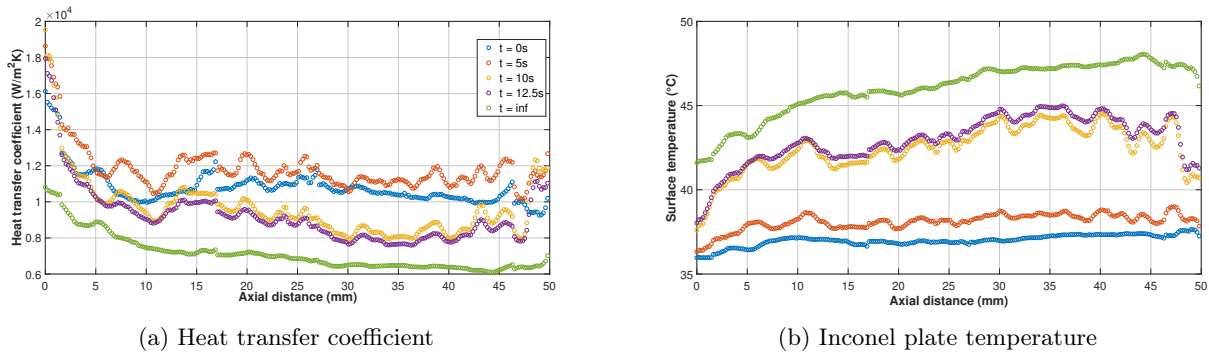

(b) Inconel plate temperature
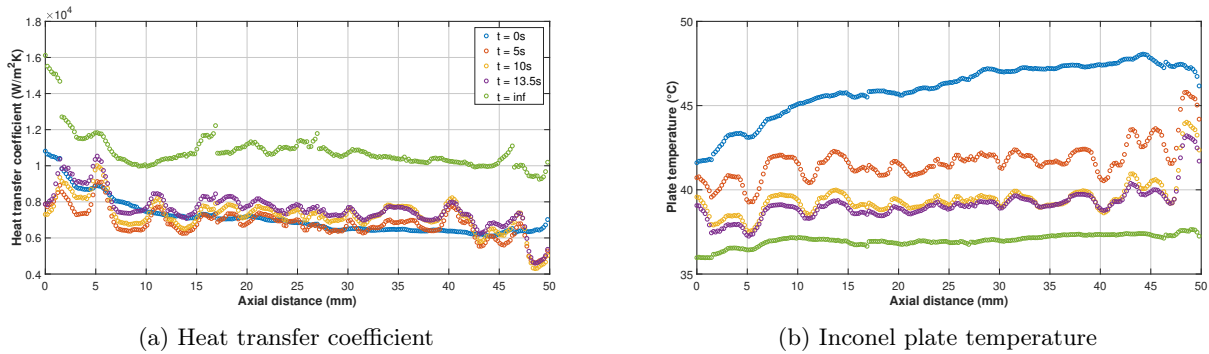
Figure 3.9: Evolution in time of different results along the channel during a decrease of the heat flux from 4.37 to 2.19 W/cm^2 with a mass flux of 414.13 kg/m^{2}s

The last graph presented in Fig. 3.10 shows the evolution of the measured inlet and outlet temperatures of the supercritical carbon dioxide. As expected, the outlet temperature drops rapidly when the heat flux decreases. After that rapid drop, the temperatures decreases slowly towards the new stable point (at 32.6°C for the inlet temperature).
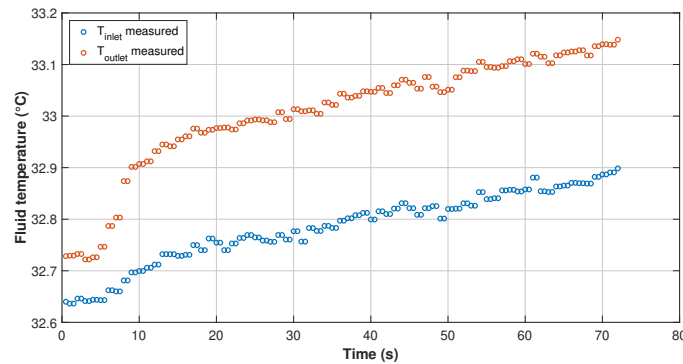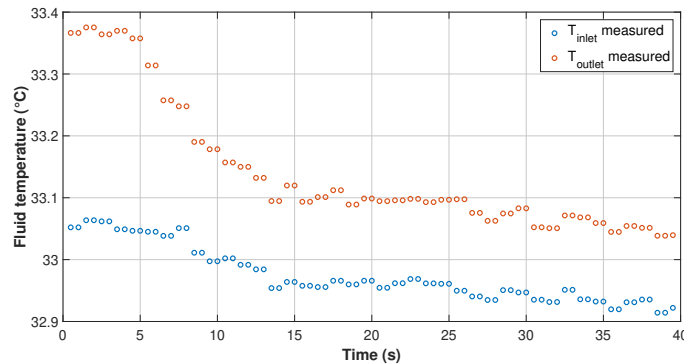

Figure 3.10: Evolution of the measured inlet and outlet temperatures of the carbon dioxide during a decrease in heat flux

From these two first transient tests, it is clear that some local phenomena are happening inside the channel when the heat flux is increased or decreased. Those phenomena could be linked to some kind of buoyancy as the buoyancy parameter clearly indicates the presence of some buoyancy. However, the value remained relatively low. Some testing at higher heat flux and with a higher buoyancy influence could potentially confirm this theory. As the transient test with the decreasing heat flux is showing some unexpected results, it would be necessary to perform some additional experiment to compare the response of the system in the event of an increase and a decrease in heat flux. Finally the same tests at different heat fluxes should be conducted to assess the impact of heat flux on the results.

3.2.5 Transient mass flux

The second varying parameter tested is the mass flux. The test is used to assess the reactivity of a system being controled by a varying mass flux to cool down a surface. Indeed, in an actual application, the mass flux is an easy to control parameter. The parameters at the start of the test are listed in Tab. 3.6. As can be seen, the mass flux increases by around 20% during a period of 5 seconds while keeping the heat flux constant.

The results of the test are shown in Fig. 3.6 with the increase in mass flux happening at 3s. As can be seen, the response of all different parameters is vary fast. Compared to the tests with the varying heat flux, the only similarity is in the evolution of the buoyancy in Fig. 3.11c that decreases linearly when the mass flux increases. This result also shows the large effect of the mass flux over the buoyancy as described in section 2.2.10. Indeed, even a small increase (20%) in mass flux results in a substantial decrease of the buoyancy parameter.

$T_{inlet,start}$ (°C)	$T_{outlet,start}$ (°C)	q'' (W/cm^2)	G_{start} (kg/m^{2}s)	G_{end} (kg/m^{2}s)	t_{start} (s)
32.48	32.7	4.37	490.29	578.70	4

Table 3.6: Parameters specification for the start of the transient test with the increase in mass flux ($P_R = 1.038$, $T_{PC} = 32.66$°C)

The biggest difference, compared to the test with the increase or decrease in heat flux, is the evolution of the heat transfer coefficient in Fig. 3.11a. In this case, the heat transfer coefficient follows the evolution of the mass flux without any delay at the start. The results even show a small overshoot in the heat transfer coefficient at the end of the increase that then stabilises. The system seems even pretty stable after only a few seconds following the end of the increase in mass flux.

Looking at the evolution of the plate temperature in Fig. 3.11b, its evolution is also faster than in the case of a change in the heat flux. The temperature decreases rapidly as soon as the mass flux changes and stabilises fast at the end as well.

(a) Mean heat transfer coefficient along the channel

(b) Mean Inconel plate temperature

(c) Mean of the buoyancy parameter
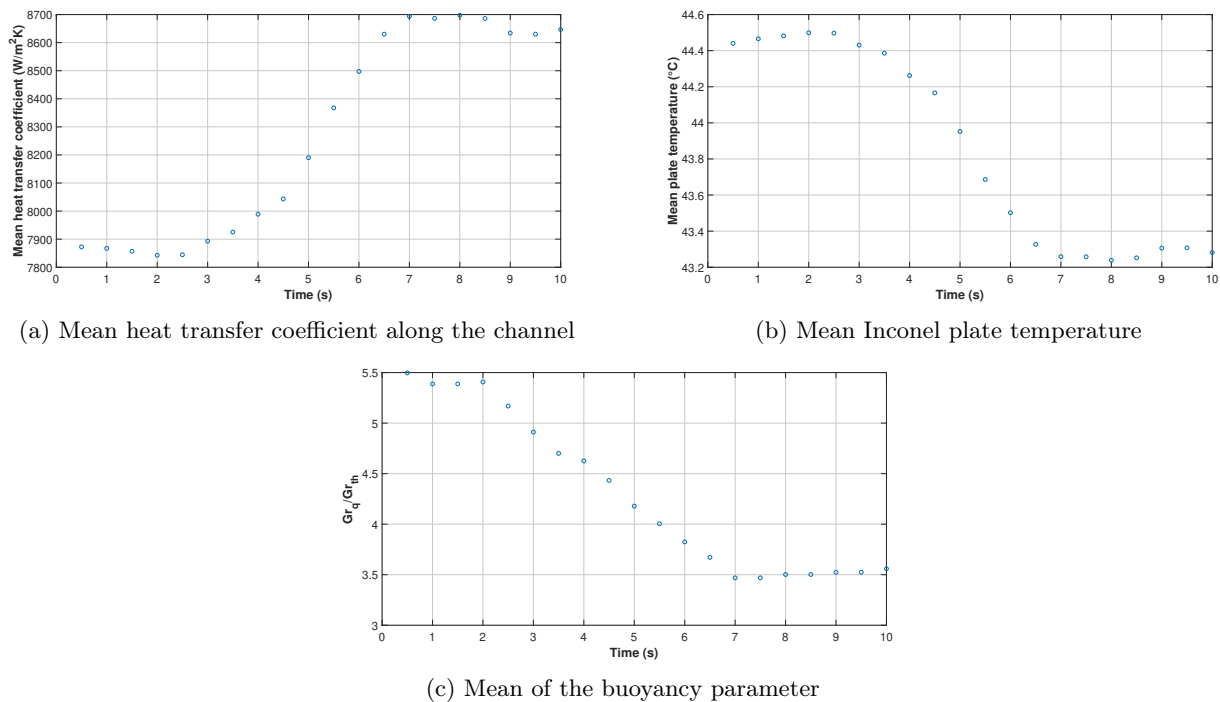
Figure 3.11: Evolution in time of the mean value of different results along the channel during an increase of the mass flux from 490.29 to 578.7 kg/m^{2}s with a heat flux of 4.37 W/cm^2

With the three parameters showing a fast convergence, it is interesting to look at the results all along the channel at different times to see if some local phenomena appear as well in this case. The results in Fig. 3.12, with the heat transfer coefficient in Fig. 3.12a and the plate temperature in Fig. 3.12b, clearly indicate the opposite. Both the heat transfer coefficient and the plate temperature evolve similarly all along the channel with an increase of the heat transfer coefficient and a decrease of the plate temperature. Moreover, the difference between the results at 7.5s and 10s shows that the system is already more stable than it was after the same period of time with a varying heat flux.

The last result displayed in Fig. 3.13 is the evolution of the measured inlet and outlet temperatures. This evolution shows that the system is not totally stable even if the previous results are indicating the contrary. This continuous variation in temperature comes from the interaction of all the parameters inside the loop. Indeed, the results indicate that the pressure in the loop is slightly decreasing, changing the pseudo-critical point and all the system converges to a new stable point. This new stable point is caused by the general decrease of the fluid temperature in the loop and all the components converging to a new stable point (notably the pre-heater and the post-cooler linked to the chiller).

(a) Heat transfer coefficient

(b) Inconel plate temperature
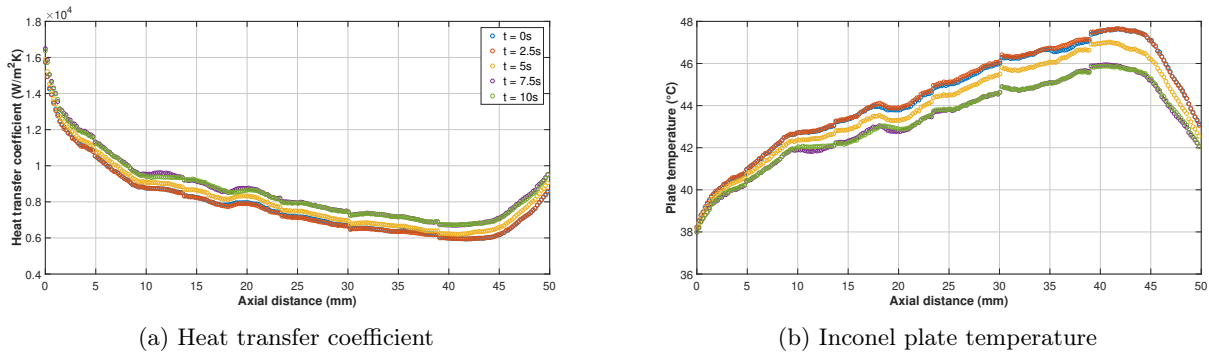
Figure 3.12: Evolution in time of different results along the channel during an increase of the mass flux from 490.29 to 578.7 kg/m^{2}s with a heat flux of 4.37 W/cm^2
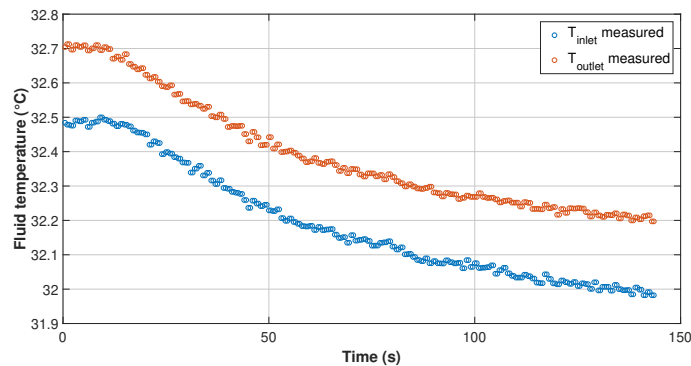
Figure 3.13: Evolution of the measured inlet and outlet temperatures of the carbon dioxide during an increase in mass flux

In conclusion of this Chapter, the response of the heat exchanger to a variation in mass flux seems very quick and with a better convergence than with a change in heat flux. Moreover, the results show that no instabilities are occurring as the plate does not show some cold or hot spot as in the previous sections. This good response of the system is really promising if the plate temperature was to be manage with the mass flux. However more testing are needed to see if those results are repeated for different mass fluxes and heat fluxes. It could also be interesting to look at the response of the system to a decrease of the mass flux. This analysis of the experimental tests in a transient regime concludes the experimental part and the theoretical models are developed in the following Chapters.

Chapter 4

Model for the steady-state heat exchange

In this chapter, the theoretical model of the heat exchanger analysed in steady-state condition is developed. The model was developed using the Engineering Equation Solver (EES) software and can be found in Appendix A.

4.1 Principle

The approach used is an electrical representation of the heat exchanger. A global overview is represented in Fig. 4.1 with the y-axis corresponding to the direction of discretization along the channel. The number of finite elements along the channel was set to 40 in order to keep a fast resolution and to have a node for every 6 points in the experimental data. Across the channel (corresponding to the x-axis), the Inconel plate is divided in three regions namely: the outer edge the channel and the side wall. The current flowing through the plate is divided by the total cross area of the Inconel sheet to determine the constant current density flowing in the different regions. The last axis (z-axis), orthogonal to the Inconel plate, is the one in which the heat exchange between the plate and the fluid happens. The grey layer around the Inconel sheet represents the perfect insulation assumption made to simplify the model. This assumption is made thanks to the good insulating properties of the Torlon plastic. An other assumption is that no heat goes through the bottom layer even with the presence of the camera view port for the middle channel.

The principle of the electrical representation is to give a temperature for every finite region represented by a node. This node is linked to other nodes by resistances representing the resistance in conduction or convection between the two corresponding nodes. The different equations used will be described in more detail in following sections. Apart from the heat exchange between the nodes, the heat generated by Joule effect in the Inconel sheet is also assumed to be 'injected' at the node representing the finite element.

4.2 Description

A global description of the model can be seen in Fig. 4.2 where the different inputs, outputs and parameters are represented. The inputs of the model are the current, the absolute pressure and the inlet temperature of the supercritical carbon dioxide and finally the mass flux. It is important to note that the model only represents the channels and not the header region, the inlet temperature is therefore not the one measured by the thermocouple but the one computed by the MATLAB model for the inlet of the micochannels.

The parameters of the model are the different geometrical dimensions of the channels. The value for each dimension is listed in Tab. 4.1. The initial goal of the study was to try different values for some dimensions to look at the effect of the geometry. But due to the limitation of time for the experimental part due to the Covid-19, this part of the study was abandoned and is left for further studies.

Finally, the main outputs of the model are:

- $\bar{T}_{sCO_2,i}$: the bulk flow temperature of the carbon dioxide (in °C) at the different node along the channel
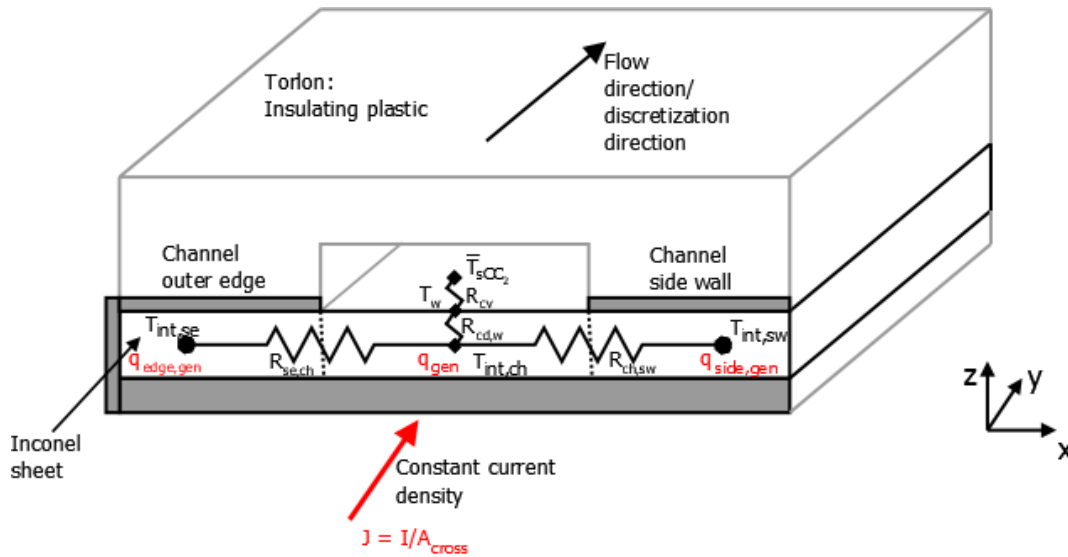
Figure 4.1: Scheme of the modelling of the heat exchanger

Thickness of the Inconel sheet: Th_B	254 µm
Length of the channel: L_B	50 mm
Width of the channel: W_{ch}	1.92 mm
Thickness of the channel side wall: Th_{SW}	1.5 mm
Thickness of the outer edge: Th_{SE}	1.5 mm
Height of the channel: H_{ch}	600 µm
Number of channel: N_{ch}	3
Absolute roughness of the channel walls: AR	0.78 µm

Table 4.1: Geometrical specification of the channels and the Inconel sheet in the model

- ΔP_{sCO_2}: the pressure drop of the carbon dioxide (in Pa)

- $h_{conv,i}$: the heat transfer coefficient in convection between the Inconel and the supercritical carbon dioxide (in W/m^{2}K) at the different node along the channel

- $T_{int,ch,i}$: the temperature of the Inconel sheet below the channel (in °C) at the different node along the channel

- $T_{int,sw,i}$: the temperature of the Inconel sheet below the side wall (in °C) at the different node along the channel

- $T_{int,se,i}$: the temperature of the Inconel sheet below the outer edge (in °C) at the different node along the channel

- q'': the heat flux (in W/m^2)

- Bo: the buoyancy parameter by Petukhov and Polyakov

- K_v: the acceleration parameter

Those outputs are computed for every node along the channel to see their evolution and be able to make some comparison with the experimental data points.

4.2.1 Evolution of the fluid properties along the channel

One of the main capabilities of the model is the evaluation of the fluid properties along the channel. As the fluid is in a supercritical state and is never under the saturation curve, the pressure and temperature are always independent from one another. Therefore, the different properties are always determined with the help of those two
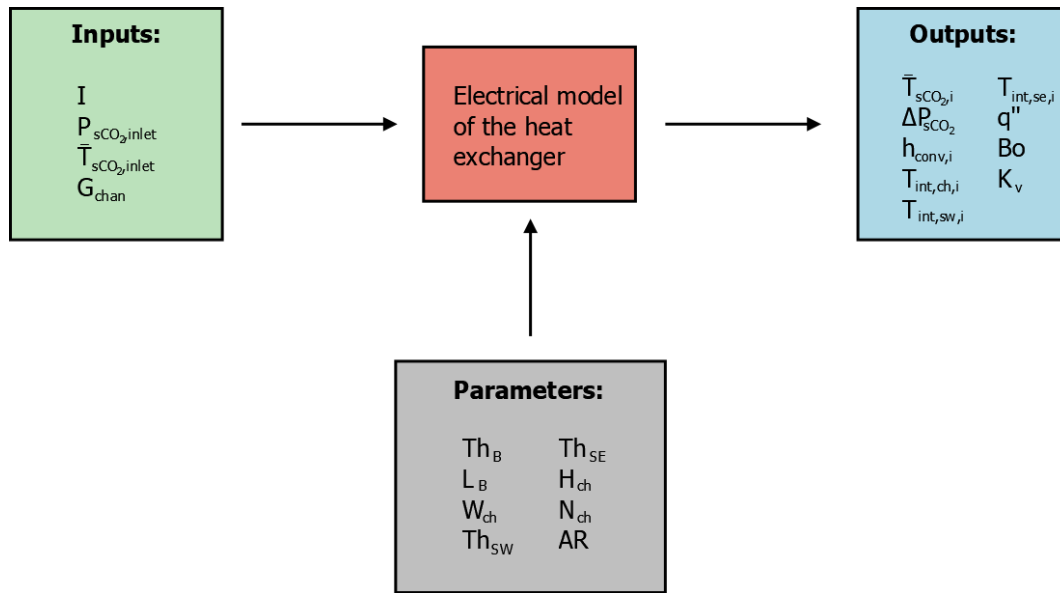
Figure 4.2: Input, output and parameters of the electrical representation of the heat exchanger

thermodynamic properties.

The assumption of constant pressure inside the heat exchanger is made as the pressure drop is small compared to the absolute pressure ($<0.1\%$). This assumption could lead to non negligible errors in the case of the modelling of larger microchannels based heat exchangers or in the case of a very large mass flux. An advantage of considering the pressure constant (apart from the simplicity to compute the properties) is that the pseudo-critical temperature is also considered constant along the channel as it only depends on the pressure. Its mathematical expression is presented in Eq. 4.1 where the pressure of the carbon dioxide is expressed in bar.

$$T_{PC} = -122.6 + 6.124 * P_{sCO2,bar} - 0.1657 * P_{sCO2,bar}^2 + 0.01773 * P_{sCO2,bar}^{2.5} - 0.0005608 * P_{sCO2,bar}^3 \qquad (4.1)$$

The other parameter, namely the bulk fluid temperature ($\bar{T}_{sCO_2}$) is increasing along the channel with the heat flux applied. Its evolution at a node 'i' is computed using a simple energy conservation at the wall of the Inconel sheet described in Eq. 4.2:

$$\dot{m}h_{i-1} + \frac{T_{w,i} - \bar{T}_{sCO_2,i}}{R_{conv}} = \dot{m}h_i \qquad (4.2)$$

The enthalpy of the carbon dioxide h_i is computed using a pre-built property function developed in EES. In the special case of the first node, the enthalpy of the node 'i − 1' is simply the enthalpy of the fluid taken at the inlet temperature. The other terms present in the equation are the mass flow $\dot{m}$, computed with the mass flux and the cross flow area, the wall temperature at the node T_w and the resistance in convection R_{conv}. The resistance in convection is computed at each nodes using a correlation (like the Dittus-Boelter correlation) to determine the Nusselt number. The Nusselt number is then used in Eq. 4.3 and 4.4 with the thermal conductivity k (taken at the bulk fluid temperature), the hydraulic diameters D_h and the area where the heat exchange occurs A_{conv}. The different correlations that can be used will be described in more detail in section 4.3 where their results will be compared to the experimental results.

$$R_{conv} = \frac{1}{h_{conv,i}A_{conv}} \qquad (4.3)$$

$$h_{conv} = \frac{Nuk_{bulk}}{D_h} \qquad (4.4)$$

With the temperature of the bulk fluid known and with the pressure assumed constant, all the other properties such as density, thermal conductivity, viscosity, Prandtl number,... can be updated.

4.2.2 Evolution of the Inconel temperature

As previously explained in section 4.1, the Inconel sheet is divided in three different regions: the outer edge, the side wall and the center below the channel. As the model is in steady-state, the temperature of the different parts can simply be computed using a general energy conservation equation.

The outer only sees heat exchange through conduction with the Inconel node under the channel and with the previous/next outer edge node along the channel. The general energy conservation equation at the node 'i' is expressed in Eq. 4.5. In the case of the first or last node, one of the heat exchange along the axis is not present in the equation. As can be seen, the general rule in the equation is to assume that the heat produced and the heat exchange with the previous node are entering the node. The other heat exchanges are leaving it.

$$q_{edge,gen,i} + \frac{T_{int,se,i-1} - T_{int,se,i}}{R_{ax,se,i-1}} = \frac{T_{int,se,i} - T_{int,ch,i}}{R_{se,ch,i}} + \frac{T_{int,se,i} - T_{int,se,i+1}}{R_{ax,se,i}} \tag{4.5}$$

In this case, all resistances are in conduction either along the channel (with $R_{ax,EE,i-1}$ and $R_{ax,EE,i}$) or across it (with $R_{se,ch,i}$) for the exchange with the center of the channel. Those resistancess in conduction are computed using the following equation:

$$R_{cond} = \frac{\Delta L}{k A_{cross}} \tag{4.6}$$

The thermal conductivity k is taken at the mean temperature of the two nodes between which the heat transfer is happening. The distance ΔL is taken from one node to the other (eg. between the outer edge and the center of the channel, the distance is $Th_{SE}/2 + W_{ch}/2$). Finally, A_{cross} is the cross area of the heat flow.

The heat generated q_{gen} is computed using the knowledge of the current (used as input in the model) with Eq. 4.7 and 4.8.

$$q_{gen} = (J A_{cross})^2 R_e \tag{4.7}$$

$$R_e = \frac{L \rho_e}{A_{cross}} \tag{4.8}$$

The current density 'J' is simply the total current going through the test section divided by the total cross area of the Inconel sheet. The cross area then used in the equations is the cross area of the studied element (eg. for the part of the Inconel below the channel $A_{cross} = W_{ch} \times Th_B$). Finally, the electrical resistivity ρ_e is taken at the temperature of the node concerned.

The side wall region temperature is assumed symmetric to the plane at half the thickness of the wall. This assumption is done as both sides of the wall are in contact with a channel where the carbon dioxide flows and in theory half of the heat produced under the side wall will go to one side and the other half to the other side. The side wall region is therefore divided in two with each part linked to one channel. With that, the node in the scheme of Fig. 4.1 is at a quarter of the thickness of the side wall and just like the outer edge, the heat exchanges happening are with the center part below the channel and with the previous/next node in the side wall along the channel. Therefore, the energy conservation is similar to the one of the outer edge and is described in Eq. 4.9. The only small difference being the expression of the heat exchange with the center expressed with the heat entering the node. Once more, this expression is for the node 'i' and in the case of the first/last node, one of the exchange along the channel would disappear.

$$q_{side,gen,i} + \frac{T_{int,sw,i-1} - T_{int,sw,i}}{R_{ax,sw,i-1}} + \frac{T_{int,ch,i} - T_{int,sw,i}}{R_{ch,sw,i}} = \frac{T_{int,sw,i} - T_{int,sw,i+1}}{R_{ax,sw,i}} \tag{4.9}$$

The last node representing a given volume of the Inconel sheet is the center part below the channel. The expression of the energy balance is slightly longer as there is two more heat exchanges than for the two other parts. The first one is due to the heat exchange to both sides (outer edge and side wall) and the second one is the heat exchange with the surface of the Inconel sheet. With those two additional heat exchanges, the expression becomes:

$$q_{ch,gen,i} + \frac{T_{int,ch,i-1} - T_{int,ch,i}}{R_{ax,ch,i-1}} + \frac{T_{int,se,i} - T_{int,ch,i}}{R_{se,ch,i}} = \frac{T_{int,ch,i} - T_{int,ch,i+1}}{R_{ax,ch,i}} + \frac{T_{int,ch,i} - T_{int,sw,i}}{R_{ch,sw,i}} + \frac{T_{int,ch,i} - T_{w,i}}{R_{ch,w,i}} \tag{4.10}$$

Finally, the last node present is the surface node. As this node is only representing the surface, no heat is produced at that node. Moreover, as the thickness is assumed negligible, no heat exchange happens along the channel through the surface. The surface only sees two heat exchanges. One with the fluid through convection and one in conduction with the center of the Inconel sheet below the channel. The energy conservation equation is therefore simply:

$$\frac{T_{int,ch,i} - T_{w,i}}{R_{ch,w,i}} = \frac{T_{w,i} - T_{F,i}}{R_{conv,i}} \tag{4.11}$$

The resistance in conduction is computed with Eq. 4.6 where the distance is simply half the thickness of the Inconel sheet. The resistance in convection is computed using the method presented in the previous section with the Eq. 4.3 and 4.4 and the different correlations for the Nusselt number.

4.2.3 Pressure drop

An other part of the model is dedicated to the pressure losses in the microchannels. As the model describes only the channels, no minor loss such as the reduction of cross flow area between the header region and the inlet of the channel is present in the model. The total pressure loss can be decomposed in two terms. The pressure loss due to the acceleration of the fluid inside the channels (due to the change of density) and the pressure loss due to friction.

The pressure loss associated with the acceleration of the flow is evaluated by Eq. 4.12. As can be seen, this pressure losses is proportional to the density which means that in the case of a test around the pseudo-critical point where the density sees a rapid decrease, this loss can be substantial.

$$\Delta_{P,acc} = (\rho_{out} V_{out}^2 - \rho_{in} V_{in}^2) \tag{4.12}$$

For the pressure loss due to friction, the Darcy friction factor for turbulent flow (shown in Eq. 4.13 to 4.15) is used. The Reynolds number is computed using the bulk flow temperature at the inlet and the absolute pressure to determine the viscosity. As the flow is turbulent for all the experiments, no friction factor for a laminar flow was used. The pressure loss is then computed using Eq. B.10 where the density and velocity are evaluated at the bulk flow temperature. Finally, the total pressure drop is simply the addition of the losses due to friction and acceleration as described in Eq. 4.17.

$$f_{turb} = 8 \left[\frac{8}{Re_{D_h}} \right]^{12} + (\theta_1 + \theta_2)^{-1.5} \Big]^{\frac{1}{12}} \tag{4.13}$$

$$\theta_1 = \left[2.457 ln \left[\left[\frac{7}{Re_{D_h}} \right] + 0.27 \frac{R_a}{D_h} \right]^{-1} \right]^{16} \tag{4.14}$$

$$\theta_2 = \left[\frac{37530}{Re_{D_h}} \right]^{16} \tag{4.15}$$

$$\Delta_{P,fric} = f_{turb} \frac{L_{chan}}{D_h} \frac{V_{chan}^2}{2} \rho_{chan} \tag{4.16}$$

$$\Delta_{P,tot} = \Delta_{P,fric} + \Delta_{P,acc} \tag{4.17}$$

4.2.4 Study of the buoyancy and the acceleration effects

An other important part of the model is the study of the buoyancy and the acceleration effects. Indeed, as was shown in the different results presented in section 2.2, the buoyancy is well present and even if some further study analysis (notably with a heat exchanger with the upper plate heated) is needed to quantify the effect, it is interesting to have more information about when to expect some effects. For the acceleration, it was shown that its impact is minor in this case but is nonetheless included to see if its influence can be significant in some cases that were not part of the experimental study.

For the buoyancy, the criterion used is the one from Petukhov and Polyakov as it is the best suited according to the literature [24]. The different parameters present in Eq. 4.18 to 4.21 are explained in details in section 1.1.3. The threshold value for the buoyancy parameter described in Eq. 4.22 is 1. Any value of Bo above 1 indicates the presence of some buoyancy effects and the higher the parameter, the greater the effect.

$$Gr_{th} = 3 \times 10^{-5} Re_b^{2.75} \bar{Pr}^{0.5} [1 + 2.4 Re_b^{-1/8} (\bar{Pr}^{2/3} - 1)] \tag{4.18}$$

$$\bar{Pr} = \frac{h_w - h_b}{T_w - T_b} \frac{\mu_b}{k_b} \tag{4.19}$$

$$Gr_q = \frac{g \bar{\beta} q'' D_h^4}{\nu_b^2 k_b} \tag{4.20}$$

$$\bar{\beta} = \frac{1}{\rho_{film}} \frac{\rho_b - \rho_w}{T_w - T_b} \tag{4.21}$$

$$Bo = \frac{Gr_q}{Gr_{th}} \tag{4.22}$$

, two criteria were presented in section 1.1.3. The first one described by Eq. 4.23 to 4.26 is not adapted to asymmetric heating and therefore overestimates the effect of the acceleration in asymmetric heating conditions.

Concerning the impact of the acceleration, a semi-empirical model was created by [9] for its effect in uniformly heat tubes. This model is developed in details in [9]. The idea is to compare the heat transfer between the normal case and the case where the acceleration is taken into consideration and is reducing the shear stress. Base on that, correlations relating the friction and the heat transfer are used to find a relation between the shear stress and the heat transfer. Once it is done, a relation between the two Nusselt numbers can be defined in Eq.1.7. In this equation, Nu_b is the Nusselt number influenced by the acceleration and Nu_{b_0} is the one without its influence. If the acceleration parameter A_{cb} is small enough and that $C_A A_{cb} F_{VP1}$ is smaller than 0.385, the influence of the acceleration over the heat transfer will be less than 2%.

$$\frac{Nu_b}{Nu_{b_0}} = \left[|1 - C_A A_{cb} F_{VP1} \left(\frac{Nu_b}{Nu_{b_0}} \right)^{-1.1} | \right] \tag{4.23}$$

$$C_A = 10^4 \tag{4.24}$$

$$A_{cb} = \frac{\beta_b q'' D}{k_b Re_b^{1.625} Pr_b} \tag{4.25}$$

$$F_{VP1} = \left(\frac{\mu_{ave}}{\mu_b} \right) \left(\frac{\rho_{ave}}{\rho_b} \right)^{-0.5} \tag{4.26}$$

However, this model developed for uniformly heated tubes is not adapted to asymmetric heating and therefore overestimates the effect of the acceleration in asymmetric heating conditions. To account for the different boundary condition, a new criterion was developed by McEliot [3]. The new criterion is described in Eq. 4.27. The similarity to the acceleration parameter A_{cb} is obvious, the main change being the addition of the relation between the heated parameter Per_{heated} and the perimeter of the channel. The threshold value for the apparition of the effect of

the acceleration is when $K_v > 9.5 \times 10^{-7}$. Below that value, the flow can be considered still fully turbulent and with no impact from the acceleration. An extreme case of the acceleration is the transition of the boundary layer to a laminar one, decreasing substantially the thermal transport and reducing the heat transfer coefficient. The threshold for that transition is $K_v > \approx 2 - 3 \times 10^{-6}$.

$$K_v = \frac{4(Per_{heated}/Per_h)q^+}{Re_b} \tag{4.27}$$

$$q^+ = \beta q_w''/Gc_p \tag{4.28}$$

4.2.5 Correlation to compare to the experimental results

In order to get the best accuracy possible, different correlations are compared to the experimental results in order to implement the most accurate in the predictive model. As the heat exchanges happen around the pseudo-critical point, the Dittus-Boelter correlation is showing some large errors in its prediction according to [28]. Some more complex correlations taking into account the evolution of the density or other properties of the carbon dioxide might give better results in the temperature range seen in this case. However, the Dittus-Boelter correlation, expressed in Eq. 4.29, is still part of the study (and will be compared to the experimental results) as its results away from the pseudo-critical points are good. The Reynolds number is computed using the hydraulic diameter and the viscosity at the bulk fluid temperature. The Prandtl number is taken at the average temperature of the wall and bulk fluid.

$$Nu = 0.023Re_b^{0.8}Pr_b^{0.4} \times 0.91 \tag{4.29}$$

The second correlation used is a modified version of the Dittus-Boelter correlation developed by Miropolski and Shitsman [47] and expressed in Eq. 4.30. In this correlation, instead of looking at single Prandtl number, both the Prandtl at the wall and at bulk flow temperatures are computed and the minimal value is retained. Just like the Dittus-Boelter correlation, it presents the advantage of being extremely easy to compute but contrary to the Dittus-Boelter correlation, it takes into account the wall temperature. Indeed, considering that temperature can potentially greatly improve the results observed, especially in the case of large differences in temperature between the wall and the fluid.

$$Nu = 0.023Re_b^{0.8}Pr_{min}^{0.8} \tag{4.30}$$

The third correlation, expressed in Eq. 4.31, is a correlation developed by Ornastsky (1970) and is derived from the Miroposki-Shitsman correlation [47]. This correlation aims to take into consideration the variation of the density across the boundary layer to improve the results, notably close to the pseudo-critical point. Indeed, the density gradient inside the boundary layer plays an important role in the heat exchange as it is at the origin of the buoyancy.

$$Nu = 0.023Re_b^{0.8}Pr_{min}^{0.8} \left(\frac{\rho_w}{\rho_b}\right)^{0.3} \tag{4.31}$$

The last correlation used is the one developed by Jackson and Hall (1979) [2] and its expression is as follows:

$$Nu = 0.0183Re_b^{0.82}Pr_b^{0.5} \left(\frac{\rho_w}{\rho_b}\right)^{0.3} \left(\frac{\bar{c}_p}{c_{p_b}}\right)^n \tag{4.32}$$

$$\bar{c}_p = \frac{h_w - h_b}{T_w - T_b} \tag{4.33}$$

This correlation takes into account the evolution of the density gradient across the boundary layer. In order to account for the non-uniformity of the fluid properties, an additional correcting factor is added. This factor, using

the integrated specific heat capacity $\bar{c}_p$, as its exponent n varying with the value of T_w and T_b compared to T_{PC}. The different values and their conditions are as follows:

$$n = 0.4 \text{ for } T_b < T_w < T_{PC} \text{ and for } 1.2T_{PC} < T_B < T_w \tag{4.34}$$

$$n = 0.4 + 0.2\left(\left(\frac{T_w}{T_{PC}}\right) - 1\right) \text{ for } T_b < T_{PC} < T_w \tag{4.35}$$

$$n = 0.4 + 0.2\left(\left(\frac{T_w}{T_{PC}}\right) - 1\right)\left(1 - 5\left(\left(\frac{T_b}{T_{PC}}\right) - 1\right)\right) \text{ for } T_{PC} < T_b < 1.2T_{PC} \text{ and } T_b < T_w \tag{4.36}$$

4.2.6 Comparison with the experimental results

In this section, the four correlations will be compared to the experimental results. The different temperatures for the correlations are directly taken from the analysis and the comparison is made on the heat transfer coefficient.

In order to compare the different correlations, the mean absolute percentage error (MAPE) expressed in Eq. 4.37 is used. This criterion, where N is simply the total number of points studied, compares the measured heat transfer coefficient $h_{conv,exp}$ to the computed one using the correlation $h_{conv,corr}$. In order to have a better idea of the precision of the different correlation, the data of the 20 first points as well as the 20 last are ignored. Indeed, the heat transfer is induced at the inlet and outlet due to the geometry and the flow as explained in section 2.2.6. This increase being unrelated to the fluid properties, the different correlations can not predict it properly. Therefore, those results are ignored to stay as objective as possible.

$$MAPE = \frac{100\%}{N} \sum_{i=1}^{N} \left| \frac{h_{conv,exp} - h_{conv,corr}}{h_{conv,exp}} \right| \tag{4.37}$$

4.2.6.1 Results away from the pseudo-critical point

The first comparison of the different correlations is done on a test performed away from the critical point previously used for the data validation. As can be expected based on the literature, the Dittus-Boelter correlation is the one giving the best results in Fig. 4.3. In order to keep a readable graph, the uncertainty error is displayed only for the experimental data analysis.
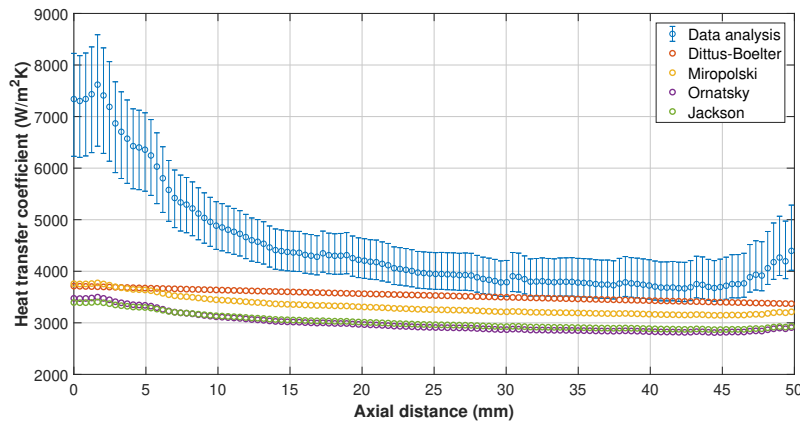
Figure 4.3: Comparison between the heat transfer coefficient of the data analysis and the correlations for a test performed away from the pseudo-critical point ($T_{inlet} = 40.1°C$, $P_R = 1.04$, $G = 567$ kg/m^{2}s, $q'' = 5.69$ W/cm^2)

The Dittus-Boeleter correlation has a MAPE value between 5 and 15% lower than the other correlations shown in Tab. 4.2. Once more, the effect of the inlet and outlet over the heat flux is clear with all the correlations showing a nearly constant heat transfer coefficient all along the channel. However, contrary to the results presented in [28], the MAPE value for these correlations remains quite good. Moreover, if the results were computed on the part of

the data analysis where the heat transfer coefficient is really stable (between 20 and 45mm in Fig. 4.3), those values would be even lower. Therefore, in the case of a test only occurring far from the critical point, the Dittus-Boelter correlation should be preferred as the heat transfer is similar to a single phase turbulent heat transfer. However, the other correlations give acceptable results and may be preferred over the Dittus-Boelter correlation for cases where a part of the heat exchange of the heat exchanger is close to the pseudo-critical point..

	Dittus-Boelter	Miropolski and Shitsman	Ornatsky	Jackson and Hall
MAPE (%)	15.46	21.35	29.49	28.43

Table 4.2: MAPE results for the different correlation away from the critical point ($T_R = 1.025$

4.2.6.2 Results close to the pseudo-critical point

Following the analysis far from the pseudo-critical point, it is important to look at the results closer to it. This is done by analysing the MAPE value of the different correlations for several tests with different heat fluxes, mass fluxes and inlet temperatures. The goal is to find the correlation that gives the best results in the majority of the cases.

The first couple cases to be looked at are two tests with a small heat flux (q''=6.88 W/cm^2) but with two different inlet temperatures. The results of the test with the lower inlet temperature are shown in Fig. 4.4a and the results in Fig. 4.4b correspond to the higher inlet temperature. The MAPE results for those two tests are presented in Tab. 4.3. Both in the figures and the table, the difference between the results of the Dittus-Boelter correlation is very large. Compared to this, the three other correlations have better results, especially in the second case. In all cases, the difference is much lower than for the Dittus-Boelter correlation.

(a) $T_{inlet)} = 31.06°C$, $G = 485.99$ kg/m^{2}s

(b) $T_{inlet)} = 32.78°C$, $G = 493.25$ kg/m^{2}s
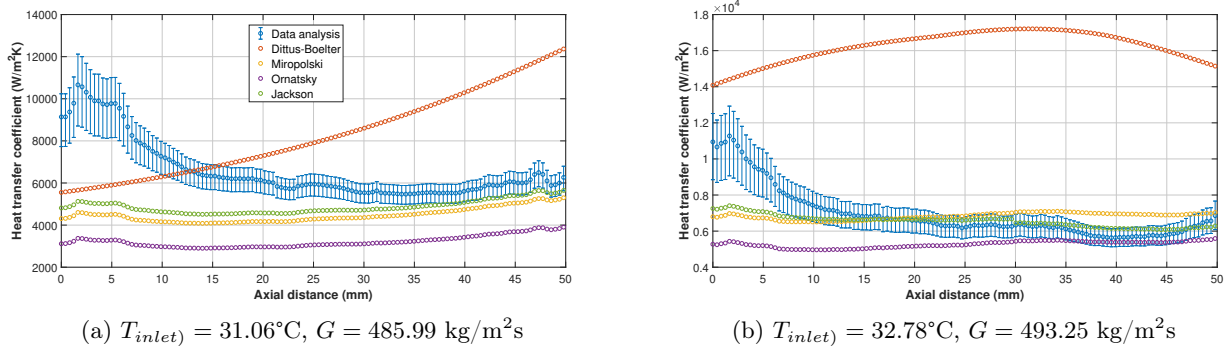
Figure 4.4: Comparison between the heat transfer coefficient from the data analysis and the correlations close to the critical point with a heat flux q'' of 6.88 W/cm^2

Inlet temperature (°C)	Heat flux (W/cm^2)	Mass flux (kg/m^{2}s)	Dittus -Boelter	Miropolski and Shitsman	Ornatsky	Jackson and Hall
31.06	6.88	485.99	43.74%	28.86%	49.13%	22.47%
32.78	6.88	493.25	154.69%	13.08%	19.42%	6.67%

Table 4.3: MAPE results for the correlation with two different tests

The large error difference for the Dittus-Boelter correlation between the two different tests comes from the fact that the fluid temperature for the first test in Fig. 4.4a does not reach to the pseudo-critical temperature while the second one in Fig. 4.4b does. As the correlation uses the bulk fluid temperature for the Prandtl number to compute the Nusselt number (in Eq. 4.29) but also the thermal conductivity k to compute the heat transfer coefficient (in Eq. 4.4), the difference close to the pseudo-critical temperature (in Fig. 4.4a) and at the pseudo-critical temperature (in Fig. 4.4b) can be significant. Indeed, looking at the evolution of those two fluid properties close to the pseudo-critical temperature in Fig. 4.5, the value of the Prandtl number is multiplied by 4 from 32°C to 33°C and the thermal conductivity increases substantially as well at the same time. In Fig. 4.4b, a maximum is even reached when the bulk fluid temperature reaches the pseudo-critical temperature between the 30th and 35th

mm of the channel. Moreover, contrary to the other correlations used, the Dittus-Boelter one is not taking into consideration the temperature of the wall (ranging between 40 and 50°C for the two tests) that influences the heat exchange in the boundary layer.
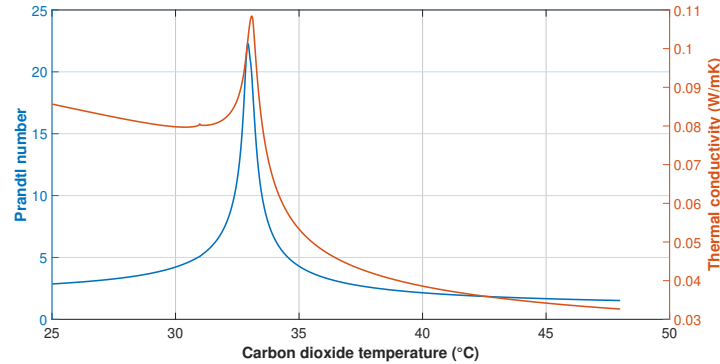
Figure 4.5: Evolution of the Prandtl number and the conductivity of the supercritical carbon dioxide ($PP_R =1.05$) with the temperature

Concerning the three other correlations, the one from Jackson and Hall is the best one in both cases with the Miropolski-Shitsman giving nearly identical results as both curves have the same shape and nearly overlap. The correlation from Ornatsky has also the same shape but with a higher error. As those three correlations give promising results, more tests are performed to compare them to experimental data points. However, considering the bad results of the Dittus-Boelter in this case, it will not be used in the predictive model. This correlation should only be used for really small heat flux (i.e. when the temperature difference between the wall and the bulk fluid is low) or when the flow is far from the pseudo-critical point.

The three correlations are compared to all the available data points, the detailed list of all the tests with the corresponding MAPE results of the different correlations is exposed in Tab. C.1 in Appendix C. All those tests are done at a constant pressure ($P_R = 1.05$) with a corresponding pseudo-critical temperature of 33°C. To give an overview of the different tests, the results for four different cases are displayed in Fig. 4.6.

Fig. 4.6a shows the results for a test with a lower inlet temperature. As can be seen, the correlation that fits the results the best is the one from Jackson and Hall in purple as its MAPE result is less than 15%. The curve is also discontinuous due to the change of the value of the exponent for the correction factor 'n' in Eq. 4.32. The discontinuity happens as the fluid temperature reaches the pseudo-critical point and the condition $T_B < T_{PC} < T_w$ is not respected anymore. This discontinuity is notable in the three other figures. The two other correlation have a similar MAPE results even though the curves have different shapes. The Ornatsky correlation underestimates the heat transfer coefficient at the start but once the fluid is closer to the pseudo-critical point, the results fit well the experimental data. The Miropolski correlation does the opposite, the results are acceptable at the start but once the fluid temperature is closer to the pseudo-critical temperature, the correlation overestimates the results.

The second figure, Fig. 4.6b, corresponds to a test with a higher inlet temperature but a lower heat flux of only 8.74 W/cm². The Miropolski correlation is once more overestimating the heat transfer coefficient all along the channel (except a the start due to the influence of the inlet) and presents the worst results with a 20% MAPE result. Both the Orntsky and the Jackson and Hall correlations give really good results and fit the curve well with a slightly better results for Jackson and Hall due to a better approximation at the start where Ornatsky underestimates the heat transfer coefficient similar to the the first figure.

The same results are observed with a higher mass flux in Fig. 4.6c and a lower one in Fig. 4.6d. The Moropolski, while giving descent results with a MAPE of around 20-25%, the simplicity of this correlation is showing its limit compared to the other ones when the heat transfer occurs close to the pseudo-critical point. The Ornatsky correlation tends to underestimates the results at the start when the pseudo-critical point is not yet reached. Indeed before the discontinuity in the Jackson and Hall curve, the Ornatsky correlation is always under the data analysis results. However after that point the results are really good. Overall, the correlation from Jackson and Hall gives the best results all around. Its mean MAPE results over all the tests presented in Tab. C.1 in Appendix C is 8.69% while the Ornastky correlation has 17.16% and the Miropolski correlation 23.99%.
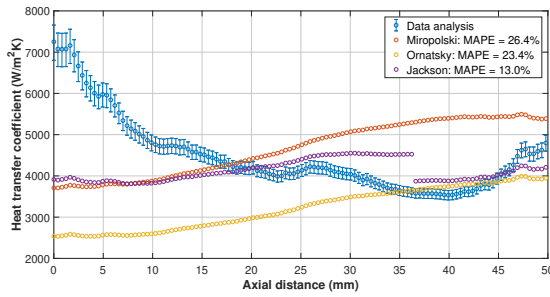
(a) $T_{inlet} = 31.73°C$, $T_{outlet} = 33.12°C$, $G = 488.65$ kg/m^{2}s and $q'' = 12.8$ W/cm^2
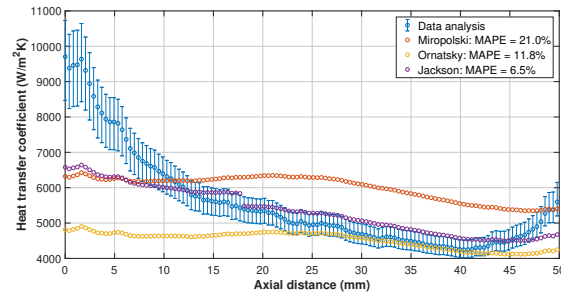
(b) $T_{inlet} = 32.80°C$, $T_{outlet} = 33.46°C$, $G = 483.67$ kg/m^{2}s and $q'' = 8.74$ W/cm^2
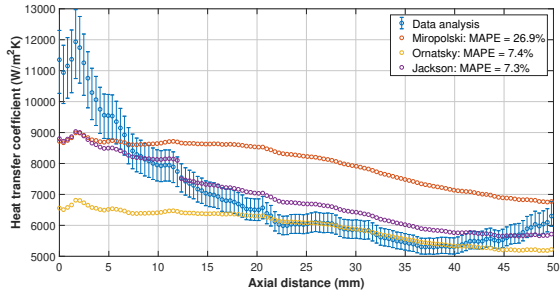
(c) $T_{inlet} = 32.89°C$, $T_{outlet} = 33.72°C$, $G = 744.08$ kg/m^{2}s and $q'' = 13.41$ W/cm^2
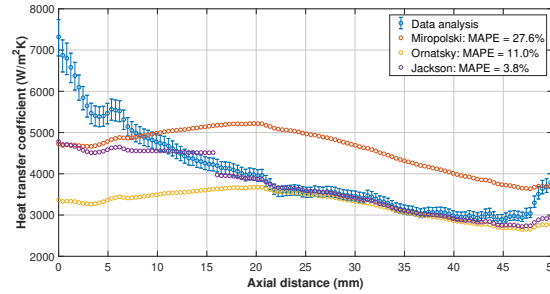
(d) $T_{inlet} = 32.77°C$, $T_{outlet} = 34.15°C$, $G = 463.48$ kg/m^{2}s and $q'' = 12.8$ W/cm^2

Figure 4.6: MAPE results for four different tests

Considering those results, the Jackson and Hall correlation is used to compute the Nusselt number and therefore the thermal resistance in convection in the predictive model.

4.3 Model validation

With the correlation selected, the model is now complete and its results can be compared to the experimental data. In this section, the model is validated with the experimental results. The next section is dedicated to look at the influence of different parameters with some actual quantitative numbers as the results of the theoretical model are not affected by the channel inlet. Moreover, the theoretical model allows to look at the effect of a parameter while keeping the others exactly constant which is nearly impossible in an experimental study.

In order to keep a logic in the results displayed, the tests shown to validate the model are the same than in Fig. 4.6 (the rest is listed in Tab C.2 in Appendix C). They are displayed in Fig. 4.7. An additional information is added for the parameters of the tests. This new parameter is the temperature at the inlet of the channel. Indeed, as explained in section 4.2, the model only describes the channels region but not the header region. Therefore the temperature measured by the sensor at the inlet is not the same than the one used for the model. The temperature used is the one computed in the data analysis at the entrance of the channels.

The first thing to note in the results is the huge difference between the model and the data analysis at the start of the channel further showing the effect of the inlet of the channels over the heat transfer happening there. As the model was developed without aiming at the representation of those effect, the mean absolute percentage error is only calculated starting at a quarter of the length of the heat exchanger (10 out of the 40 finite element of the model are neglected). The worst prediction is in Fig. 4.7a with a 17% MAPE result. This was already the case in Fig. 4.6 when the different correlations were compared to the data analysis. Similarly, the best result is for the last case in Fig. 4.7d where the data analysis is really well fitted by the model. The two other cases in Fig. 4.7b and 4.7c are also well approximated with a MAPE results of 15% or less. This is the case for most of the tests performed in this study which indicates a good prediction of the model.

In some case, the large effect of the inlet over the heat transfer coefficient leads to some false interpretation notably with the place of the peak of the heat transfer coefficient. This is most notable with the test with a lower
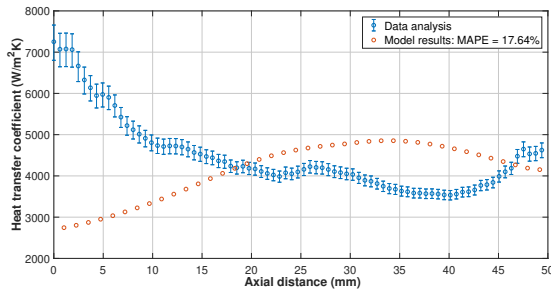
(a) $T_{inlet} = 31.73$°C, $T_{in,chan} = 32.21$°C, $T_{outlet} = 33.12$°C, $G = 488.65$ kg/m^{2}s and $q'' = 12.8$ W/cm^2
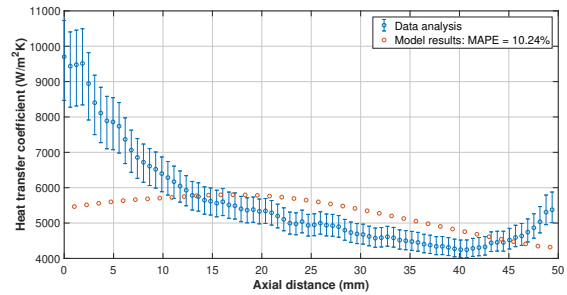
(b) $T_{inlet} = 32.80$°C, $T_{in,chan} = 32.88$°C, $T_{outlet} = 33.46$°C, $G = 483.67$ kg/m^{2}s and $q'' = 8.74$ W/cm^2
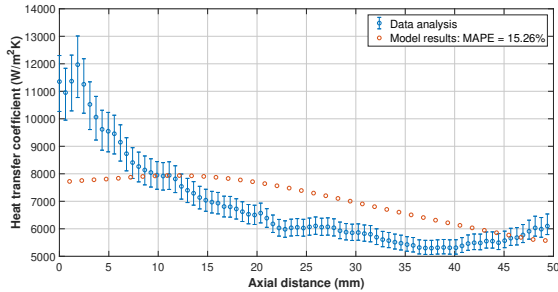
(c) $T_{inlet} = 32.89$°C, $T_{in,chan} = 32.96$°C, $T_{outlet} = 33.72$°C, $G = 744.08$ kg/m^{2}s and $q'' = 13.41$ W/cm^2
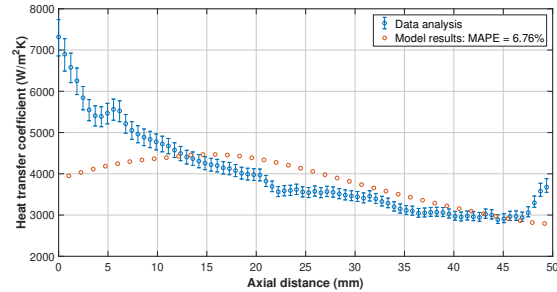
(d) $T_{inlet} = 32.77$°C, $T_{in,chan} = 32.94$°C, $T_{outlet} = 34.15$°C, $G = 463.48$ kg/m^{2}s and $q'' = 12.8$ W/cm^2

Figure 4.7: Model validation of the predictive model for four different tests

inlet temperature and a relatively low heat flux that present the worse predictions of all the tests. Looking at Fig. 4.8, the model gives a bad prediction of the heat transfer coefficient showing how strong the impact of the inlet really is. Indeed, the model shows a clear increase of the heat transfer coefficient all along the channel and only reaches the value of the experimental data at the end. In the figure, an other prediction was added (in yellow) with a channel inlet temperature slightly higher than the one given by the data analysis and the results are much better. The improvement of the results with a slightly higher channel inlet temperature could be observed for most of the tests. In Fig. 4.7, this would be represented by a slight shift of the red curve to the left, it is easy to see that besides maybe the case in Fig. 4.7a, the prediction would be better with that small shift. The reason behind this error could be a small underestimation in the heat generated inside the header region.

Finally, without the impact of the inlet of the channels, it is clear that the heat transfer coefficient does not see such a sharp peak as could be observed in the experimental results. Indeed the predictions of the model show indeed a peak reached as expected with the good properties around the pseudo-critical point but no huge drop in the heat transfer coefficient happens over such a small distance.
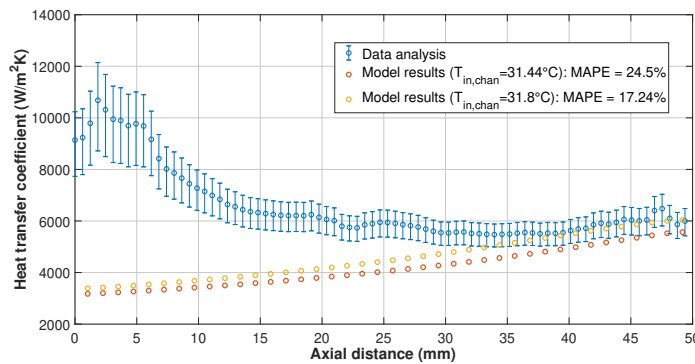
Figure 4.8: MAPE results of the model for a test with a low inlet temperature and a low heat flux ($T_{inlet} = 31.06$°C, $T_{in,chan} = 31.44$°C, $T_{outlet} = 32.62$°C, $G = 485.99$ kg/m^{2}s and $q'' = 6.88$ W/cm^2)

In conclusion, apart from the large impact of the inlet of the channels, the model shows good results with 87% predicted with a mean absolute percentage error of less than 20% and an average result of 12.39% over those 87% of the experimental data points. The model can therefore be considered valid and the influence of the different parameters can be studied.

4.4   Model results

In this section, the influence of the different parameters previously studied with the experimental results are analysed with the model. This study is done to give some quantitative data as the one from the experimental data are heavily impacted by the inlet of the channels. Moreover, the model allows to keep some of the parameters perfectly equal to really see the influence of one parameter alone. Finally, the model is useful as it can be used to simulate tests that were not experimentally tested.

An important thing to note is the meaning of the heat flux. Previously, in the experimental results, the heat flux indicated was the one produced below the channel but the fluid is seeing nearly twice that amount as the heat from the side walls and the edges goes to the fluid from the bottom as well. In this theoretical study, the heat flux corresponds to the one seen directly by the fluid taking into account all the heat from the sides walls and edges. Therefore a heat flux of 20 W/cm^2 in the theoretical study corresponds to a 10 W/cm^2 in the experimental study.

4.4.1   Effect of the inlet temperature

In this section, the effect of the inlet temperature is studied. In the experimental part (in section 2.2.9), it was found that the impact of the inlet temperature was rather low on the results. The maximal heat transfer coefficient was supposed to increase with an inlet temperature closer to the pseudo-critical point but at the cost of a small increase the pressure drop. Another point was the decrease of the buoyancy effect with the increase of the inlet temperature. Finally, another observation was that it is possible to optimize the inlet temperature at the inlet to minimize the plate temperature.

The results using the model for an inlet temperature varying between 32.2°C and 33°C (the pseudo-critical temperature being 33.05°C) are represented in Fig. 4.9. The other parameters are fixed with a mass flux of 500 kg/m^{2}s and a heat flux of 19.8 W/cm^2.

Looking at the results of the model in Fig. 4.9, it is clear that the interpretation of the experimental results showing an increase of the maximal heat transfer coefficient was caused by the effects of the inlet of the channels. Indeed, Fig. 4.9a shows a constant maximum heat transfer coefficient of 6050 W/m^{2}K. However it is important to note that the bulk flow reaches the pseudo-critical temperature inside the test section for all the inlet temperature tested here. If the inlet temperature is too low for the fluid to reach the pseudo-critical temperature, the heat transfer coefficient does not reach its peak and the maximum value will occur at the end of the channel while still increasing. On the contrary, if the inlet temperature is higher than the pseudo-critical temperature, the heat transfer coefficient will decrease all along the channel as the peak would occur before the inlet of the channels. Unlike the maximal heat transfer coefficient, the mean heat transfer coefficient inside the channel can be optimized to decrease the temperature of the plate (as shown in Fig. 4.9b). In order to have the best mean heat transfer coefficient, the peak in heat transfer coefficient must occur around the middle of the channel. Looking in Fig. 4.10, it is clear that the mean value of the curve corresponding to 32.8°C as inlet temperature is higher than the mean value of the other curves. This optimization depends both on the heat flux and the mass flux as an increase of heat flux will cause the bulk fluid temperature to increase faster (the pseudo-critical temperature will be reached sooner and with it the peak in heat transfer coefficient) and an increase of mass flux will have the opposite effect. Those effects are detailed in the following sections.

Concerning the effect of the buoyancy, both the model (in Fig. 4.9c) and the experimental results show a decrease of the buoyancy parameter when the inlet temperature increases. This is explained by the lower density gradient across the boundary layer when the fluid starts at a higher temperature and therefore a lower density.

The last results in Fig. 4.9d show the evolution of the pressure drop with the inlet temperature increasing. As can be seen, between the lowest and highest inlet temperature present in the graph, the pressure drop increases by 20%. This increase comes from the evolution of the bulk flow towards a 'vapor-like' state increasing the pressure drop along the channel. With a higher inlet temperature, the bulk fluid starts closer to that state and the pressure

(a) Heat transfer coefficient

(b) Inconel plate temperature

(c) Buoyancy parameter

(d) Pressure drop
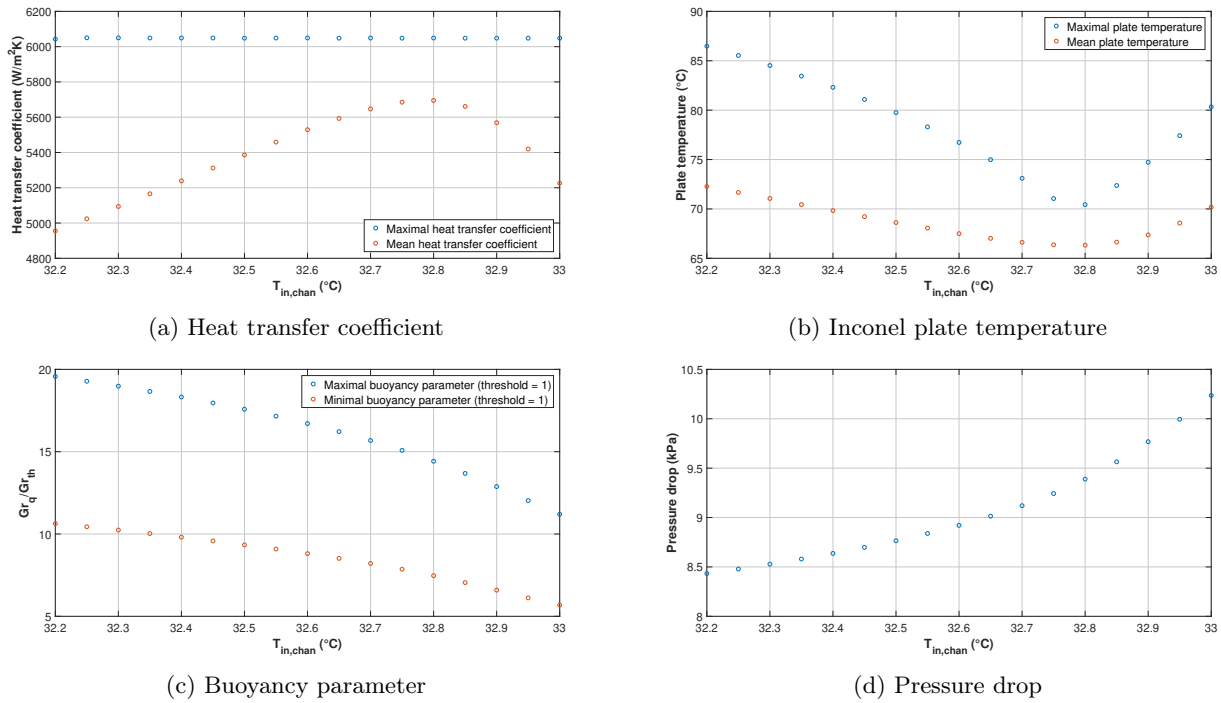
Figure 4.9: Analysis of the effect of a different inlet temperature with the other parameters constant ($G = 500$ kg/m^{2}s, $q'' = 19.8$ W/cm^2, $P_R = 1.0468$ and $T_{PC} = 33.05$°C)

drop is therefore higher.
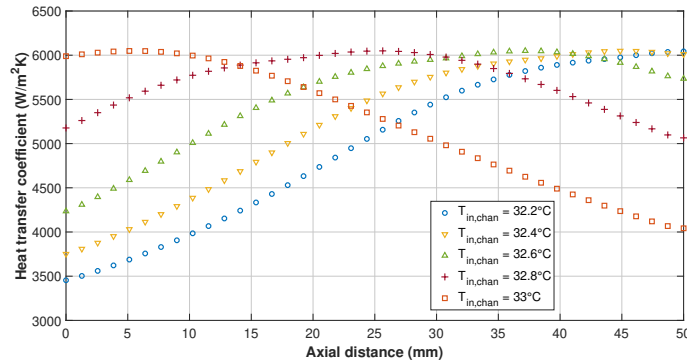
Figure 4.10: Model prediction of the evolution of the heat transfer coefficient along the axis with different inlet temperatures ($G = 500$ kg/m^{2}s, $q'' = 19.8$ W/cm^2, $P_R = 1.0468$ and $T_{PC} = 33.05$°C)

In conclusion, even if the inlet temperature does not impact the maximal value of the heat transfer coefficient (if the pseudo-critical temperature is already reached in the channel), it is possible to optimize it once the heat flux and the mass flux are fixed to reduce the overall temperature of the plate. Its impact over the pressure drop is not too important considering the 15% increase of the mean heat transfer coefficient over the whole heat exchanger (from 4956 to 5695 W/m^{2}K) and the reduction of the mean and maximal temperature of the plate (respectively 6°C and 16°C) with a variation between 32.2°C and 32.8°C for the inlet temperature. It is therefore really important to manage it to keep the pseudo-critical point inside the heat exchanger at all time and as close as possible to the middle of the heat exchanger.

4.4.2 Effect of the heat flux

The second parameter to be studied is the heat flux. The heat flux is the only parameter that is impossible to control as in a real application, the heat flux will come from the 'outside' and the goal of the cooling system is to manage it. It is therefore important to analyse the response of the system to different heat flux with the other parameters constant.

In the experimental study in section 2.2.8, the observations are that an increase in heat flux leads to a decrease in the heat transfer coefficient and a general increase of the plate temperature. Moreover, it impacted significantly the buoyancy with a very high value of the parameter at the inlet for the higher heat fluxes. However, the parameter decreases faster with a higher heat flux as the density gradient across the boundary condition decreases fast with an increasing bulk fluid temperature. The last observation was that the pressure drop would slightly increase with the heat flux but less compared to the effect of the inlet temperature or the effect of the mass flux.

The different results obtained by the predictive model can be observed in Fig. 4.11 with a heat flux varying between 15.26 and 27.5 W/cm^2. The other parameters are fixed with a mass flux of 500 kg/m^{2}s, an inlet temperature of 32.5°C and a reduced pressure of 1.0468 leading to a pseudo-critical temperature of 33.05°C.

(a) Heat transfer coefficient

(b) Inconel plate temperature

(c) Buoyancy parameter

(d) Pressure drop

Figure 4.11: Analysis of the effect of a different heat flux with the other parameters constant ($G = 500$ kg/m^{2}s, $T_{inlet,chan} = 32.5$°C, $P_R = 1.0468$ and $T_{PC} = 33.05$°C)

It can be seen that the different observations made in the experimental part are also predicted by the model. Indeed, all the results are perfectly in line with the experimental part. The evolution of the heat transfer coefficient in Fig. 4.11a shows a decrease of more than 20% (from 5840 to 4476 W/m^{2}K) of the mean value of the heat transfer coefficient between the two extreme heat fluxes. This decrease could be even higher if the inlet temperature was optimized (while keeping the mass flux constant). Indeed, the evolution of the heat transfer coefficient along the channel for different heat flux, displayed in Fig. 4.12, shows that for the lowest heat flux the peak is not even reached at the end of the channel. If the test with the 15.26 W/cm^2 was done with a higher inlet temperature its mean heat transfer coefficient would be higher and considering that the peak in the green curve happens close to the center (showing a good inlet temperature), the decrease of the heat transfer coefficient could become a 30% decrease. This decrease is in line with what could be observed in the experimental data. This graph also shows that with the same inlet temperature, the heat transfer coefficient of the test with the highest heat flux is always lower than the other tests even if it reaches its peak first (ie. the curves never cross each other).

As expected, the temperature of the plate (shown in Fig. 4.11b) increases with the heat flux with a mean

Figure 4.12: Model prediction of the evolution of the heat transfer coefficient along the axis with different heat fluxes ($G = 500$ kg/m^{2}s, $T_{inlet,chan} = 32.5$°C, $P_R = 1.0468$ and $T_{PC} = 33.05$°C)

temperature nearly twice as high for the highest heat flux (27.5 W/cm^2) than for the lowest heat flux (15.26 W/cm^2). The maximal value of the buoyancy parameters also increases significantly with the heat flux while the minimal value stays nearly constant showing a faster decrease for higher heat fluxes. Finally, the pressure drop increases but only slightly. As for the case of the inlet temperature, this difference comes from the higher temperature of the fluid subject to the higher heat fluxes. This higher temperature means that the bulk fluid is at a lower density leading to an acceleration of the fluid and an increase of the pressure drop.

In conclusion, the heat flux always has a negative effect over the performance of the heat exchanger. The heat transfer coefficient always decreases and the plate temperature increases. As it is impossible to control it, it is important to optimize the other parameters to respond to the deterioration of the heat transfer caused by a higher heat flux.

4.4.3 Effect of the mass flux

The last parameter to be studied is the mass flux. The experiment results showed that increasing the mass flux leads to higher heat transfer coefficients at the cost of higher pressure drops. The mass flux also reduces the plate temperature as well as the effect of the buoyancy.

The results of the model showing the effect of the mass flux are displayed in Fig. 4.13. The mass flux is varying from 400 to 700 kg/m^{2}s while the other parameters are fixed with the inlet temperature of the channel at 32.5°C, a heat flux of 22.89 W/cm^2 and a reduced pressure of 1.0468 (leading to a pseudo-critical temperature of 33.05°C). As for the effect of the heat flux in the previous section, the results of the model are in line with the observations of the experimental study.

The evolution of the heat transfer coefficient in Fig. 4.13a shows a nearly proportional evolution with the mass flux. The mean value of the heat transfer coefficient with a mass flux of 400 kg/m^{2}s is 3690 W/m^{2}K while it is 7280 W/m^{2}K for a mass flux of 700 kg/m^{2}s. Therefore an increase of 75% in mass flux results in a nearly 100% increase in the mean transfer coefficient. This results is comparable to the 50% increase of the heat transfer coefficient when the mass flux increases by 40% in the experimental study. This increase would effectively become more than 100% if the inlet temperature was optimized for the higher heat flux. Indeed as shown in Fig. 4.14, the case with the mass flux of 700 kg/m^{2}s does not its its peak before the end of the channel. This shows that the mass flux has indeed the opposite effect of the heat flux. A higher mass flux causes the peak to be reached later at a higher value while a higher heat flux causes the peak to happen sooner and at a lower maximal value.

With the heat transfer enhanced by the mass flux, the temperature of the plate is decreasing when the mass flux increases as displayed in Fig. 4.13b. The buoyancy parameter is also reduced significantly when the mass flux increases. Indeed, a 50% increase in mass flux (from 400 to 600 kg/m^{2}s) leads to the buoyancy parameter value being divided by more than two. This confirms that the mass flux is the easiest way to improve the heat transfer and to reduce the temperature of the surface. However, this improvement comes at the cost of a higher pressure drop. The pressure drop increase is nearly quadratic as it goes from 6.38kPa to 15.66kPa (145%) when the mass flux increases by 75%.

(a) Heat transfer coefficient

(b) Inconel plate temperature

(c) Buoyancy parameter

(d) Pressure drop
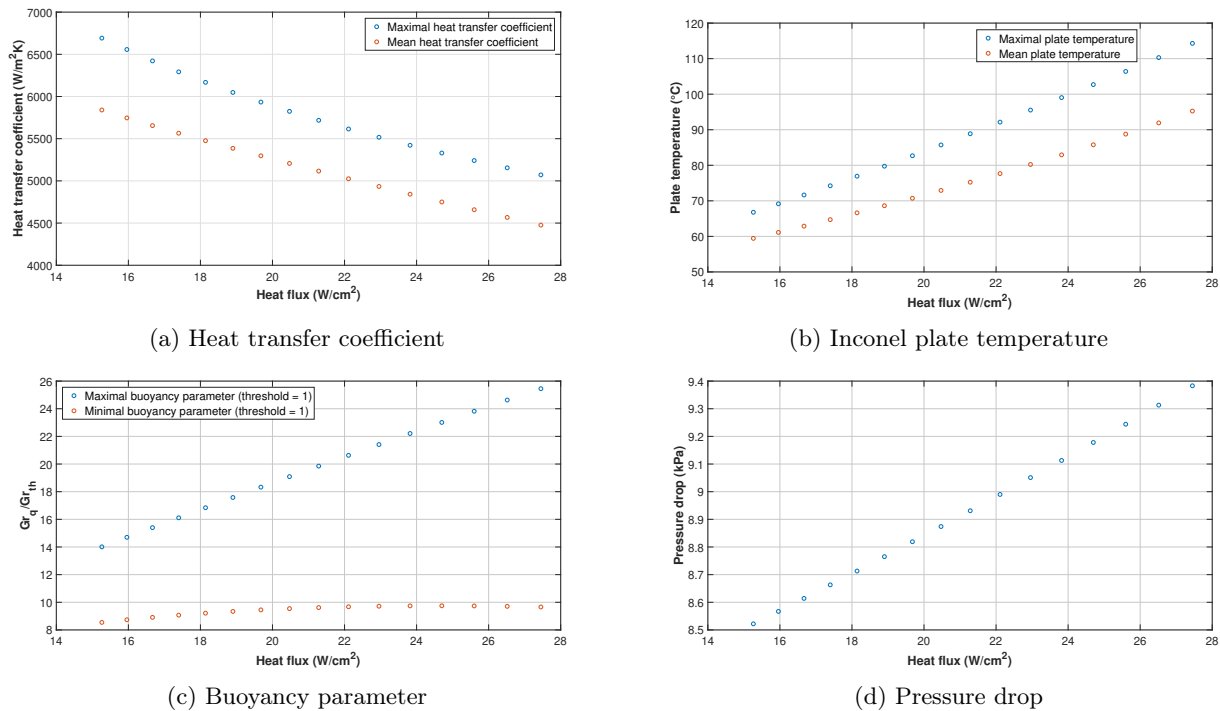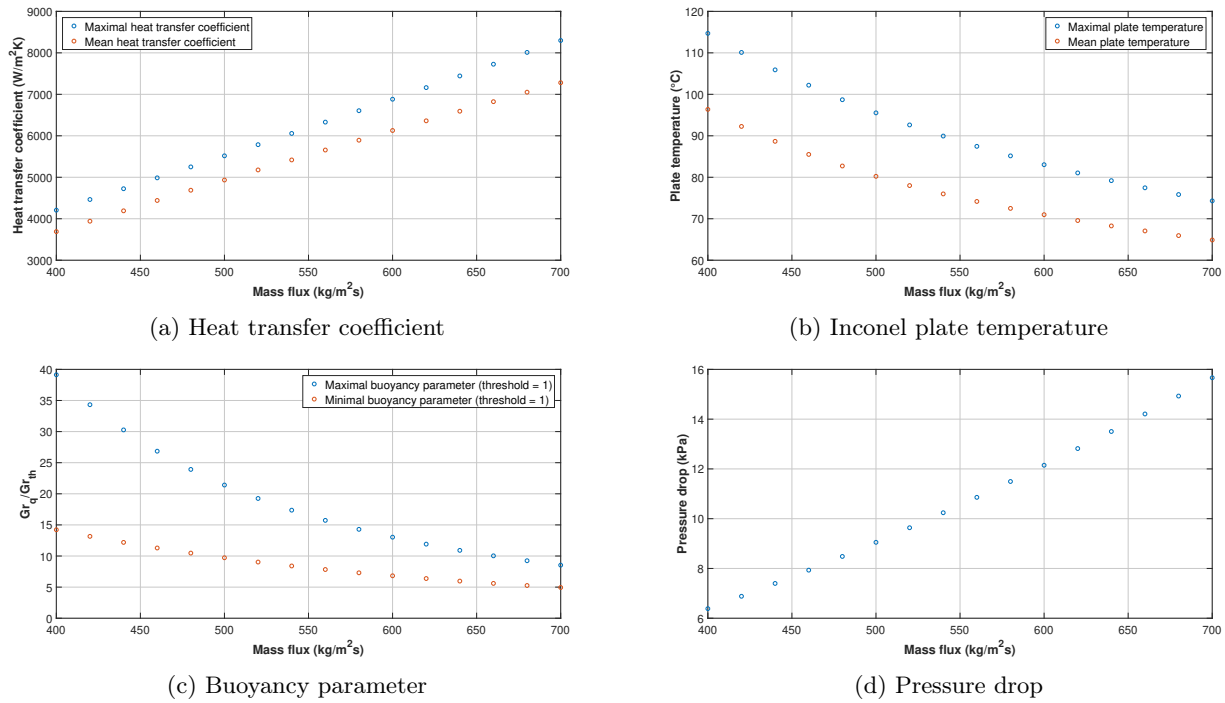
Figure 4.13: Analysis of the effect of a different mass flux with the other parameters constant ($T_{inlet,chan} = 32.5°C$, $q'' = 22.89$ W/cm^2, $P_R = 1.0468$ and $T_{PC} = 33.05°C$)

In conclusion, increasing the mass flux is the most effective way to increase easily the heat transfer coefficient, as can be observed in other heat exchanger. However, it comes at the cost of a large increase in the pressure drop meaning an increase of the work to provide at the pump. Therefore, in a real application only managing the mass flux is not the most effective way to do it. Indeed, the combined control of the mass flux and the inlet temperature to keep the pseudo-critical point inside the heat-exchanger is the best way to ensure a lower pressure drop and therefore a lower work at the pump while keeping a high heat transfer coefficient.

4.4.4   Particular case

Following the analysis of the impact of the different parameters, it is possible to look at a couple of particular cases. The first one is a test with a low mass flux and a high heat flux. This test is done to determine the point where the acceleration would start to deteriorate the heat transfer. In the experimental part in section 2.2.11, one of the two tests presented was done using a lower mass flux of 350 kg/m^{2}s to try to observe that. However, with the risk of melting the Torlon plastic, the mass flux could not be decreased enough. Therefore, the model is used to see if this phenomenon could occur in a realistic state of operation.

The second case is a test with a relatively low heat flux which is comparable to the heat produced by some actual processors (40-50 kW/m^2 according to [11] leading to around 10 W/cm^2 in the model considering the heat produced in the sides walls and edges). This test is done to see the kind of results that could be observed if the test section was an actual processor to cool down.

The results for the first case are displayed in Fig. 4.15. Fig. 4.15a shows the evolution of buoyancy parameter and of the acceleration parameter. As the goal was to have a test with an acceleration parameter above its threshold value, its value at the starts reaches $1.04*10^{-6}$. This value indicated an impact by the acceleration but still remains far from the second threshold value of $2\text{-}3*10^{-6}$ indicating the laminarization of the boundary layer. Moreover, the value decreases rapidly and after half of the channel, the parameter gets below the threshold value as the bulk fluid temperature increases past its pseudo-critical temperature (as shown in Fig. 4.15d). Considering the setting of the test with a really low mass flux of 350 kg/m^{2}s and the high heat flux of 23.1 W/cm^2, it is highly improbable to ever see a laminarization caused by the acceleration with this kind of test. Looking at the buoyancy in the same picture, its evolution follows what could be observed in the previous results with a large value at the start followed
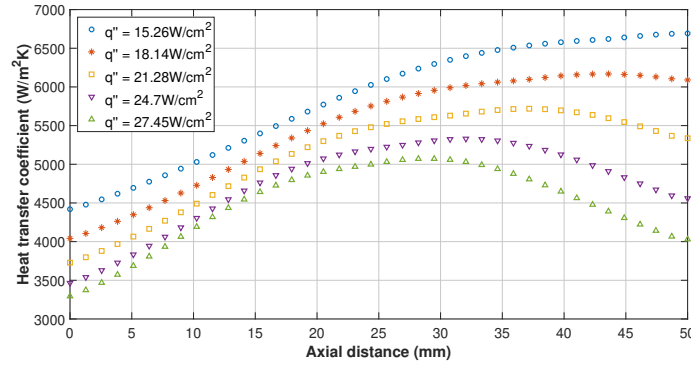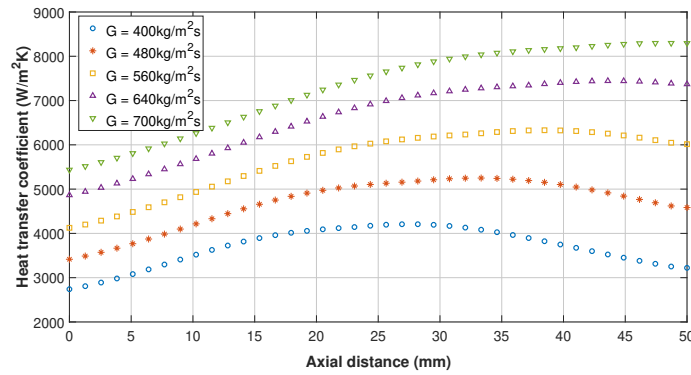
Figure 4.14: Model prediction of the evolution of the heat transfer coefficient along the axis with different mass fluxes ($T_{inlet,chan} = 32.5°C$, $q'' = 22.89$ W/cm^2, $P_R = 1.0468$ and $T_{PC} = 33.05°C$)

by a fast decrease along the channel with the density gradient decreasing across the channel.

The two other evolution shown in Fig. 4.15b and 4.15c are the heat transfer coefficient and the plate temperature. The first one shows a peak in the middle (as the inlet temperature was optimized) but with low values all along the channel as the maximum heat transfer coefficient is lower than 4000 W/m^{2}K due to the very large temperature gradient across the boundary layer and the large heat flux. The plate temperature shows two really high temperatures at the start and the end of the channel where the heat transfer coefficient is at its minimum. With the plate temperature as high as 130°C, the temperature predicted below the edges of the heat exchanger reached values as high as 210°C. This shows that this test could not be performed experimentally as it would results in the melting of the Torlon plastic and the degradation of the test section.

(a) Buoyancy parameter

(b) Heat transfer coefficient

(c) Inconel plate temperature

(d) Carbon dioxide temperature
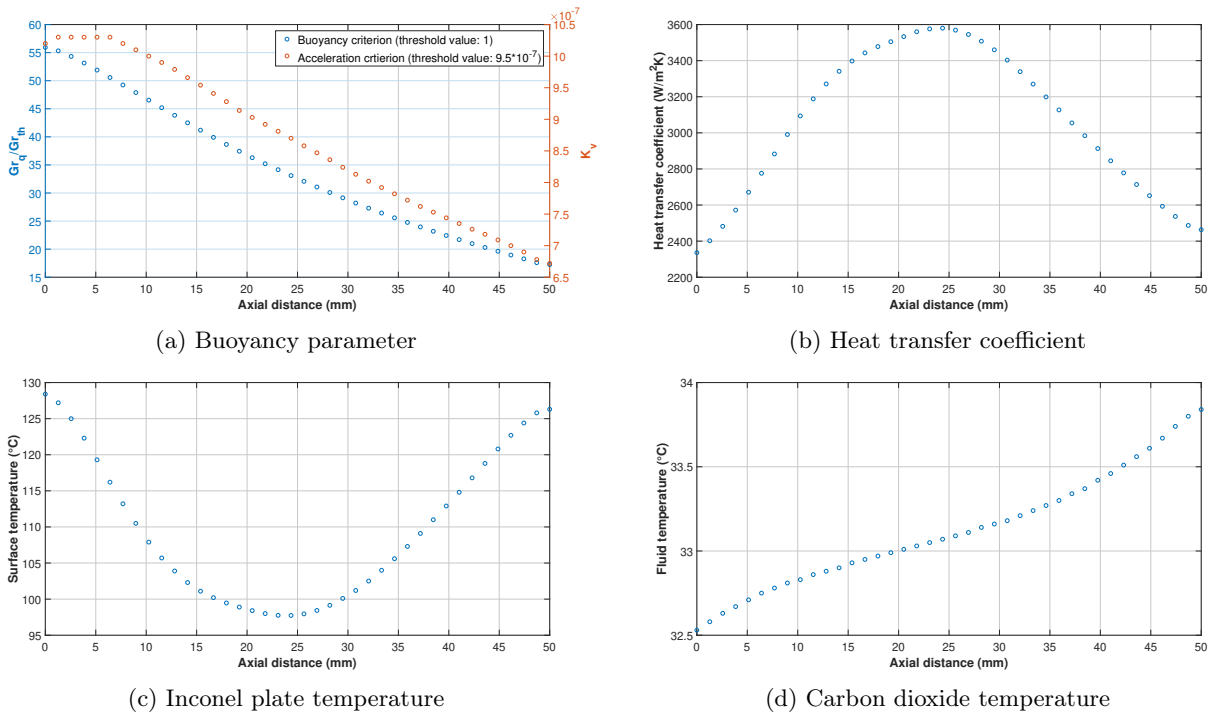
Figure 4.15: Analysis of a case impacted by the acceleration ($G = 350$ kg/m^{2}s, $T_{inlet,chan} = 32.5°C$, $q'' = 23.1$ W/cm^2, $P_R = 1.0468$ and $T_{PC} = 33.05°C$)

The results of the second test are displayed in Fig. 4.16. The heat flux is fixed at 10.3 W/cm^2 to be close to what could be observed in a real application. The mass flux was then set to 400 kg/m^{2}s to keep it as low as possible (to reduce the pressure drop, here equal to 6.24 kPa) while still respecting the maximal temperature

allowed by electronic component (100°C in this case). Finally the inlet temperature was set to 32.9°C to have the pseudo-critical temperature reached around the middle of the channel. This test is done under a reduced pressure of 1.0468 with a corresponding pseudo-critical temperature of 33.05°C.

The evolution of the heat transfer coefficient in Fig. 4.16a shows a peak around the middle of the channel as the pseudo-critical temperature is reached there. The maximum heat transfer reached is 6164 W/m^2K and the average is 5976 W/m^2K. This graph also shows that the slope after the critical point is steeper than before. This could already be observed in some of the previous tests but it is even clearer in this case. This is explained by the evolution of the properties of the carbon dioxide. Indeed, the thermal conductivity of the fluid in a 'vapor-like' state is much lower than in 'liquid-like' state leading to lower heat transfer coefficient after the pseudo-critical point.

The evolution of the Inconel plate temperature is shown in Fig. 4.16b. As can be seen, a large difference in temperature can be observed between the surface temperature in blue and the plate temperature below the edges. The difference with the side wall is lower than for the edges, the side walls are cooled down from both sides. It is important to take this difference into account when controlling the mass flux and inlet temperature to avoid an overheating in those parts. Indeed, in this case if the temperature controlled was the one below the channel and was heated up to 100°C, the temperature below the edges would be much higher than 100°C leading to a degradation of the electrical components. Finally, Fig. 4.16c shows that the acceleration has no effect over the heat transfer in this case even though the buoyancy is still present.

(a) Heat transfer coefficient

(b) Inconel plate temperature

(c) Buoyancy parameter
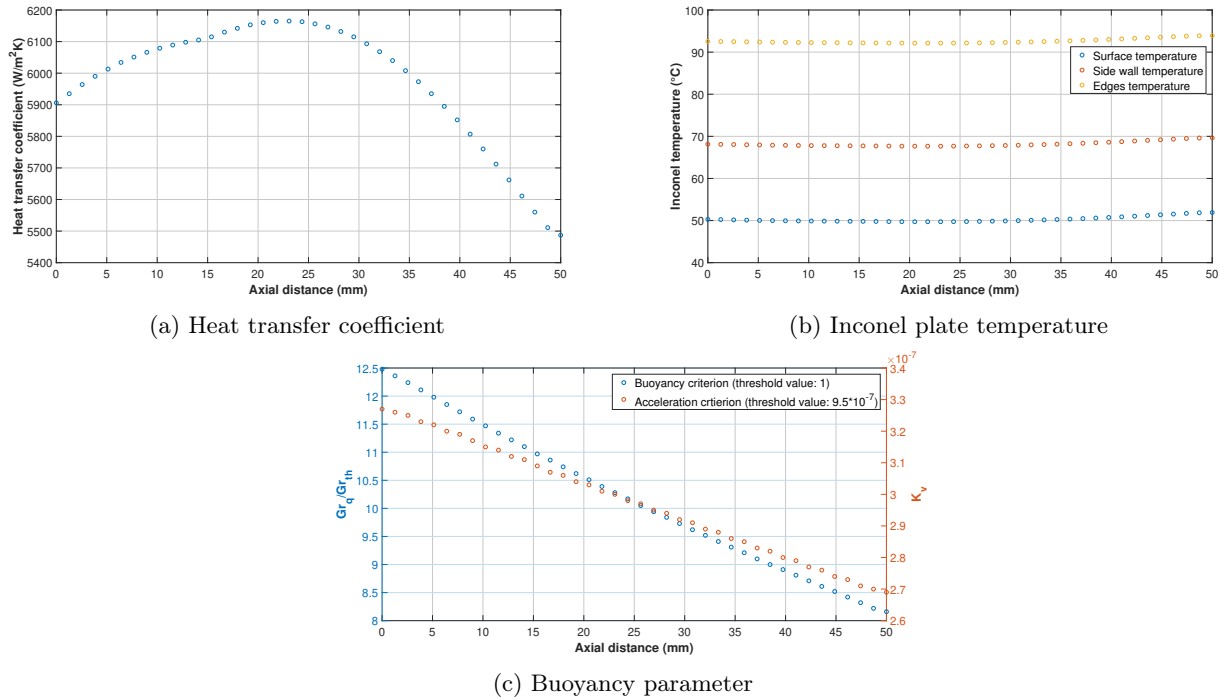
Figure 4.16: Analysis of a possible case in a real application ($G = 400$ kg/m²s, $T_{inlet,chan} = 32.9$°C, $q'' = 10.3$ W/cm², $P_R = 1.0468$ and $T_{PC} = 33.05$°C)

Both tests show that the chances are low to have a real application of electronics cooling with its heat transfer affected by the acceleration. Indeed, the maximum temperature allowed by the processor and other electronics is most of the time around 100°C. Therefore, the mass flux will never be decreased enough for the acceleration to affect the heat transfer. Moreover, due to the relatively small heat flux, the heat transfer coefficient can be high without a too high mass flux and therefore the work to provide at the pump is low as the pressure drop stays low.

In conclusion of this Chapter, the predictive model results are in good accordance with the experimental results with more than 87% of the test having a mean absolute percentage error below 20%. The results shows that the inlet temperature can be optimized by having the pseudo-critical point reached by the bulk fluid in the middle of the channel instead of close to one side. This optimization can result with an increase of the average heat transfer coefficient in the channel up to 15%. The heat flux is shown to decrease the overall performance of the

heat exchanger when increased. On the opposite, the mass flux greatly increases the heat transfer coefficient (up to 100% for a 70% increase of the mass flux) and reduces the plate temperature. However, it comes at the cost of a quadratic increase of the pressure drop. Finally, two particular tests show that in an actual application of electronics cooling, the acceleration should never affect the heat transfer and that a heat transfer coefficient of around 6000 W/m^{2}K can be reached with a limited mass flux and a relatively small pressure drop. With the steady-state model developed and the results analysed, it is possible to look at the second model treating the heat transfer in a transient regime.

Chapter 5

Model for the transient heat exchange

5.1 Principle

In this chapter, the theoretical model of the heat exchanger in transient condition is developed. Similarly to the steady-state model, the software used is the Engineering Equation Solver (EES) and the heat exchanger is represented using an electrical representation. The code can be found in Appendix A. The overview of the representation is shown in Fig. 5.1. The general principle is the same as for the steady-state system. The Inconel plate is divided in three different regions: one below the outer edge, one directly below the channel and one under the side wall. This division, across the channel, corresponds to the x-axis. The channel is then divided in 40 finite elements along the y-axis. The last axis is orthogonal to the Inconel plate and corresponds to the z-axis. The exchange between the plane and the fluid is happening along that direction. The same assumptions are also made, the Torlon plastic is assumed to be a perfect insulator, therefore all the heat produced in the Inconel plate goes to the fluid only through the bottom. The camera view port is also neglected as it affects only one of the three channel.
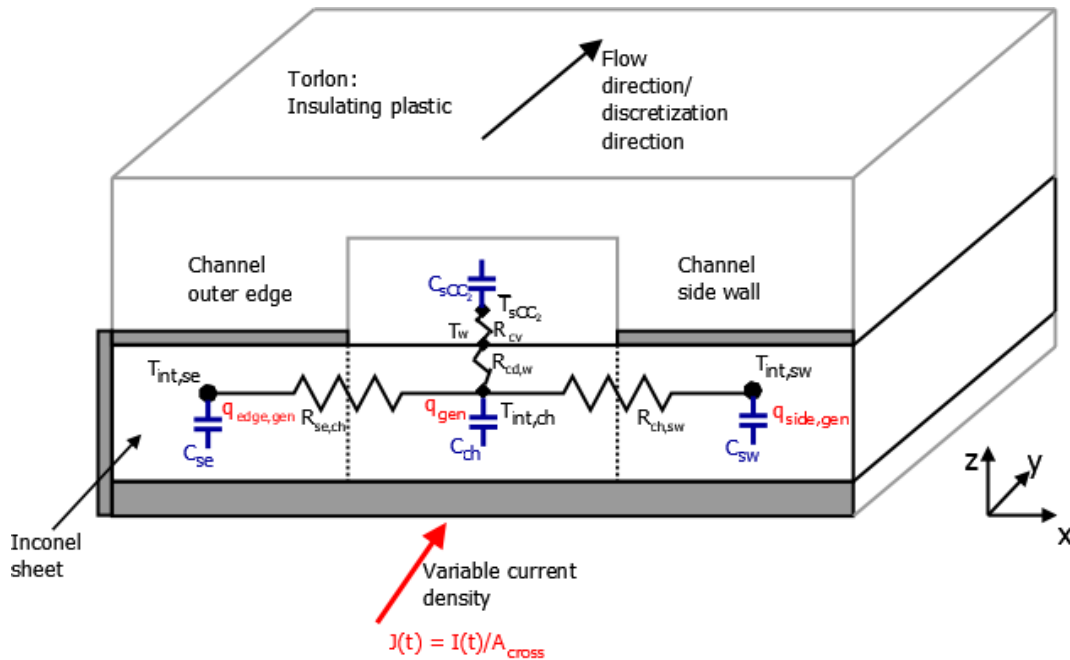
Figure 5.1: Scheme of the modelling of the heat exchanger in transient regime

The difference with the representation of the steady-state case is that all properties are time dependant. In the scheme, only the current is displayed as time dependant in order to avoid overcomplicating the scheme but

with the current varying (or the mass flux), the heat generated changes leading to a temperature change and all the properties are evolving. However, as the system does not converge instantly and present a thermal inertia, capacitors are added at the different nodes that were only defined by their temperature in the steady-state model. As the wall is an infinitesimal surface, it does not present any thermal inertia which explains why the node is still fully described by the temperature.

5.2 Description

An other global view of the model can be seen in Fig. 5.2 with the different inputs, outputs and parameters of the model. Compared to the model described in section 4.2, the parameters stay exactly the same and the different values of those ones are in Tab. 4.1. The outputs are also the same except for their dependence to time. Indeed, previously a single node was described by a single temperature. In a transient test, the node temperature is evolving in time and the whole evolution becomes an output. This is the same for the heat transfer coefficient, the pressure drop but also for the buoyancy and acceleration parameters that all change in time as well.

The biggest difference between the two models is in the input. Beside the four inputs present in steady-state (current, pressure, inlet temperature and mass flux), the initial temperature for all the different nodes is also an input. Indeed, the initial state must be described in order to have a 'starting' steady-state point before the thermal inertia starts to play its role. Th temperature parameter is chosen because it is the easiest way to describe a steady-state point. This implies that a first steady-state test must be performed with the initial state (current, mass flux, inlet temperature and pressure) in order to know those temperatures and avoid oscillations at the start.
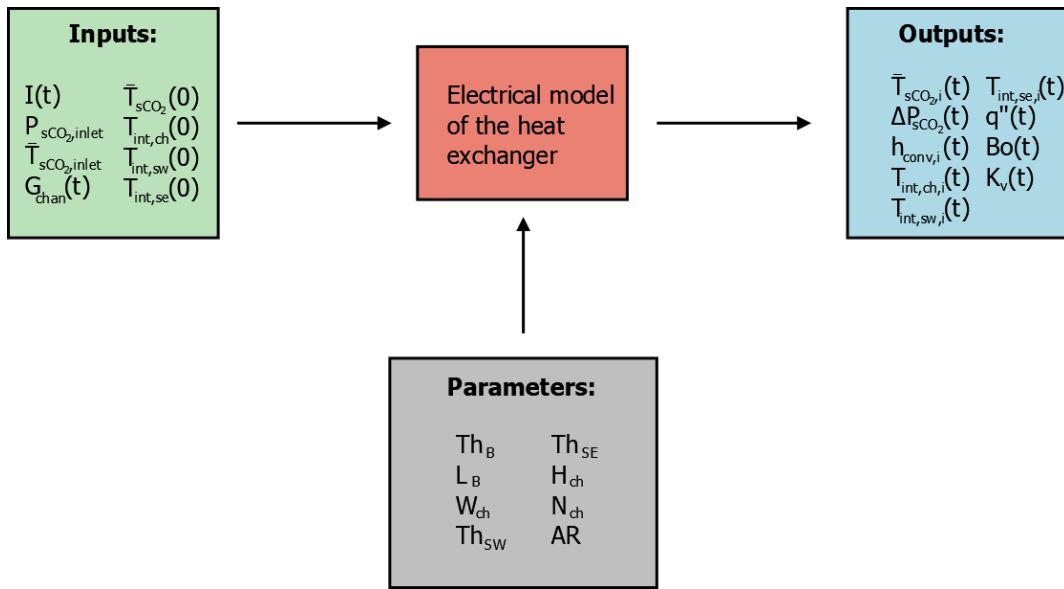
Figure 5.2: Input, output and parameters of the electrical representation of the heat exchanger in a transient case

Using the same method to represent the channel allows to keep the different equations from the steady-state model to compute the evolution of the properties (besides the temperature) of the fluid along the channel. The pressure is still assumed to be constant all along the channel and also stays constant in time. This simplification is done as the evolution of the pressure in time does not result of the heat exchanger alone but from the interaction of the whole loop. Some extensive tests would therefore be necessary to find a relation between the heat flux (or mass flux) variation and the pressure variation. However, by neglecting this, the long stabilisation after the first few seconds observed on the inlet and outlet temperature of the different tests (in Fig. 3.7, 3.10 and 3.13) will not occur. The pressure drop model is also remaining the same as well as the study of the buoyancy and the acceleration effects. Compared with the steady-state model, the difference occurs in the energy balance equations. Indeed, as the heat transfer is in a transient regime, the thermal inertia of the system needs to be considered. This is done using the heat capacity of the finite elements of the Inconel plate or the heat capacity rate of the fluid as described in section 1.2.1 and used in [35].

5.2.1 Evolution of the temperatures

With the temperatures becoming time dependent, the different equations had to change to take into account the inertia. The first equation to change is the evolution of the temperature of the carbon dioxide. Its new equation is as follows:

$$C_{sCO_2,i}\frac{\partial \bar{T}_{sCO_2,i}}{\partial t} = \dot{m}h_{i-1} + \frac{T_{w,i} - \bar{T}_{sCO_2,i}}{R_{conv}} - \dot{m}h_i \tag{5.1}$$

Comparing this equation to Eq. 4.2, a new term is present on the left part of the equal sign. It corresponds to the partial derivative in time of the temperature of the fluid at that specific node and the heat capacity of the fluid present at the node at that time described in Eq. 5.2. With both the specific heat capacity c_p and the density ρ evolving with the temperature, the heat capacity must be updated at every time and for every nodes. Looking at the sign of the terms present on the right hand side of the equation in Eq. 5.1, the terms corresponding to heat entering the node have a positive sign as they tend to increase the temperature in time. On the opposite, the term with heat leaving from the node have a negative sign. In this equation, the only 'negative' term is the flow leaving the node with its energy while both the fluid entering and the heat transfer with the wall have a positive sign. Concerning the evaluation of the resistance in convection, the same equations are used as in steady-state (developed in section 4.2.1). Moreover the Jackson and Hall correlation is used in order to compute the Nusselt number as it is the best correlation available as shown in section 4.2.6.

$$C_{sCO_2,i} = c_{p,sCO_2,i}L_{elem}W_{ch}H_{ch}\rho_{p,sCO_2,i} = c_{p,sCO_2,i}m_{p,sCO_2,i} \tag{5.2}$$

From there, the partial derivative in time of the fluid temperature is numerically integrated over each time step to determine the temperature difference between the time t and $t + dt$. With the temperature difference known, the new temperature is also known. The integral equation is as follows:

$$T(t + dt) - T(t) = \Delta T \approx \int_t^{t+dt} \frac{\partial T}{\partial t}dt \tag{5.3}$$

The new temperature at the node i at the time $t + dt$ is the new temperature used to compute the different fluid properties using the pressure (assumed constant) as the second independent property to fully describe the state of the fluid.

Concerning the evolution of the Inconel sheet, the same transformation is done to update the steady-state equation to a time dependent one. The first equation, described in Eq. 5.4, is the evolution of the temperature in time below the edges.

$$C_{int,se,i}\frac{\partial T_{int,se,i}}{\partial t} = q_{edge,gen,i} + \frac{T_{int,se,i-1} - T_{int,se,i}}{R_{ax,se,i-1}} - \left(\frac{T_{int,se,i} - T_{int,ch,i}}{R_{se,ch,i}} + \frac{T_{int,se,i} - T_{int,se,i+1}}{R_{ax,se,i}}\right) \tag{5.4}$$

Once more, on the right hand side of the equation, the different heat exchanges seen by the node (with the appropriate sign associated depending if the heat enters or leaves the node). Those exchanges include the heat generation by Joule effect inside the node and are computed using Eq. 5.5 where the electrical resistivity $\rho(t)$ becomes time dependant (as it evolves with the temperature) and the current density J potentially evolving in time as well. The same equation is used to compute the heat generation in the other part of the Inconel sheet with the cross section changing according to the geometry. The other exchanges are the same as in steady-state with three heat exchange in conduction. Namely the exchange with the previous node under the edge, the exchange with the node at the center below the channel and finally the exchange with the next node along the axis. The different resistances in conduction are computed using the same equation as in steady state (Eq. 4.6). On the left hand side of the equation, the heat capacity of the node appears with the partial derivative in time of the node temperature. The heat capacity is computed using the same equation as for the fluid in Eq. 5.2 applied to the geometry of the node (changing W_{ch} by Th_{se}) and using the Inconel properties (density and specific heat capacity).

$$q_{gen}(t) = (J(t)A_{cross})^2 R_e(t) \tag{5.5}$$

The same evolution from steady-state to transient can be observed with the additional heat capacity and partial derivative of the temperature in time in Eq. 5.6 for the nodes under the side wall and in Eq. 5.7 for the nodes under the channel. With the partial derivative in time of the temperature known across the Inconel sheet, the integral method in Eq. 5.3 is also used to compute the evolution of the different nodes constituting the Inconel sheet. Moreover, the Inconel is an incompressible solid, the temperature is enough to describe the state of the solid and to compute the different properties such as the thermal conductivity and the electrical resistivity used to calculate the resistance in conduction and the heat generated inside the plate by Joule effect.

$$C_{int,sw,i}\frac{\partial T_{int,sw,i}}{\partial t} = q_{side,gen,i} + \frac{T_{int,sw,i-1} - T_{int,sw,i}}{R_{ax,sw,i-1}} + \frac{T_{int,ch,i} - T_{int,sw,i}}{R_{ch,sw,i}} - \left(\frac{T_{int,sw,i} - T_{int,sw,i+1}}{R_{ax,sw,i}}\right) \tag{5.6}$$

$$C_{int,ch,i}\frac{\partial T_{int,ch,i}}{\partial t} = q_{ch,gen,i} + \frac{T_{int,ch,i-1} - T_{int,ch,i}}{R_{ax,ch,i-1}} + \frac{T_{int,se,i} - T_{int,ch,i}}{R_{se,ch,i}}$$
$$- \left(\frac{T_{int,ch,i} - T_{int,ch,i+1}}{R_{ax,ch,i}} + \frac{T_{int,ch,i} - T_{int,sw,i}}{R_{ch,sw,i}} + \frac{T_{int,ch,i} - T_{w,i}}{R_{ch,w,i}}\right) \tag{5.7}$$

The last node present in the representation of the heat exchange is the node of the wall in contact with the carbon dioxide. As the node represent an infinitesimal surface, the node does not present any thermal inertia (just like it does not see any heat generated). This assumption was further verified by looking at the Biot number as it was previously done in section 2.2.3 when the temperature measured by the camera was assumed equal to the surface temperature seen by the carbon dioxide. Once more, the Biot number was well under its threshold of 0.1. Considering this, the energy conservation at the node remains the same as in the steady-state case and is as follows:

$$\frac{T_{int,ch,i} - T_{w,i}}{R_{ch,w,i}} = \frac{T_{w,i} - T_{F,i}}{R_{conv,i}} \tag{5.8}$$

5.3   Model validation

As stated in [4], an easy way to validate a transient model is to compare its results to steady-state experimental data points as they are asymptotic solutions for the time dependant problems. Moreover, in this case, the results obtained in the steady-state are more reliable than the ones in transient due to the impossibility to fully adapt the setup, as explained in section 3.1.

Considering this, the two tests displayed in Fig. 5.3 are the two steady-state points presented in the analysis of a transient heat flux in section 3.2.4. The one with the lower heat flux is represented in Fig. 5.3a with the prediction given by the model. The MAPE results is 12.07% which is in line with the average result of the steady-state model. The case with the higher heat flux, displayed in Fig. 5.3b, fits even better with a higher precision and a mean absolute percentage error of only 6.82%.

Those two results show that the model can predict the results with a good accuracy. As the correlations used are the same as in the steady-state model, a test with all the partial derivative of temperature in time being equal to zero gives the same results as the steady-state model. Therefore this model shows the same precision as the one in steady-state. Due to the low number of experimental data points and the relatively low reliability of those data points, those points are not used to validate the model. Instead, the model predictions are compared to those in the following sections to see if the results match or not.

5.4   Model results

In this section, the model prediction for different transient tests (transient current or transient mass flux) are analysed. The predictions are compared to the experimental data points and therefore the parameters for the
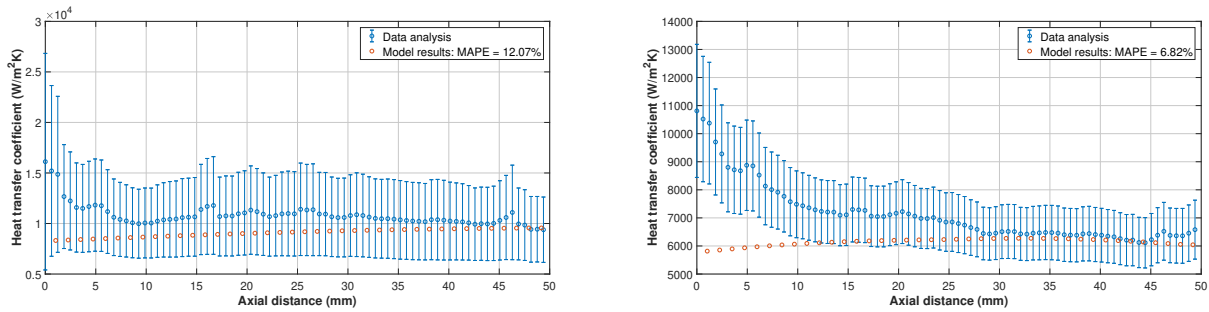
(a) $T_{inlet} = 32.6°C$, $T_{in,chan} = 32.63°C$, $T_{outlet} = 32.68°C$, $G = 4416.46$ kg/m^{2}s and $q'' = 2.19$ W/cm^2

(b) $T_{inlet} = 33°C$, $T_{in,chan} = 33.05°C$, $T_{outlet} = 33.3°C$, $G = 408.52$ kg/m^{2}s and $q'' = 4.37$ W/cm^2

Figure 5.3: Model validation with a comparison with two steady-state points

different tests are chosen close to the one of the corresponding experimental test. Once more, the heat flux indicated here is not the same as in the experimental part (but roughly the double). However, the current measured and used in the model to compute it was equal. After the comparison of the three cases with experimental data, a last transient test is studied. This last test is a step increase in current to see the response of the system to a sudden change.

5.4.1 Transient heat flux

In section 3.2.4, two transient heat fluxes are tested. The first one is an increase in the heat flux over a 5 second period. The observations were that the decrease in the heat transfer coefficient was delayed compared to the heat flux with even a small increase at the start. Moreover, the evolution in time along the channel was not smooth as some local peaks appeared in correspondence to some cold spots in the surface temperature. The mean plate temperature would increase relatively quickly with an asymptotic convergence at the end. Finally, the buoyancy parameter showed a linear increase with the heat flux.

The results of the predictive model are shown in Fig. 5.4. The first thing to note, looking at Fig. 5.4a, with the current increasing between 5 and 10s, the heat flux is not increasing perfectly linearly with it. The stable heat flux is reached only a couple second later than the end of the transient current. This is due to the impact of the electrical resistivity of the Inconel evolving with the temperature. Indeed, with the plate temperature increasing, the electrical resistivity increases slightly, increasing the heat generated for a given current. The low evolution of the electrical resistivity with the temperature was one of the reasons to choose the Inconel plate (as explained in section 2.1.1.1) to reduce this effect.

The evolution of the heat transfer coefficient, displayed in Fig. 5.4b, is showing no sign of a delay or of any increase that were observed in the experimental test. This delay can come from a larger inertia when all the system is considered (as the model only represent the channels). Moreover, the Torlon plastic is assumed to be a perfect insulator in the model therefore providing no inertia when in reality, the plastic is still heating up a bit creating a small heat capacity. More experimental test should be performed to see if the delay and the increases are recurrent or if it is caused by a data acquisition error. If the delay is seen to be recurrent, the model can be tuned by adding some additional thermal capacity that would lead to a higher inertia. Besides the delay, both the experimental analysis and the model show a sharp decrease and an asymptotic convergence. The model shows a decrease from 8333 W/m^{2}K to 6201 W/m^2 (in around 8 seconds for the model). The longer convergence of the experimental analysis is also due to the variation in the pressure and the inlet temperature assumed to be constant in the model.

In addition, both the evolution of the surface temperature and the buoyancy parameter are in line with the experimental observations. The surface temperature in Fig. 5.4c and the buoyancy parameter in Fig. 5.4d show a rapid increase and an asymptotic convergence at the end with a steady temperature reached around time equal to 15s. This stabilization at 15 seconds happens much sooner than in the experimental data as the model assumes a constant inlet temperature and a constant pressure which is not the case in the experimental measures. The change in the pressure and the inlet temperature is due to the whole system converging to a new steady-state point and the interaction of all the components of the loop.

(a) Heat flux

(b) Mean heat transfer coefficient

(c) Mean Inconel plate temperature

(d) Buoyancy parameter
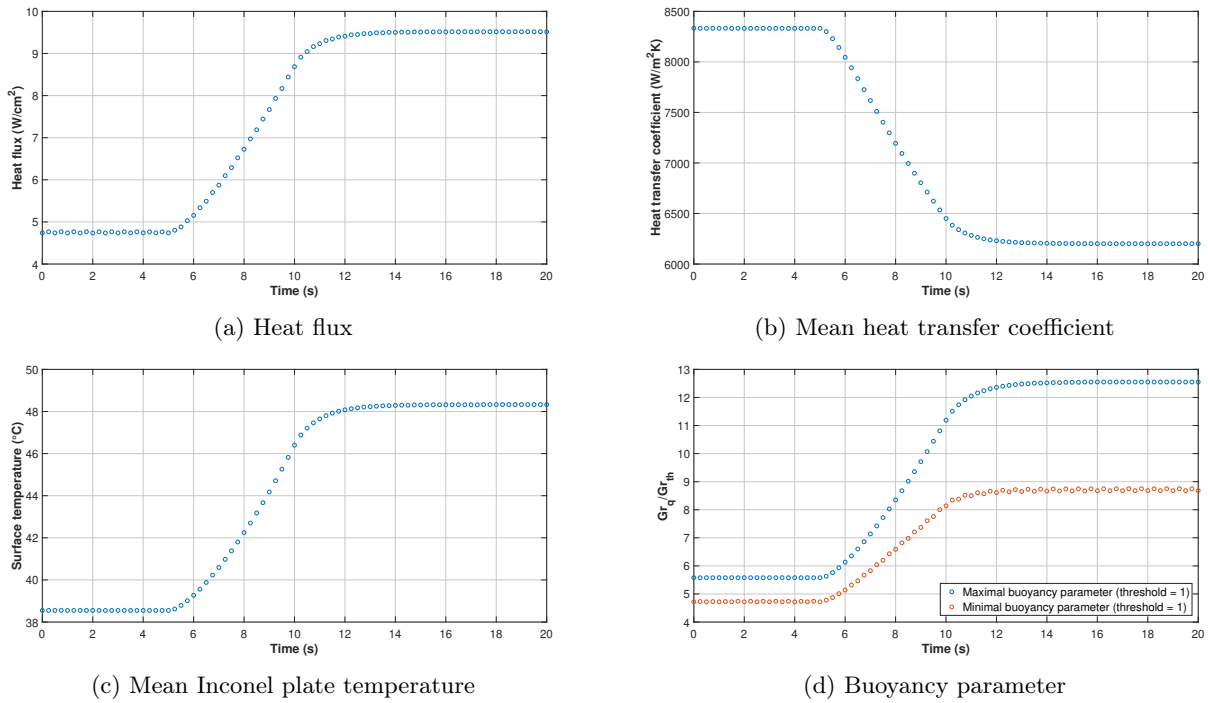
Figure 5.4: Analysis of the system under a transient current going from 25.2Amp to 35.6Amp in 5s ($G = 411.61$ kg/m^{2}s, $T_{inlet,chan} = 32.73$°C, $P_R = 1.0469$ and $T_{PC} = 33.05$°C)

Another observation made with the experimental results was the apparition of local peaks in the evolution of the heat transfer coefficient along the axis. However, the model is not predicting those local effects in Fig. 5.5. This difference could come from the model as the prediction of the local effect is a weakness of the 1D representation. Indeed, a CFD model in 3D is often necessary to simulate that kind of local phenomena. More experimental tests are needed to assess the presence of those local effects.
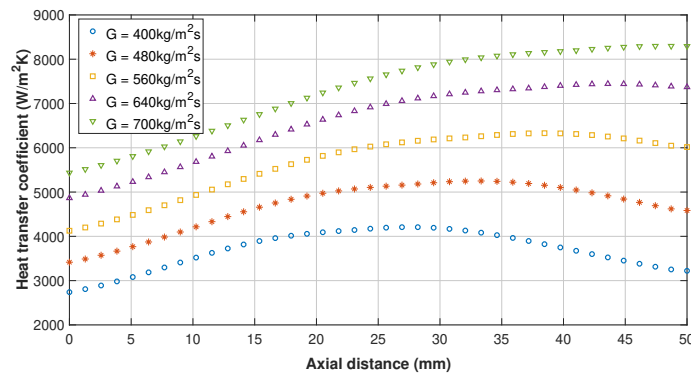
Figure 5.5: Model prediction of the evolution of the heat transfer coefficient along the axis at different times ($G = 411.61$ kg/m^{2}s, $T_{inlet,chan} = 32.73$°C, $P_R = 1.0468$ and $T_{PC} = 33.05$°C)

The second experimental test analysed was a test with the heat flux decreasing in time over a 5 seconds period. The results showed a large decrease in the heat transfer coefficient which is a strange results likely produced due to an error of the data acquisition as it is really different from the response to an increase in heat flux while the plate temperature and the buoyancy showed a pretty similar behavior between the two tests. Indeed, the plate temperature decreased rapidly with the heat flux decreasing and so did the buoyancy parameter.

The model simulated a decrease in current from 35.6Amp to 25.2Amp in 5 seconds starting after 5 seconds of steady-state. The mass flux is fixed at 414.13 kg/m^{2}s and the inlet temperature is equal to 33.05°C. The results

of the simulation are shown in Fig. 5.6. The first thing to note is that the small oscillations occurring during the first few seconds and notably for the buoyancy are due to a small imprecision in the guess values leading to the system trying to reach the true steady-state point. Other than that the response of the system is really similar to an increase in heat flux.

The heat flux (shown in Fig. 5.6a) shows the same evolution with an asymptotic convergence due to the evolution of the electrical resistivity of the Inconel plate with the temperature. The heat transfer coefficient evolution in Fig. 5.6b does not present any abrupt decrease as was observed in the experimental test. This shows that even if a delay and a small decrease are possible (just like the increase sees a delay and a small increase), the large decrease is most probably due to an error in the data acquisition. The prediction shows an asymptotic convergence of the heat transfer coefficient from 6040 to 8791 in around 8s. The starting and ending value of the mean heat transfer coefficient are different than the prediction for the increase in heat flux due to slightly different conditions such as the inlet temperature and mass flux. The two last results, namely the plate temperature in Fig. 5.6c and the buoyancy parameter in Fig. 5.6d, show a good concordance between the experimental data and the model prediction. Both see an asymptotic decrease to their new stable value. The stable value is also reached faster as the inlet temperature and the pressure are still considered constant.

(a) Heat flux

(b) Mean heat transfer coefficient

(c) Mean Inconel plate temperature

(d) Buoyancy parameter
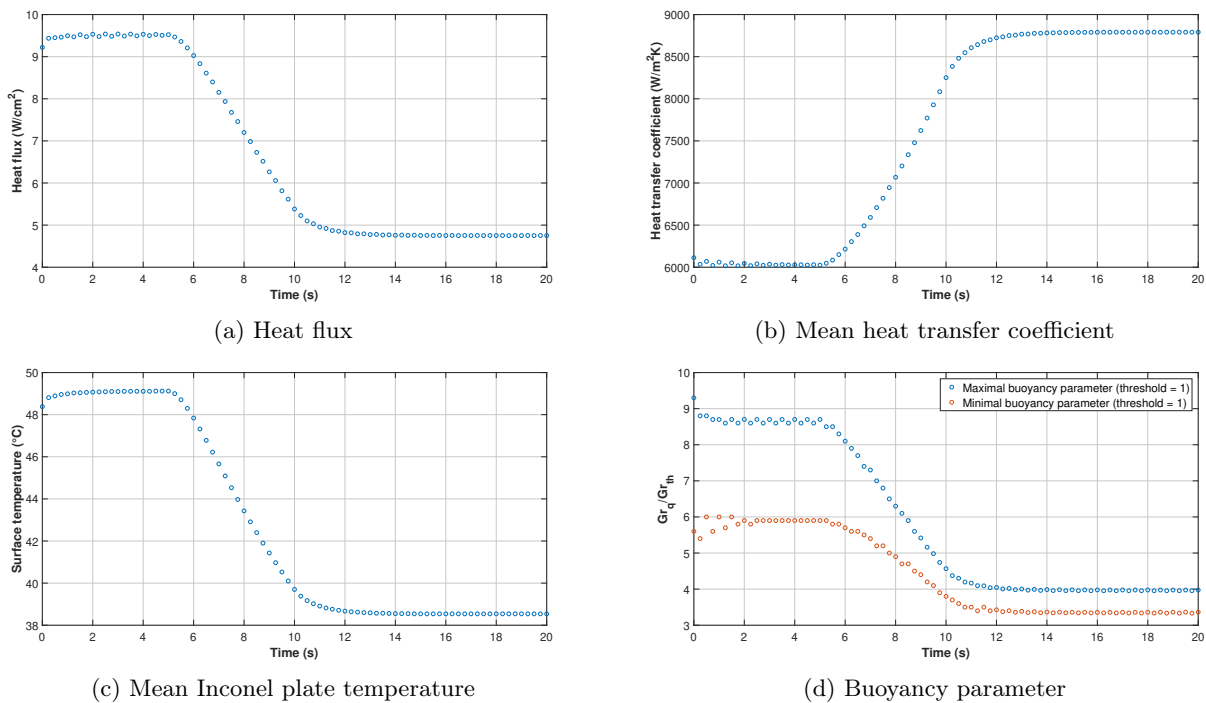
Figure 5.6: Analysis of the system under a transient current going from 35.6Amp to 25.2Amp in 5s ($G = 414.13$ kg/m²s, $T_{inlet,chan} = 33.05$°C, $P_R = 1.0469$ and $T_{PC} = 33.06$°C)

In conclusion, the model simulation predict the system to respond well to a progressive change in the heat flux with the plate temperature and the heat flux increasing nearly as fast as the heat flux. This is due to the low inertia of the system as the Inconel plate is really thin and the Torlon is assumed to be a perfect insulator and therefore provides no thermal inertia at all. The system shows no sign to a better response in the case of an increase or decrease of the heat flux. However, this impression is discussed in more detail in the test with the system subject to a current step change.

5.4.2   Transient mass flux

In this section, the prediction of the model for a transient mass flux is compared to the experimental test analysed in section 3.2.5. In both the experiment test and the model prediction, the mass flux goes from 490.29 kg/m²s to 578.7 kg/m²s over a period of 5 seconds. The experimental test showed a really fast convergence of the system to its new steady-state point and no local peak in the heat transfer coefficient along the channel was observed, the transition from one steady-state point to the other being really smooth.

The results of the model are displayed in Fig. 5.7, it is clear that those results are really close to what could be observed with the experimental test. Indeed, all the observations made are here verified with the mean heat transfer coefficient (in Fig. 5.7b) following nearly perfectly the increase of the mass flux in Fig. 5.7a. The Inconel mean plate temperature also shows a nearly linear decrease in Fig. 5.7c. Finally, with the mass flux increasing, the buoyancy parameter decreases all along the channel as shown in Fig. 5.7d.

(a) Heat flux

(b) Mean heat transfer coefficient

(c) Mean Inconel plate temperature

(d) Buoyancy parameter
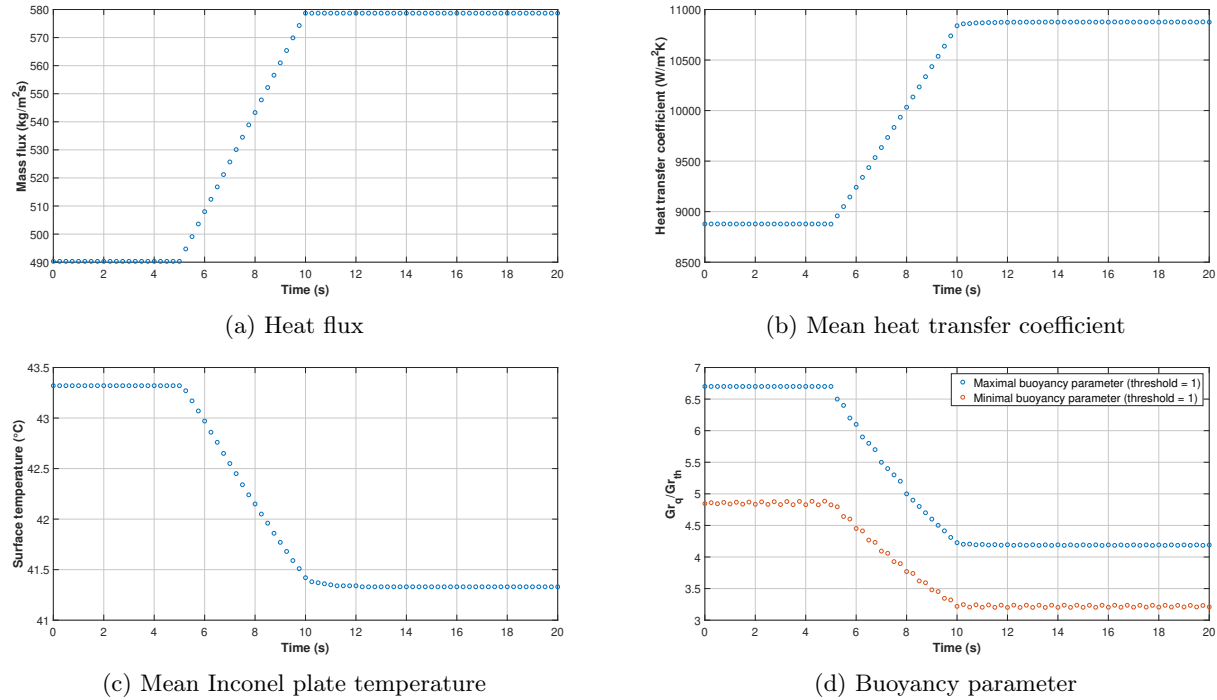
Figure 5.7: Analysis of the system under a transient mass flux going from 490.29 kg/m^{2}s to 578.7 kg/m^{2}s in 5s ($T_{inlet,chan} = 32.51$°C, $P_R = 1.038$ and $T_{PC} = 32.66$°C)

In conclusion, the response of the system to a mass flux variation is very quick as the convergence is not asymptotic. These results show that in a real application it will be possible to rapidly decrease the surface temperature if the heat flux increase by increasing the mass flux.

5.4.3 Step variation of the current

In this last section, the response of the system to a faster change in the heat flux is analysed. The parameters are taken equal to the one of the transient test with the increase in heat flux in Fig. 5.4. However, instead of an increase of the current over 5 seconds the current is increased in a single step at t=5s. The results of the test are displayed in Fig. 5.8.

Once more, due to the evolution of the electrical resistivity with regard to the temperature, the heat flux is not increased in a single step but is doubled in around 3 seconds and finally stabilizes after 5 seconds as shown in Fig. 5.8a. The increase is therefore twice as fast as the test with an increase of the heat flux in 5 seconds.

Looking at the response of the system with the evolution of the mean heat transfer coefficient in Fig. 5.8b, the convergence is really fast with no overshoot or oscillation observed. Moreover, the same starting and ending value of the mean heat transfer coefficient are observed here and in Fig. 5.4b. Therefore, in a real application no significant oscillation should occur at the macro-scale level. However, more experimental tests should be done to see if local phenomena (as observed in Fig. 3.6a) are indeed recurrent or just subject to the limitation of this test setup.

Finally, the same test was performed with a step decrease in the current to compare the response of the system in two opposite situation. The parameters are the same as in Fig. 5.6. The step change from 35.6Amp to 25.2Amp is happening at t=5s as well.
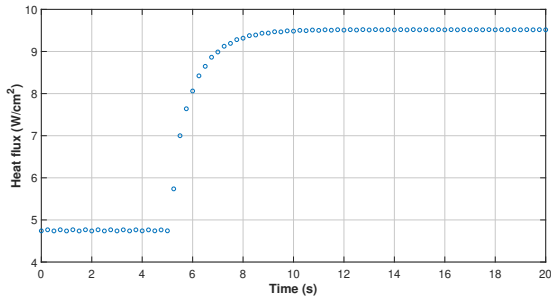
(a) Heat flux
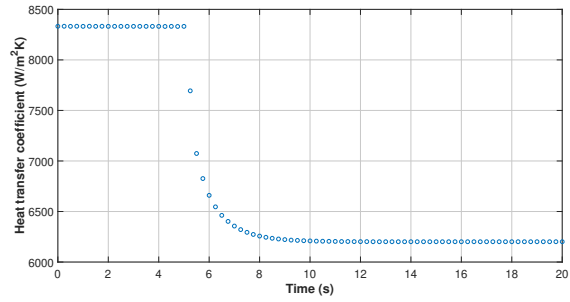
(b) Mean heat transfer coefficient

Figure 5.8: Analysis of the system under a step increase in the current going from 25.2Amp to 35.6Amp at t=5s ($G = 411.61$ kg/m^{2}s, $T_{inlet,chan} = 32.73$°C, $P_R = 1.0469$ and $T_{PC} = 33.05$°C)

The results are shown in Fig. 5.9. The response to a step decrease is similar to a step increase with a very fast decrease of the heat flux (in Fig. 5.9) and the corresponding increase in the mean heat transfer coefficient (in Fig. 5.9b). Both step increase/decrease tests show changes at the same speed and none show oscillation or a slower convergence.
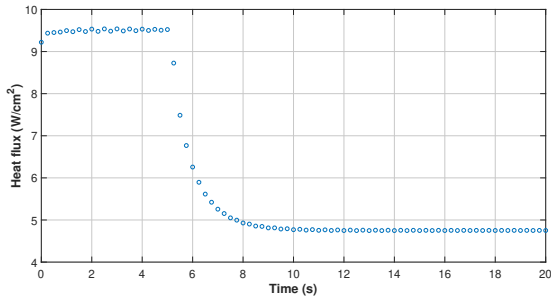
(a) Heat flux
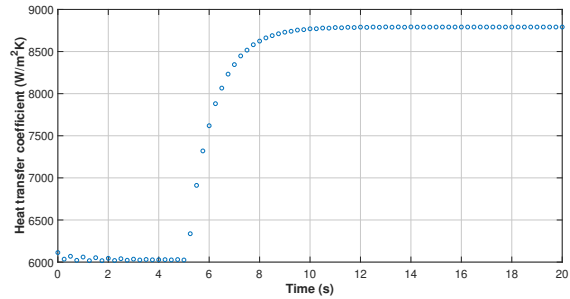
(b) Mean heat transfer coefficient

Figure 5.9: Analysis of the system under a step decrease in the current going from 35.6Amp to 25.2Amp in 5s ($G = 414.13$ kg/m^{2}s, $T_{inlet,chan} = 33.05$°C, $P_R = 1.0469$ and $T_{PC} = 33.06$°C)

In conclusion of this Chapter, due to the very low thermal inertia of the system, its response to a change in the heat flux of the mass flux is very fast and seems to present no oscillation. However, more experimental testing is needed to draw a conclusion. Moreover, some local phenomena seem to occur in the experimental data when varying the heat flux but are not present in the simulation. If they were to be recurrent and significant in more experimental testing, an other approach than the 1D representation would be necessary to determine where some hot spots could occur.

Chapter 6

Conclusion and perspectives

6.1 Conclusion

Throughout this study the performance of a microchannel based heat exchanger using supercritical carbon dioxide was studied. More particularly this work looks at the heat transfer of supercritical carbon dioxide close to its pseudo-critical point, in a turbulent regime and subject to an asymmetric heat flux boundary condition. Due to the increasing compactness of electronics device, new technologies are looked at as the heat flux is ever increasing while the maximum allowed temperature remains the same. In that context, some cooling systems used today could become obsolete due to the to high heat load. The use of supercritical carbon dioxide might be an alternative to the traditional air or water cooling widely used today. This raises the following question: "Is a microchannel-based heat exchanger using supercritical carbon dioxide well suited to cool down electronics devices?".

To answer this question, an experimental setup as well as a microchannel-based heat exchanger modeling were investigated in parallel in steady-state and transient conditions. Chapters 2 and 3 describe the experimental setup and analyse the recorded results. Then, an electrical representation of the heat exchanger in steady-state is developed in Chapter 4. This model is finally modified in Chapter 5 to be able to simulate some transient tests.

Th experimental study is divided in two distinct parts. In Chapter 2, the heat exchanger is tested under steady-state conditions. The aim of this part is to look at the influence of the different parameters such as the heat flux, the mass flux and the inlet temperature over the heat transfer. The tests looked at the influence of the different parameters over the plate temperature measured with an IR camera and the heat transfer coefficient computed with an analysis of the plate temperature, the knowledge of the heat flux produced by Joule effect and the knowledge of the inlet temperature of the carbon dioxide. Another main point of interest was the buoyancy and the acceleration effects both resulting from the density gradient (across the boundary layer or along the axis). The former one is shown to be present in most cases. However, the acceleration is negligible in all the conditions tested experimentally. Its effect only appears in extreme cases of high heat flux and low mass flux, leading to too high temperatures for the security of the test setup. The inlet temperature main effect being the displacement of the pseudo-critical location inside the channel, its effect over the heat transfer coefficient and the plate temperature in the experimental results is not significant as long as the pseudo-critical point is reached inside the channel. This conclusion was favored by an enhancement of the heat transfer at the inlet of the channels leading to a large peak in the heat transfer coefficient sometimes hiding the position of the real heat transfer coefficient peak and changing the mean value of the heat transfer coefficient along the channel. This large increase also makes it impossible to determine with certainty the value of the heat transfer coefficient at its peak. However, an impact over the buoyancy is observed as a higher inlet temperature (closer to the pseudo-critical temperature) reduces the effect of the buoyancy. Despite the problem of the heat flux enhanced at the inlet, the effect of the heat flux and the mass flux are easy to analyse. The former one has a negative effect over all the results. The heat transfer coefficient is decreased all along the channel (by around 30% with the heat flux being doubled), the plate temperature is significantly increased and the buoyancy effect increases as well. The latter one has a positive impact over the results. With an increased mass flux, the plate temperature is lower and the heat transfer coefficient is much higher (around 50% higher when the mass flux is increased by 40%). Moreover the impact of the buoyancy is reduced. However, the positive impact

comes at the cost of a large pressure drop increase.

In Chapter 3, the approach is modified to perform transient tests. However, due to the limitation of time caused by the Covid-19 crisis, the test setup could not be adapted to optimize the data acquisition of transient tests. The number of experimental tests is also limited to only three different tests to look at the response of the system to a varying heat flux and a varying mass flux. The system showed a good response to an increasing heat flux with a small delay between the heat flux increase and the heat transfer coefficient decrease. The small delay was followed by a sharp decrease to converge to the new stable point. The plate temperature also shows a fast increase with some local cold spots along the channels. However the local phenomena could not be confirmed as no additional experimental test is available to support their existence. The results observed for a heat flux decrease are inconsistent with what could be expected. Indeed, the heat transfer coefficient is decreasing as long as the heat flux decreases where the result expected was the same kind of response than in the case of the heat flux increase with a delay follow by a fast increase in heat transfer coefficient. It is most probably due to some errors during the data acquisition as the plate temperature evolution decreases as soon as the heat flux decreases and nothing really explains that the heat transfer coefficient decreases. Finally, the response to a change in mass flux is shown to be really fast and with no oscillation or local peak as in the case of the transient heat flux. An other observation in all the tests is a long and slow convergence of the inlet and outlet temperature to their new stable values. This is due to the whole system adapting to the new heat flux or new mass flux and converging to the new stable point.

In Chapter 4, the heat exchanger is modeled using an electrical representation by replacing finite elements with nodes linked to one another by thermal resistances. Different correlations to compute the Nusselt number were tested with the experimental data points and the one with the lowest mean absolute percentage error (developed by Jackson and Hall) is used. This model predicts more than 87% or the experimental results with a mean absolute percentage error of less than 20%. With the model, the impact of the different parameters is studied and a couple of particular tests are also studied. The following observation can be pointed out:

- The inlet temperature actually plays a major role in the optimization of the heat transfer coefficient as its average (the peak not being impacted) can be increased by 15% between a case where the pseudo-critical temperature is reached by the bulk fluid at the very end of the channels and a case where it is reached in the middle. This optimization comes at a cost of a small pressure drop increase.

- The effects of the heat flux are in line with the experimental observations. The heat transfer coefficient is decreased by around 20% when the heat flux is doubled and the plate temperature increases significantly. The buoyancy is also heavily increased as the maximum reached value increases linearly with the heat flux.

- As seen with the experimental results, the model shows a high increase in the heat transfer coefficient with an increase in mass flux. A 75% increase in mass flux leads to an increase of around 100% in the average heat transfer coefficient over the whole channel and a 100% increase in its peak value. The plate temperature is therefore reduced and the decrease of the buoyancy parameter is quadratic. This comes however at the cost of a quadratic increase of the pressure drop.

- An extreme simulation with a low mass flux and a high heat flux shows that the acceleration effect will not occur in normal conditions of electronics device cooling. The temperature reached in some part of the exchanger are higher than 200°C which is much higher than what is supported by electronics device.

- A test with a realistic value of heat generated by an actual processor shows heat transfer coefficients as high as 6164 W/m^{2}K with an average of 5976 W/m^{2}K over the whole heat exchanger. Compared to the value obtained with the air (around 2-300W/m^{2}K) this is a significant improvement. those values are also at least as high as what could be observed with water while still presenting the safety advantage of the carbon dioxide (non corrosive and electrical insulator). The mass flux in this test is lowered as much as possible to reduce the pressure drop (equal to 6.24 kPa) while keeping the maximal temperature inside the heat exchanger below 100°C.

Finally, a model of the heat exchanger in transient condition is developed in Chapter 5. The electrical approach from the steady-state model is kept with the addition of thermal capacities to account for the thermal inertia. Due to the very limited number of transient tests, the model is not validated with transient tests. But using the same correlation as the steady-state model, it shows the same precision for steady state experimental tests that represent the asymptotic convergence points of time-dependant situations. The results of the model shows similar results to the experimental analysis for the mass flux variation with a very fast reaction and no oscillation. The model is

however not showing the delay in the response of the heat transfer coefficient when the heat flux increases. If the delay is confirmed by more experimental tests it is possible to tune the model by adding thermal capacity inducing a larger inertia in the response of the system. Another limitation of the model is the incapacity to detect any local phenomena. More experimental tests are therefore needed to asses the importance of those local effects and their impact over the response of the whole heat exchanger. Finally, the model shows the same time of convergence in an increase and a decrease in heat flux with no overshoot or oscillation in the case of a sudden change.

In conclusion, this work answers the initial question as the microchannel-based heat exchanger using super-critical carbon dioxide close to the critical point shows some promising results for the thermal management of electronic devices. With the really high heat transfer coefficients in the vicinity of its pseudo-critical point and its good response to transient heat flux and mass flux, the carbon dioxide could be well suited to extract the growing heat produced by more and more compact electronic devices. However, further research is needed especially in the response of the system to transient perturbations as the few results showed the apparition of some possible local phenomena that need to be confirmed and analysed in more detail to develop a model taking them into account.

6.2 Recommendations for future works

To conclude this work, some perspectives to improve both the experimental setup and the modeling are suggested.

6.2.1 Experimental setup

For the experimental setup, the first improvement would be to adapt the setup for the acquisition of transient experiments notably by the acquisition of the current in real time directly in LabView. A better data acquisition system could also be installed to increase the number of data points per second without decreasing the precision. Furthermore, the length of the channels could be increased to reduce the relative part of the channel impacted by the effects of the inlet of the channels.

After the modification of the system, more experimental points should be recorded in transient conditions. The presence of the local effects in the case of the increase in heat flux should be verified and their impact analysed if they are recurrent. The delay in the response should also be addressed to potentially improve the model with the addition of thermal capacities. Furthermore, a new test matrix should be used to look at the response of the system in transient regimes starting at different inlet temperatures, varying between two different heat fluxes and with different mass fluxes. Finally, the design of the test section could be inverted with only the top plate heated instead of the one at the bottom. This new design could help determine the real impact of the buoyancy locally but also at the exchanger scale with the global performance decrease in both steady-state and transient conditions.

6.2.2 Modeling

About the modeling several perspective can be suggested:

- A 3D CFD model could be developed to be able to predict the effect of the inlet over the heat exchange and therefore fit the results of the experimental study over the whole channel.

- The representation of the header region could be added to be able to use the data from the thermocouple for the inlet temperature.

- The transient model thermal inertia could be tuned with more experimental testing.

- Finally, if the local phenomena are shown to be recurrent and significant under transient conditions a CFD model could be developed to represent these phenomena.

Bibliography

[1] R. H. Sabersky and E. G. Hauptmann, "Forced convection heat transfer to carbon dioxide near the critical point," *International Journal of Heat and Mass Transfer*, vol. 10, no. 11, pp. 1499–1508, nov 1967.

[2] J. D. Jackson, "Fluid flow and convective heat transfer to fluids at supercritical pressure," *Nuclear Engineering and Design*, vol. 264, pp. 24–40, nov 2013.

[3] D. M. McEligot and J. D. Jackson, "Criteria for convective heat transfer in gas flow through non-circular ducts," *Nuclear Engineering and Design*, vol. 232, no. 3, pp. 327–333, aug 2004.

[4] J. Padet, "Transient convective heat transfer," *Journal of the Brazilian Society of Mechanical Sciences and Engineering*, vol. 27, no. 1, pp. 74–95, mar 2005.

[5] *TRICOR Coriolis Mass Flow Meters.*

[6] J. Stafford, E. Walsh, and V. Egan, "Characterizing convective heat transfer using infrared thermography and the heated-thin-foil technique," *Measurement Science and Technology*, vol. 20, no. 10, p. 105401, sep 2009.

[7] H. Ay, J. Jang, and J.-N. Yeh, "Local heat transfer measurements of plate finned-tube heat exchangers by infrared thermography," *International Journal of Heat and Mass Transfer*, vol. 45, no. 20, pp. 4069–4078, sep 2002.

[8] *Genesys - Programmable DC Power Supply.*

[9] J. D. Jackson, "Heat transfer deterioration in tubes caused by bulk flow acceleration due to thermal and frictional influences," *International Congress on Advances in Nuclear Power Plants 2012, ICAPP 2012*, vol. 1, pp. 223–230, 01 2012.

[10] T. Evans, *The Different Technologies for Cooling Data Centers*, Schneider Electric – Data Center Science Center.

[11] P. S. F. Intel® Xeon®, *Thermal mechanical specification and design guide*, Dec. 2019.

[12] C. B. Tibiriçá, L. E. Czelusniak, and G. Ribatski, "Critical heat flux in a 0.38mm microchannel and actions for suppression of flow boiling instabilities," *Experimental Thermal and Fluid Science*, vol. 67, pp. 48–56, oct 2015.

[13] B. M. Fronk and A. S. Rattner, "High-Flux Thermal Management With Supercritical Fluids," *Journal of Heat Transfer*, vol. 138, no. 12, aug 2016.

[14] O. C. da Rosa, F. G. Battisti, G. M. Hobold, and A. K. da Silva, "Enhancing heat rejection from electronic devices with a supercritical carbon dioxide minichannel heat exchanger," *International Journal of Refrigeration*, vol. 106, pp. 463–473, oct 2019.

[15] J. D. Jackson, "Models of heat transfer to fluids at supercritical pressure with influences of buoyancy and acceleration," *Applied Thermal Engineering*, vol. 124, pp. 1481–1491, sep 2017.

[16] V. Narayanan, B. M. Fronk, T. L'Estrange, and E. Rasouli, "Supercritical carbon dioxide solar thermal power generation - overview of the technology and microchannel receiver development," in *Energy, Environment, and Sustainability.* Springer Singapore, nov 2018, pp. 333–355.

[17] D. G. Randall, "Some heat transfer and fluid friction experiments with supercritical water," *Reactor heat transfer conference*, 1956.

[18] B. S. Shiralkar and P. Griffith, "Deterioration in heat transfer to fluids at supercritical pressure and high heat fluxes," *Journal of Heat Transfer*, vol. 91, no. 1, pp. 27–36, feb 1969.

[19] R. P. Bringer and J. M. Smith, "Heat transfer in the critical region," *AIChE Journal*, vol. 3, no. 1, pp. 49–55, mar 1957.

[20] Y.-Y. Hsu and J. M. Smith, "The effect of density variation on heat transfer in the critical region," *Journal of Heat Transfer*, vol. 83, no. 2, pp. 176–181, may 1961.

[21] R. D. Wood and J. M. Smith, "Heat transfer in the critical region—temperature and velocity profiles in turbulent flow," *AIChE Journal*, vol. 10, no. 2, pp. 180–186, mar 1964.

[22] E. G. Hauptmann, "An experimental investigation of forced convective heat transfer to a fluid in the region of its critical point," Ph.D. dissertation, 1966.

[23] J. D. Jackson, "Screening and correlating data on heat transfer to fluids at supercritical pressure," *Journal of Nuclear Engineering and Radiation Science*, vol. 2, no. 1, dec 2015.

[24] M. Bazargan, D. Fraser, and V. Chatoorgan, "Effect of buoyancy on heat transfer in supercritical water flow in a horizontal round tube," *Journal of Heat Transfer*, vol. 127, no. 8, pp. 897–902, mar 2005.

[25] B. W. Lance, J. R. Harris, and B. L. Smith, "Experimental validation benchmark data for computational fluid dynamics of mixed convection on a vertical flat plate," *Journal of Verification, Validation and Uncertainty Quantification*, vol. 1, no. 2, apr 2016.

[26] S. J. Kline, W. C. Reynolds, F. A. Schraub, and P. W. Runstadler, "The structure of turbulent boundary layers," *Journal of Fluid Mechanics*, vol. 30, no. 4, pp. 741–773, dec 1967.

[27] V. C. Patel and M. R. Head, "Reversion of turbulent to laminar flow," *Journal of Fluid Mechanics*, vol. 34, no. 2, pp. 371–392, nov 1968.

[28] S. A. Jajja, K. R. Zada, and B. M. Fronk, "Experimental investigation of supercritical carbon dioxide in horizontal microchannels with non-uniform heat flux boundary conditions," *International Journal of Heat and Mass Transfer*, vol. 130, pp. 304–319, mar 2019.

[29] S. A. Jajja, J. M. Sequeira, and B. M. Fronk, "Geometry and orientation effects in non-uniformly heated microchannel heat exchangers using supercritical carbon dioxide," *Experimental Thermal and Fluid Science*, vol. 112, p. 109979, apr 2020.

[30] T. Schulenberg and M. Raqué, "Transient heat transfer during depressurization from supercritical pressure," *International Journal of Heat and Mass Transfer*, vol. 79, pp. 233–240, dec 2014.

[31] K.-H. Kang and S.-H. Chang, "Experimental study on the heat transfer characteristics during the pressure transients under supercritical pressures," *International Journal of Heat and Mass Transfer*, vol. 52, no. 21-22, pp. 4946–4955, oct 2009.

[32] H. Li, Z. Hu, M. Zhao, H. Gu, and D. Lu, "Experimental investigation on transient heat transfer in 2×2 bundle during depressurization from supercritical pressure," *Annals of Nuclear Energy*, vol. 109, pp. 237–248, nov 2017.

[33] Q. Zhang, J. Cao, Q. Bi, Z. Yang, and J. Yan, "Transient heat transfer characteristics of supercritical fluid during rapid depressurization process," *Applied Thermal Engineering*, vol. 145, pp. 435–443, dec 2018.

[34] A. Fershtman, L. Shemer, and D. Barnea, "Transient convective heat transfer in a pipe due to impulsively initiated downward flow and/or heat flux," *International Journal of Heat and Mass Transfer*, vol. 111, pp. 1181–1191, aug 2017.

[35] M. Chen, X. Sun, R. N. Christensen, I. Skavdahl, V. Utgikar, and P. Sabharwall, "Dynamic behavior of a high-temperature printed circuit heat exchanger: Numerical modeling and experimental investigation," *Applied Thermal Engineering*, vol. 135, pp. 246–256, may 2018.

[36] M. Marchionni, L. Chai, G. Bianchi, and S. A. Tassou, "Numerical modelling and transient analysis of a printed circuit heat exchanger used as recuperator for supercritical CO2 heat to power conversion systems," *Applied Thermal Engineering*, vol. 161, p. 114190, oct 2019.

[37] B. Ruan, S. Huang, H. Meng, and X. Gao, "Transient responses of turbulent heat transfer of cryogenic methane at supercritical pressures," *International Journal of Heat and Mass Transfer*, vol. 109, pp. 326–335, jun 2017.

[38] H. Wang, J. Zhou, Y. Pan, and N. Wang, "Experimental investigation on the characteristics of thermo-acoustic instability in hydrocarbon fuel at supercritical pressures," *Acta Astronautica*, vol. 121, pp. 29–38, apr 2016.

[39] W. B. Bloem, R. J. van der Linden, C. J. Hoogendoorn, and H. Postma, "Experimental and numerical results on transient heat transfer to supercritical helium at low temperatures," *Wärme- und Stoffübertragung*, vol. 22, no. 6, pp. 315–323, nov 1988.

[40] F. Sharifi, M. G. Narandji, and K. Mehravaran, "Dynamic simulation of plate heat exchangers," *International Communications in Heat and Mass Transfer*, vol. 22, no. 2, pp. 213–225, mar 1995.

[41] *MICROPUMP - GC series.*

[42] P. Negendakumana, *Mesures de grandeurs thermofluides*, 2019.

[43] *Omega - All Stainless Steel Transducer/Transmitter Multimedia Compatibility.*

[44] F. P. Incropera, D. P. DeWitt, T. L. Bergman, and A. S. Lavine, *Fundamentals of Heat and Mass Transfer*. John Wiley & Sons, 2006.

[45] V. S. Amos Gilat, *Numerical Methods for Engineers and Scientists*. John Wiley & Sons Inc, 2013.

[46] B. K. Rao, "TURBULENT HEAT TRANSFER PERFORMANCE OF NEWTONIAN FLUIDS IN ASYM-METRICALLY HEATED RECTANGULAR CHANNELS," *Experimental Heat Transfer*, vol. 2, no. 3, pp. 227–236, jan 1989.

[47] S. K. Debrah, E. Shitsi, S. Chabi, and N. Sahebi, "Assessment of heat transfer correlations in the sub-channels of proposed rod bundle geometry for supercritical water reactor," *Heliyon*, vol. 5, no. 11, p. e02927, nov 2019.

[48] Crane, *Flow of Fluids Through Valves, Fittings, and Pipe*, New-York, 1977.

Appendix A

Modeling (code)

The different codes are provided as an attached file due to their length. It includes the IR image analysis, the steady-state model and the transient model of the heat exchanger. In addition to the IR image analysis, the different experimental data points recorded are present in the attached file.

Appendix B

Pressure drop analysis

The different pressure losses encountered by the flow are represented in Fig. B.1. It is interesting to note that the test section is symmetric and the pressure losses encountered in the inlet region are similar to the ones in the outlet. The difference being that a sudden reduction in diameter in the inlet becomes a sudden diameter expansion in the outlet. In the inlet, the first loss is a 90° bend combined with a diameter reduction. The flow then arrives in the header region and sees a sudden expansion with a sharp edge as the header flow path is orthogonal to the inlet, this is associated to a 90° bend. Between the header and the microchannels, the flow channel dimension is reduced. In addition to those minor losses, the friction losses in the tubes are also accounted for. At this point, the friction losses and the acceleration losses inside the channels start. As the test is adiabatic, the acceleration losses will be zero and the pressure drop verification will be done on the friction losses alone. After the channels, the flow sees a sudden expansion as it enters the header region. The flow pass ends up with a contraction coupled with a bend between the header and the outlet and finally a last bend with a sudden expansion.
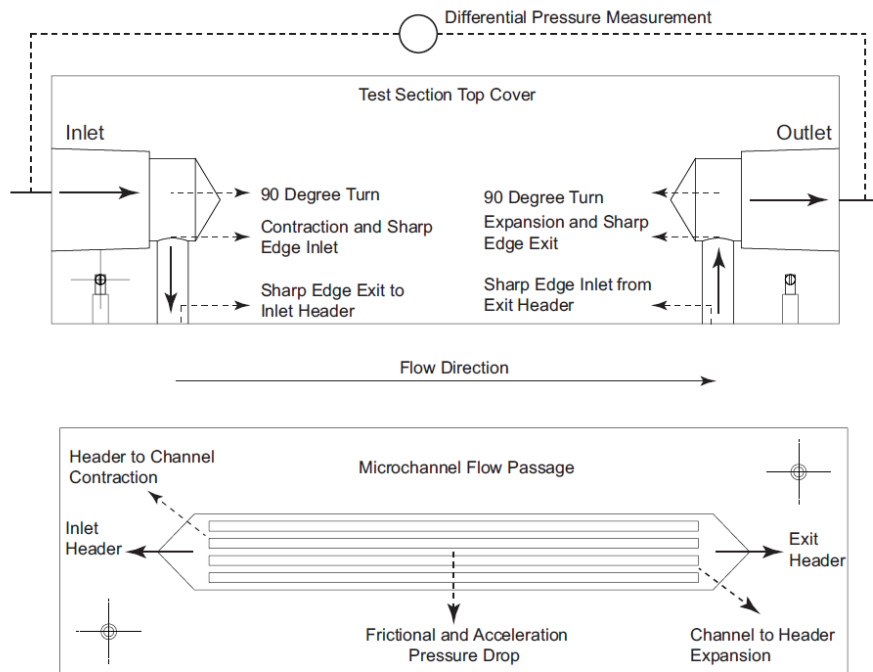

Figure B.1: Flow path of the carbon dioxide for the pressure drop analysis

The pressure drop model was done using the EES software that presents the advantage of having some pre-built functions for different minor losses. The different minor losses were computed by determining their respective K

value (resistance coefficients). The first minor loss encountered is the 90° bend, its K value is represented in Eq. B.1 and comes from [48]. The friction factor f_{turb} is the factor for a fully turbulent flow in a channel. The correlation used to compute it is in Eq. B.2 where ϵ_{rel} is the relative roughness and is equal to 0.00722 for the first bend in the stainless steel and is equal to 0.0009204 for the bend between the inlet and the header. D_{ave} is the average of the changing diameter across the bend as the flow sees a change in diameter during the bend.

$$K_{bend} = 60(f_{turb}) \tag{B.1}$$

$$\frac{1}{f_{turb}^{0.5}} = -2log\frac{\epsilon_{rel}}{3.7D_{ave}} \tag{B.2}$$

The other minor loss that happens is the sudden reduction/increase of the pipe diameter, to compute it a pre-built function of EES is used. This function uses an equation from [48] and will be used for the change in diameter in the pipe (entrance and exit). This equation is respectively for a reduction and increase of diameter:

$$K_{SC} = 0.5\left(1 - \frac{D_s^2}{D_l^2}\right) \tag{B.3}$$

$$K_{SE} = \left(1 - \frac{D_s^2}{D_l^2}\right)^2 \tag{B.4}$$

In order to account for the simplification used, an uncertainty of 50% is used over the minor losses. This explain why the uncertainty bars are longer than the uncertainty over the measure of the differential pressure of ±0.12kPa with the Rosemount 3051 SMV pressure transducer. With the different minor losses coefficients calculated, the associated pressure loss is computed using Eq. B.5 where the velocity is computed using the density of the fluid at the local state. For instance, the losses between the inlet and the header was computed using the temperature and the absolute pressure of the inlet.

$$\Delta_{P,minor} = \sum_{i=1}^{n} K_i \frac{V_i^2}{2}\rho_i \tag{B.5}$$

The pressure loss associated with the acceleration of the flow is evaluated by Eq. B.6. In the case of the adiabatic pressure test this loss is equal to zero as the temperature at the inlet and outlet are equals.

$$\Delta_{P,acc} = (\rho_{out}V_{out}^2 - \rho_{in}V_{in}^2) \tag{B.6}$$

With the different minor losses and the acceleration loss computed, those losses are substracted to the measured pressure drop to get the frictional pressure drop along the channels. To determine the theoretical pressure loss in the microchannel, the Darcy friction factor for turbulent flow (shown in Eq. B.7 to B.9) is used. The Reynolds number is computed using the bulk flow temperature at the inlet and the absolute pressure to determine the viscosity. As the flow is turbulent for all the experiments, no friction factor for a laminar flow was used. From that factor, the pressure loss is computed by Eq. B.10 where the density and velocity are evaluated at both the bulk flow temperature and the film temperature to see the effects over the pressure drop.

$$f_{turb} = 8\left[\frac{8}{Re_{D_h}}^{12} + (\theta_1 + \theta_2)^{-1.5}\right]^{\frac{1}{12}} \tag{B.7}$$

$$\theta_1 = \left[2.457ln\left[\left[\frac{7}{Re_{D_h}}\right] + 0.27\frac{R_a}{D_h}\right]^{-1}\right]^{16} \tag{B.8}$$

$$\theta_2 = \left[\frac{37530}{Re_{D_h}}\right]^{16} \tag{B.9}$$

$$\Delta_{P,theo} = f_{turb} \frac{L_{chan}}{D_h} \frac{V_{chan}^2}{2} \rho_{chan} \tag{B.10}$$

Appendix C

MAPE results of the correlations in steady-state

T_{inlet} (°C)	T_{outlet} (°C)	G (kg/m^{2}s)	q" (W/cm^2)	Miropolski	Ornatsky	Jackson
31,06	32,62	485,99	6,88	28,86	49,13	22,47
31,20	32,79	479,73	8,74	17,06	41,55	14,55
31,67	32,98	482,07	10,55	22,95	28,18	17,54
31,73	33,12	488,65	12,80	26,38	23,4	12,96
32,78	33,17	493,25	6,90	13,08	19,42	6,67
32,80	33,46	483,67	8,74	21,04	11,77	6,53
32,80	33,78	480,51	10,55	22,87	11,18	4,53
32,94	34,52	494,81	12,80	21,01	13,08	5,74
32,79	33,99	500,63	13,41	20,62	15,16	4,75
32,59	33,56	507,15	12,80	24,36	13,22	4,98
32,66	33,68	491,36	12,55	27,99	11,6	5,16
32,42	33,46	500,24	13,41	32,76	14,54	8,01
32,45	33,64	550,72	15,70	30,49	12,1	5,04
32,48	33,58	630,36	17,13	33,99	11,87	6,66
32,77	33,03	740,68	8,74	14,85	19,16	11,18
32,87	33,29	726,86	10,55	22,91	10,74	11,45
32,85	33,53	733,76	12,80	27,4	9,33	9,23
32,89	33,72	744,08	13,41	26,94	7,38	7,3
32,82	33,67	823,55	17,13	35,48	10,3	10,51
32,64	33,05	456,71	6,88	15,89	19,18	9,38
32,71	33,35	444,28	8,74	19,29	15,78	6,61
32,86	33,95	444,83	10,55	17,97	15,8	4,75
32,77	34,15	463,48	12,80	27,58	10,96	3,78

Table C.1: MAPE results (in %) for all the tests performed in steady-state

T_{inlet} (°C)	$T_{inlet,chan}$ (°C)	T_{outlet} (°C)	G (kg/m²s)	q" (W/cm²)	Model prediction
31,06	31,44	32,62	485,99	6,88	24,5
31,20	31,66	32,79	479,73	8,74	13,65
31,67	32,1	32,98	482,07	10,55	21,42
31,73	32,21	33,12	488,65	12,80	17,64
32,78	32,85	33,17	493,25	6,90	5,98
32,80	32,88	33,46	483,67	8,74	10,25
32,80	32,89	33,78	480,51	10,55	10,98
32,94	33,05	34,52	494,81	12,80	8,43
32,79	32,98	33,99	500,63	13,41	8,58
32,59	32,77	33,56	507,15	12,80	11,4
32,66	32,84	33,68	491,36	12,55	12,69
32,42	32,67	33,46	500,24	13,41	17,1
32,45	32,72	33,64	550,72	15,70	13,45
32,48	32,72	33,58	630,36	17,13	18,06
32,77	32,83	33,03	740,68	8,74	14,66
32,87	32,93	33,29	726,86	10,55	17,08
32,85	32,92	33,53	733,76	12,80	16,4
32,89	32,96	33,72	744,08	13,41	15,26
32,82	32,92	33,67	823,55	17,13	24
32,64	32,73	33,05	456,71	6,88	10,96
32,71	32,83	33,35	444,28	8,74	10,31
32,86	32,99	33,95	444,83	10,55	5,69
32,77	32,94	34,15	463,48	12,80	9,21

Table C.2: MAPE results (in %) of the model prediction compared to all the tests performed in steady-state